Textures, Vortices and Persistent Currents in a Slab of ^{3}He-A

A thesis submitted to the University of Manchester for the Degree of Doctor of Philosophy in the Faculty of Science and Engineering

Paul Michael Walmsley
Department of Physics and Astronomy
2003

Contents

Abstract **6**

Declaration **7**

Copyright Notice **8**

Acknowledgements **9**

1 Introduction **10**

1.1 Superfluidity 10

1.2 Superfluid ^{3}He 11

1.3 ^{3}He-A 12

1.4 Textures in ^{3}He-A 14

1.4.1 Orientational Effects 14

1.4.2 The Fréedericksz Transition 16

1.5 Orbital Ferromagnetism 18

1.6 Rotating ^{3}He-A 19

1.6.1 Vortices 19
1.6.2 Persistent Currents 23

2 Textures in a Slab 25

2.1 Introduction 25
2.2 Calculating textures 27
2.3 One-dimensional textures 29
2.4 Effect of Orbital Ferromagnetism 31
2.4.1 Low Fields 34
2.4.2 High Fields 35
2.5 Two-dimensional textures 36
2.5.1 Domain walls 38
2.5.2 Radial AT Vortices 40

3 The Torsional Oscillator 48

3.1 Introduction 48
3.2 Equations of motion 49
3.3 Construction 50
3.4 Magnetic shielding and DC coil 52
3.5 Electronics 52
3.6 Control Method 55
3.7 Thermometry 57

3.7.1 Normal ^{3}He 60

3.7.2 Superfluid ^{3}He-A 61

3.8 Textures in a slab of ^{3}He-A in a torsional oscillator 61

4 The Rotating Cryostat 65

4.1 Introduction 65

4.2 Overview of the cryostat 66

4.3 The heat leak problem 68

4.4 Vibration measurements 69

4.4.1 Vibration detectors 69

4.4.2 Search coils 70

4.5 Solutions to the vibration problem 71

5 Effect of rotation on texture formation 82

5.1 Introduction 82

5.2 Field sweeps 83

5.3 Effect of rotation 88

5.4 Measurement of H_F 91

6 Rotation while superfluid: uniform textures 97

6.1 Introduction 97

6.2 Acceleration and deceleration of a superfluid 98

6.3 Rotation sweeps 101

6.4 Vortex critical velocity 106

6.5 Rotation sweeps in both directions 112

7 Rotation while superfluid: non-uniform textures 118

7.1 Introduction 118

7.2 Rotation sweeps 119

7.3 Lifetime and decay of persistent currents 123

7.4 Dependence of Ω_{pers} on Ω_{max} 123

7.5 Field sweeps 127

7.6 Possible models 132

8 Conclusions 136

References 139

Abstract

We have investigated textures, vortices and persistent currents in a 0.26 mm thick slab of superfluid ^{3}He-A using a rotating nuclear demagnetization cryostat. The detection technique, monitoring the resonance of a torsional oscillator containing the slab, is sensitive to both magnetic field and counterflow induced reorientation of the **l** texture. Rotation during cooling into the superfluid transition has been used to obtain uniform **l** textures. We have observed two critical velocities when an initially uniform texture is rotated: the flow induced Fréedericksz transition velocity and the velocity for nucleation of the first vortex. We find that uniform textures are able to pin weakly approximately 10 quanta circulation and non-uniform textures are able to pin strongly about 60 quanta of circulation, leading to long lived persistent currents after rotation has been stopped. We have investigated the magnitude and direction of the persistent currents as a function of the preparation angular velocity. The maximum possible persistent current that can be generated is approximately the same for non-uniform textures that have been prepared in different ways. The mechanism responsible for the persistent currents is not yet fully understood, but comparisons with a strong pinning model have been made. The effect of orbital ferromagnetism on textures has been calculated. Attempts to detect these effects experimentally have so far proved unsuccessful. Numerical calculations of some of the possible textures in a slab geometry, such as domain walls and vortices, are presented.

Declaration

No portion of the work referred to in this thesis has been submitted in support of an application for another degree or qualification of this or any other university or other institute of learning.

Copyright Notice

1. Copyright of the text of this thesis rests with the Author. Copies (by any process) either in full, or of extracts, may be made **only** in accordance with instructions given by the Author and lodged in the John Rylands University Library of Manchester. Details may be obtained from the Librarian. This page must form part of any such copies made. Further copies (by any process) of copies made in accordance with such instructions may not be made without the permission (in writing) of the Author.
2. The ownership of any intellectual property rights which may be described in this thesis is vested in the University of Manchester, subject to any prior agreement to the contrary, and may not be made available for use by third parties without the written permission of the University, which will prescribe the terms and conditions of any such agreement.

Further information on the conditions under which disclosures and exploitation may take place is available from the Head of the Department of Physics and Astronomy.

Acknowledgements

I am particularly grateful to John Hook and Andrei Golov for their supervision and guidance. John got this work started and his death part way through has been a huge loss to the group. He was an outstanding low temperature physicist. Andrei has done an excellent job of leading the work forward with many innovative ideas and explanations. I am also indebted to Henry Hall for many useful discussions and ideas. I am thankful to Josie Naish and Derek Cousins for their work in sorting out the cryostat and helping to get the experiment up and running. The technical input of Steve May has been crucial to the success of the experiment. He has also been a constant source of advice on a wide variety of matters. Thanks to Stan and Mark for providing helium. I'm also grateful to Paul, Ladan, Simone, Ian and Chris for livening up the office and making it an enjoyable place to work.

Finally, a huge thanks to my wife for her love and encouragement and also to my parents for all their support during my time at univeristy.

Chapter 1

Introduction

1.1 Superfluidity

At very low temperatures particles tend to occupy the lowest available energy states. For a quantum gas or liquid of bosons this leads to many particles condensing into a single energy state (known as Bose Einstein condensation (BEC)), resulting in quantum behaviour being observed on a macroscopic scale due to the long range quantum coherence of the system.

^{4}He shows such behaviour when cooled below 2.17 K. Below this second order transition the fluid can be considered as to consist of two interpenetrating fluids: a normal component (with density ρ_n and velocity $\mathbf{v_n}$) which carries all the entropy and a superfluid component (with density ρ_s and velocity $\mathbf{v_s}$) with zero viscosity. The total density of the fluid is then $\rho_n + \rho_s$, with the superfluid fraction increasing with decreasing temperature and a total current density of $\mathbf{j} = \rho_n \mathbf{v_n} + \rho_s \mathbf{v_s}$. This description is known as the two fluid model and has been very successful in explaining the hydrodynamic properties of superfluids. The macroscopic wavefunction, known as the order parameter, for superfluid ^{4}He is a complex scalar,

$$\psi(\mathbf{r}) = \psi_0 \exp\left(iS(\mathbf{r})\right) \tag{1.1}$$

where ψ_0 is a temperature dependent scalar amplitude and $S(\mathbf{r})$ is a position dependent phase. Further information on superfluidity in ^{4}He can be found in the books by Guénault [1] and Tilley and Tilley [2].

BEC in dilute gases of alkali atoms was discovered in 1995. Wieman and Cornell found the transition in Rubidium atoms at temperatures of a few hundred nanokelvin [3] and Ketterle later with sodium atoms [4], achievements that merited the Nobel physics prize in 2001. BEC of several other elements have since been discovered.

In contrast, fermions are prevented by quantum statistics from condensing into a single quantum state. However, Cooper showed that it is energetically more favourable for two particles with an attractive interaction, contained above a filled Fermi sea of particles, to form a bound state [5], known as a Cooper pair. He showed that this occurs no matter how weak the interaction. Bardeen, Cooper and Schrieffer (BCS) extended this idea to a system where many particles could form Cooper pairs [6]. This theory was successful in explaining the phenomena of superconductivity in metals by showing that the conduction electrons could form s-wave, spin singlet Cooper pairs.

BCS theory was then applied to ^{3}He (a fermion) which along with the more common isotope remains liquid in the absence of applied pressure down to the lowest temperatures yet achieved due to a high zero point energy.

1.2 Superfluid ^{3}He

^{3}He atoms cannot form Cooper pairs in the same way as electrons in a superconductor because He atoms have a strong mutual repulsion when they are close together. This prevents s-wave pairing because such pairing implies the particles are more likely to be found close together. At larger separations there is a weak Van der Waals attraction, so theories with Cooper pairs that had finite angular momentum were developed.

Anderson and Morel [7] proposed a model consisting of p-wave, spin triplet Cooper pairs where the ^{3}He quasiparticles had parallel spins, $|\uparrow\uparrow\rangle$ and $|\downarrow\downarrow\rangle$. Balian and Werthamer [8] provided a more complete treatment which included an antiparallel spin combination, $|\uparrow\downarrow\rangle +$ $|\downarrow\uparrow\rangle$, the third substate of the spin symmetric triplet. They showed that this BW state should have a lower energy than that Anderson and Morel (ABM) state, making it the stable state. However, spin fluctuations result in the ABM phase being the stable state at high pressures and temperatures close to the superfluid transition T_c [9]. The superfluid phases of ^{3}He were discovered in 1972 by Osheroff, Richardson and Lee [10, 11] by using the Pomeranchuk method to obtain temperatures below 3 millikelvin, an achievement that was awarded the 1996 Nobel physics prize. The phase diagram of ^{3}He is shown in figure 1.1. The A and B phases are the ABM and BW phases respectively. At finite magnetic fields a third superfluid phase, A1, appears between the A-phase and the normal state. This phase consists only of $|\uparrow\uparrow\rangle$ spin states. The A phase is stabilized down to zero temperature for magnetic fields greater than 0.34 T at zero pressure and 0.56 T at 29.3 bar.

There has been a huge amount of both experimental and theoretical work on the superfluid phases of ^{3}He in the thirty years since their discovery, showing that they are among the most fascinating and unique condensed matter systems. Further details of much of this work can be found in [13]. This work is only concerned with experiments on ^{3}He-A so the other phases will not be discussed further.

1.3 ^{3}He-A

The order parameter vector of the A phase can be written as

$$\mathbf{D}(\mathbf{k}) = \Delta_0\,(\mathbf{m} + i\mathbf{n}) \cdot \mathbf{k}\,\mathbf{d} \tag{1.2}$$

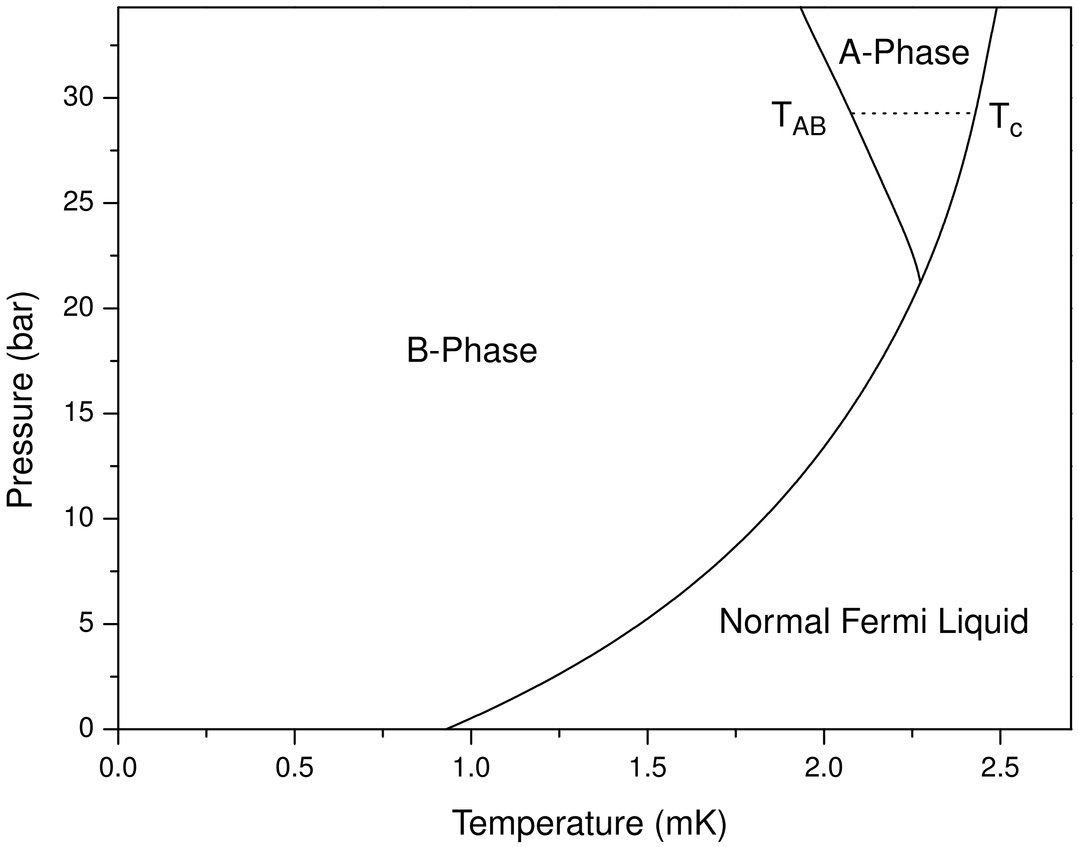

Figure 1.1: Phase diagram of ^{3}He at low temperatures and zero magnetic field [12]. The dotted line indicates the values of pressure and temperature that were used in the experiment described in this thesis.

where $\mathbf{d}$ is a unit vector in spin space, pointing along a direction where the component of spin is zero (i.e. $\mathbf{s}\cdot\mathbf{d} = 0$). $\mathbf{m}$ and $\mathbf{n}$ are a pair of orthogonal unit vectors defined such that

$$\mathbf{l} = \mathbf{m} \times \mathbf{n} \tag{1.3}$$

where $\mathbf{l}$ a unit vector in the direction of the orbital angular momentum of the Cooper pairs. The scalar product in equation 1.2 shows that the energy gap varies as a function of wavevector $\mathbf{k}$ and has axial symmetry about $\mathbf{l}$ with nodes along $\mathbf{l}$ and a maximum values of Δ_0 perpendicular to $\mathbf{l}$. The existence of these nodes means that excitations with $\mathbf{k}$ parallel or antiparallel to $\mathbf{l}$ can take place at arbitrarily low temperatures resulting in the properties of the A phase, such as viscosity and superfluid density, being strongly anisotropic. In contrast, the B phase has an isotropic energy gap resulting in its properties being similar to those of conventional superconductors, although it still displays weak anisotropy due to the dipole-dipole interaction between the quasiparticles that make up the Cooper pair.

1.4 Textures in ^{3}He-A

1.4.1 Orientational Effects

The spatial variations of $\mathbf{l}$ and $\mathbf{d}$ are known as textures, analogous to textures formed by the director in nematic liquid crystals [16]. The condensation energy is not changed by rotation of these vectors so the textures are determined by the geometry of the sample container and other orientational effects. A detailed discussion of textures and orientational effects is given in the theoretical review articles by Leggett [15] and Brinkman and Cross [14]. The main orientational effects in ^{3}He-A relevant to the experiments discussed in this thesis are described briefly below, but are covered in more detail in the following chapter along with calculations of some relevant textures.

Gradients in the texture cause an increase in energy due to bending of the order parameter, so the system has an internal stiffness that results in spatially uniform textures being preferred and hence preventing other orientational effects from changing the direction of the texture on small length scales. The walls of the container play an important role in determining textures since $\mathbf{l}$ must be perpendicular to the boundaries [17] because otherwise the Cooper pairs would be broken. Also the requirement that there should be no spin current through the walls means that the component of $\nabla\mathbf{d}$ perpendicular to the boundaries must be zero. The $\mathbf{l}$ and $\mathbf{d}$ vectors are not completely independent of each other but are coupled due to the weak dipole-dipole interaction between the ^{3}He atoms. The energy contribution from this interaction is minimized when $\mathbf{d}$ and $\mathbf{l}$ are either parallel or antiparallel. Textures where $\mathbf{d} \equiv \pm\mathbf{l}$ are called dipole -locked. The anisotropy of the spin system means that the magnetic properties, such as the susceptibility, are anisotropic about $\mathbf{d}$. This gives a magnetic energy contribution that favours $\mathbf{d}$ being aligned perpendicular to any applied magnetic field. The texture is also influenced by relative motion of the normal and superfluid components (known as counterflow), $\mathbf{v_s} - \mathbf{v_n}$. The flow energy is minimized when $\mathbf{l}$ is aligned along the direction of flow for small counterflow velocities but at higher velocities dissipation can be caused by the formation of non-uniform textures. The most widely studied example is that of a helical $\mathbf{l}$ texture that precesses about the flow direction.

The equilibrium texture is found by minimizing the free energy density, incorporating all the above orientational effects and the relevant boundary conditions. In some cases the texture is only a local minimum of the free energy resulting in a metastable state that is prevented by an energy barrier from reaching the global minimum of free energy. Further details and examples of textures are given in chapter 2.

1.4.2 The Fréedericksz Transition

The texture is often determined by several competing orientational effects. In the case of a slab of ^{3}He-A with an applied field perpendicular to the slab the uniform texture is the stable solution for fields less than a threshold field, $H < H_F$. Above this field the texture starts to distort in the center of the slab since it is energetically preferable for $\mathbf{d}$ (and also $\mathbf{l}$ due to the dipole-dipole interaction) to be perpendicular to $\mathbf{H}$. At high fields, $H >> H_F$, the texture is almost fully bent over, apart from a layer near the boundary where $\mathbf{l}$ remains anchored perpendicular to the boundary. This textural transition, illustrated in figure 1.2, is known as a Fréedericksz transition, named after the discoverer of the similar transition in nematic liquid crystals [16]. The transition in ^{3}He-A was studied extensively by the Manchester group in two different experiments [18]. The first used a torsional oscillator to measure changes in the $\mathbf{l}$ texture through the anisotropy of the superfluid density and viscosity in a 0.1 mm thick cylindrical slab [19]. They found that the resonant frequency (the inertial component) of the oscillator decreased sharply at H_F, whereas the bandwidth (the dissipative component) showed an initial dip before increasing at higher fields (see figure 1.3). The second experiment used the anisotropy of the attenuation of ultrasound to measure changes in $\mathbf{l}$ in a 2 mm thick slab [20]. The combined results for H_F as a function of temperature are shown in figure 1.4. The transition field is inversely proportional to the slab thickness.

The Fréedericksz transition has proved to be a powerful tool in the experiments described in this thesis. In chapter 5 it is shown how the transition can help quantify the uniformity of textures. A Fréedericksz transition can also be caused by counterflow, where the uniform texture is distorted when flow above a critical value is applied in a direction parallel to the boundaries of the slab. Such transitions have been measured in this experiment and are described in detail in chapter 6.

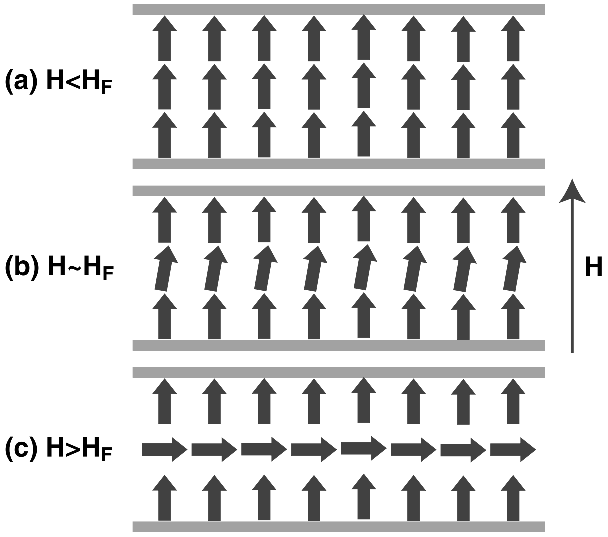

Figure 1.2: Fréedericksz Transition in a ^{3}He-A slab. a) Uniform texture. b) Texture starts to distort in center. c) Texture is almost parallel to boundaries everywhere except near the boundaries.

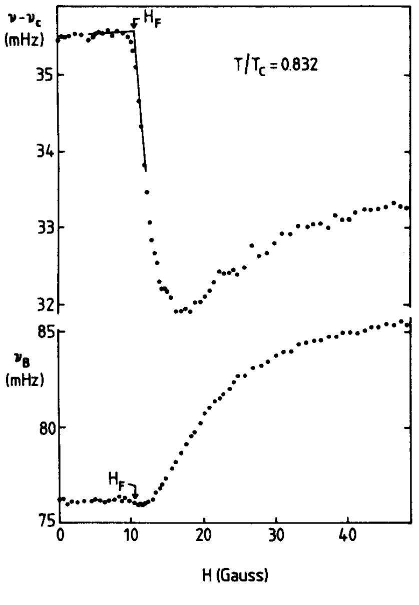

Figure 1.3: Fréedericksz transition measured using a torsional oscillator. The upper and lower parts show the shifts in resonant frequency and bandwidth respectively. Taken from [18].

1.5 Orbital Ferromagnetism

An isolated ^{3}He atom does not possess a permanent electric dipole moment because the filled 1s orbital is spherical. However, if two ^{3}He atoms come into close proximity then the electron shells are distorted and each atom will become slightly polarized. Since the ^{3}He atoms in a Cooper pair have finite angular momentum there exists a small magnetic moment oppositely direct to **l** due to the circulating charge distributions. This occurs in most diatomic molecules, but since the molecules are randomly orientated the effect averages to zero. In contrast, a sample of ^{3}He-A with a uniform **l** texture is expected to have a net magnetization due to the magnetic moments all pointing in the same direction. Hence the system can be described as ferromagnetic as this magnetization appears only at temperatures below the superfluid transition T_c. This effect provides an example of how a microscopic interaction can be observed on a macroscopic scale due to the quantum coherence of the system

In 1977 Tony Leggett [21] estimated the orbital magnetic moment to be about $10^{-11}\mu_B$ per atom by using details of the interaction between two He atoms calculated by Kestner [22]. The temperature dependent magnetization, M_l can be written as an equivalent field

$$\mathbf{H_m} = \frac{\mathbf{M_l}}{\chi_N} \tag{1.4}$$

where χ_N is the normal state susceptibility. $\mathbf{H}_m$ can then be written as

$$\mathbf{H_m} = -H_0\left(1 - \frac{T}{T_c}\right)\mathbf{l} \tag{1.5}$$

where H_0 is estimated to be 10-20 mG.

Leggett states that his estimate is at best ‘a crude order of magnitude’ and there are several questionable aspects of his calculation. The distorted electronic wave functions Leggett uses were calculated using self consistent field molecular orbitals (SCF-MO), a method that has been superseded by more advanced techniques such as quantum Monte Carlo calculations [23] and density functional theory [24] (a list of some results for the He-He interaction is given in [25]). Also the interaction in ^{3}He-A is not between bare ^{3}He atoms but between quasiparticles which have masses several times greater than the bare mass ($m^* = 5.45m$ at 29 bar pressure [12]). Hence, more theoretical calculations on the size of the magnetic moment would be useful to get a better estimate of the size of the effect.

Shortly after Leggett performed his calculation Paulson and Wheatley measured small changes of **l** textures by observing the attenuation of ultrasound [26]. To some extent their results showed that the orientation of **l** depended on the sign of the applied magnetic field. They claimed agreement with Leggett's calculation but they had non-uniform **l** textures due to the cell geometry making any quantitative estimate of the effect difficult.

The original motivation behind this work was to try to measure the orbital ferromagnetism. The effect of the ferromagnetism on the Fréedericksz transition is calculated in section 2 and the results of experimental attempts to detect this effect are described in chapter 5.

1.6 Rotating ^{3}He-A

1.6.1 Vortices

The order parameter for superfluid ^{4}He (equation 1.1) is simpler than the one for ^{3}He-A (equation 1.2) so we firstly consider the effect of rotation upon superfluid ^{4}He before considering the effect upon ^{3}He-A . The velocity of the superfluid component in ^{4}He is proportional to the gradient of the phase,

$$\mathbf{v_s} = \frac{\hbar}{m_4}\nabla S \tag{1.6}$$

where m_4 is the mass of a ^{4}He atom and it follows from this that the superfluid component executes irrotational motion and there is no vorticity,

$$\nabla \times \mathbf{v_s} = 0. \tag{1.7}$$

The circulation is defined by

$$\kappa = \oint \mathbf{v_s} \cdot d\mathbf{l} \tag{1.8}$$

and using equation 1.6 gives

$$\kappa = \frac{\hbar}{m_4} \Delta S. \tag{1.9}$$

The requirement that the order parameter is single valued means that the change in S (ΔS) after moving around a closed contour can only be either zero or an integer multiple of 2π. Hence the circulation is quantized,

$$\kappa = N \frac{h}{m_4} \tag{1.10}$$

where h/m_4 is known as the quantum of circulation and N is an integer. Fenyman [28] suggested that an array of quantized vortex lines, each with a core consisting of normal fluid, should form when the superfluid is rotated. The superfluid is then able to mimic solid body rotation without violating equation 1.7 since the vorticity is concentrated in the vortex filaments. There has since been a great deal of both theoretical and experimental work on vortices in ^{4}He, much of which is reviewed in the book by Donnelly [29].

The superfluid velocity in the case of ^{3}He-A is

$$v_{s,i} = \frac{\hbar}{2m_3} \mathbf{m} \cdot \nabla_i \mathbf{n} \tag{1.11}$$

where m_3 is the mass of a ^{3}He atom. This means that in general the superflow of ^{3}He-A is not irrotational. Instead, Mermin and Ho [30] showed that the vorticity depends on gradients in the **l** texture:

$$\nabla \times \mathbf{v_s} = \frac{\hbar}{2m_3} \sum_{ijk} e_{ijk}\, l_i \nabla l_j \times \nabla l_k \tag{1.12}$$

and hence ^{3}He-A is only irrotational if the right hand side of equation 1.12 is zero, which occurs at the container walls where **l** is rigidly held perpendicular to the boundaries. Away from the walls the texture can respond to superflow by forming an inhomogeneous texture leading to continuously distributed vorticity and a lattice of textural vortices. Although in general the circulation round an arbitrary path in the bulk fluid is not quantized, the unit cell of a lattice of textural vortices must contain an integer number of circulation quanta. Hence a rich variety of vortex structures can be created in ^{3}He-A with circulation

$$\kappa = N\frac{h}{2m_3} \tag{1.13}$$

where $\kappa_0 = h/2m_3 = 0.066$ mm^2/s is the quantum of circulation for ^{3}He . The structure and quantum number N of the vortices depend on the angular velocity Ω, applied magnetic field and often on the rotation history of the sample. The vortices can be singular, which have a hard core radius comparable to the superfluid coherence length ξ. In this case the superfluid velocity is undefined in the vortex core and the order parameter vanishes at the center. An example of such a vortex is shown in figure 1.5. The vortex lines can also be continuous with a soft core radius much greater than ξ. The amplitude of the order parameter is almost constant in such vortices and the superfluid velocity is well defined everywhere (see figure 1.6) with the vorticity $(\nabla \times v_s)$ distributed throughout the texture.

Most of the experimental work on vortices in ^{3}He-A has been performed by the Helsinki group during the last twenty years (see [31, 32] for a review). The sample geometry typically used was a cylindrical container of length 7 mm and diameter 5 mm. This was rotated about its axis with $\Omega \leq 3$ rad/s. The vortices were detected by observing cw-NMR absorption spectra, with different types of vortex structure producing absorption peaks shifted with respect to the bulk peak. ^{3}He-A also supports vortex sheets [33, 34] as well as vortex lines. This is a textural domain wall between regions of $\mathbf{l}$ in opposite direction that becomes decorated with vorticity when rotation is started.

The Manchester group [27] showed that rotation during cooling through the superfluid transition can play an important role in obtaining a uniform $\mathbf{l}$ texture in a slab geometry after the rotation has been stopped. It was also shown that rotation in the opposite direction can eventually reverse the direction of the texture after several bursts of rotation whilst in the superfluid state. The effect of varying the rotation speed during cooling with and without an applied magnetic field is

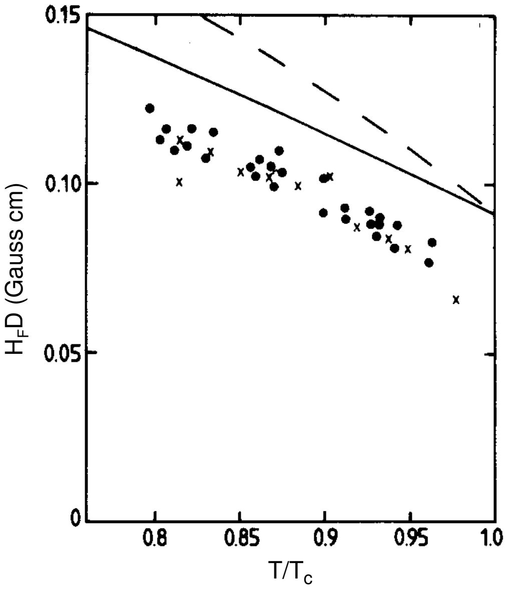

Figure 1.4: $H_F\,D$ as a function of temperature for the torsional oscillator experiment (circles) and ultrasonic experiment (crosses) [18]. The solid and dashed lines are theoretical curves using the BCS weak coupling and strong coupling energy gaps respectively.

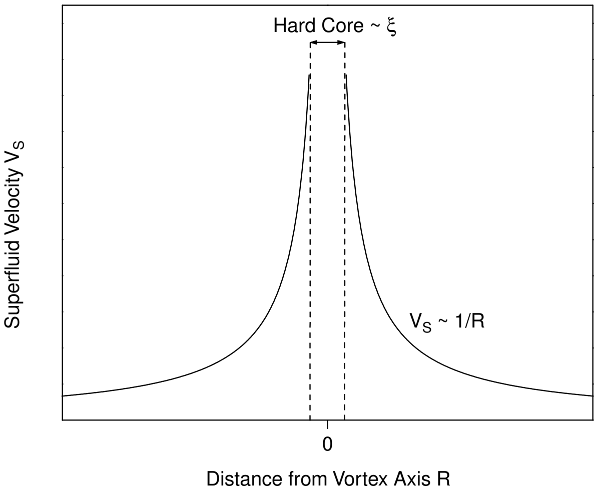
Hard Core ~ ξ
Superfluid Velocity V_S
V_S ~ 1/R
0
Distance from Vortex Axis R

Figure 1.5: Velocity profile of a singular vortex. The core of the vortex consists only of normal fluid. Examples of such vortices are those found in superfluid ^{4}He and conventional superconductors.

described in chapter 5.

1.6.2 Persistent Currents

Some of the classic experiments on superfluids have involved the demonstration of long lived persistent currents. For superfluids this involves rotating the container (and often the whole cryostat) above a critical velocity for the superfluid, then stopping rotation. The motion of the superfluid will then continue to persist indefinitely. In the case of superconductors, electrical currents have been shown to persist over a period of many years [2].

Experiments looking for persistent currents in superfluid ^{3}He-A have been performed by the Cornell [36] and Helsinki groups [37] (see [38] for a review). The Cornell experiment used a toroidal shaped container packed with 25 μm powder mounted on a torsional oscillator. They detected persistent currents by measuring the dissipation of small amplitude torsional oscillations. The dissipation was a minimum when the angular velocity of the cryostat matched that of the superfluid component. The Helsinki group first used an AC gyroscope, but no persistent currents in the A-phase were found [39]. A later experiment at Helsinki used a stack of thin Mylar plates with an average separation of 19 μm. NMR was used to observe a surface spin-wave mode which acted as a probe of the interaction between the $\mathbf{l}$ texture and superflow. They find that rotating the cryostat above a critical velocity of 0.5-0.6 rad/s and then stopping again leads to hysteresis in the observed NMR signal resulting from the presence of a persistent current. Both of the above experiments use a restricted geometry in order to pin vortices, increase the critical velocity for vortex nucleation and prevent dissipation of the superflow by large scale motion of the $\mathbf{l}$ texture, an effect resulting from the orbital anisotropy of ^{3}He-A . In chapter 7 persistent currents in a slab of ^{3}He-A are described. In our case, the disorder in the texture itself rather than an external influence can stabilize the currents.

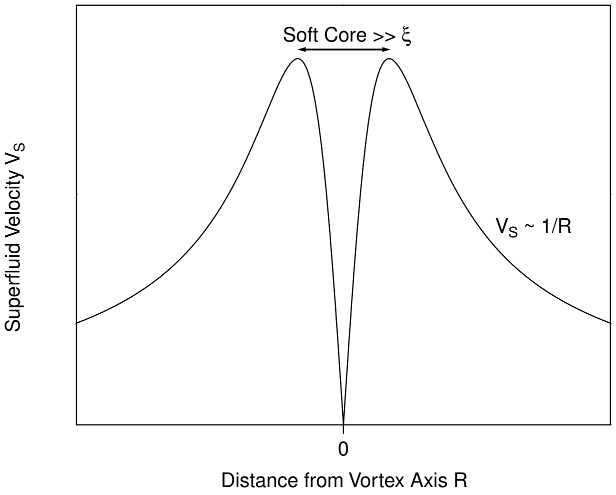

Figure 1.6: An example of the velocity profile of a continuous vortex. In this case an Anderson-Toulouse vortex [35] in ^{3}He-A which has two quanta of circulation ($N = 2$).

Chapter 2

Textures in a Slab

2.1 Introduction

All the experiments described in this thesis used a cylindrical slab geometry for the ^{3}He-A container. The main reason for using a slab (where the radius, R, is much greater than the slab thickness, D) is that the global minimum of free-energy (the ground state) is a spatially uniform texture, apart from a small region close to the side walls which can be neglected. This is important for an experiment designed to measure the orbital ferromagnetism of ^{3}He-A since the magnetic moment of each Cooper pair points in the same direction in a uniform texture, making any quantitative measurement of this quantity much easier to interpret. The non-uniform textures for various other sample geometries are shown in figure 2.1.

In practice the textures obtained in a slab of ^{3}He-A are not necessarily uniform since there are several metastable states which are prevented from reaching the ground state by large energy barriers (e.g. due to bending energies) and topological constraints. Therefore a variety of stable defects can be supported by ^{3}He-A . Planar defects such as domain walls separating regions with $\mathbf{l}$ in opposite directions are possible and rotating the superfluid enables quantized vortices to be obtained,

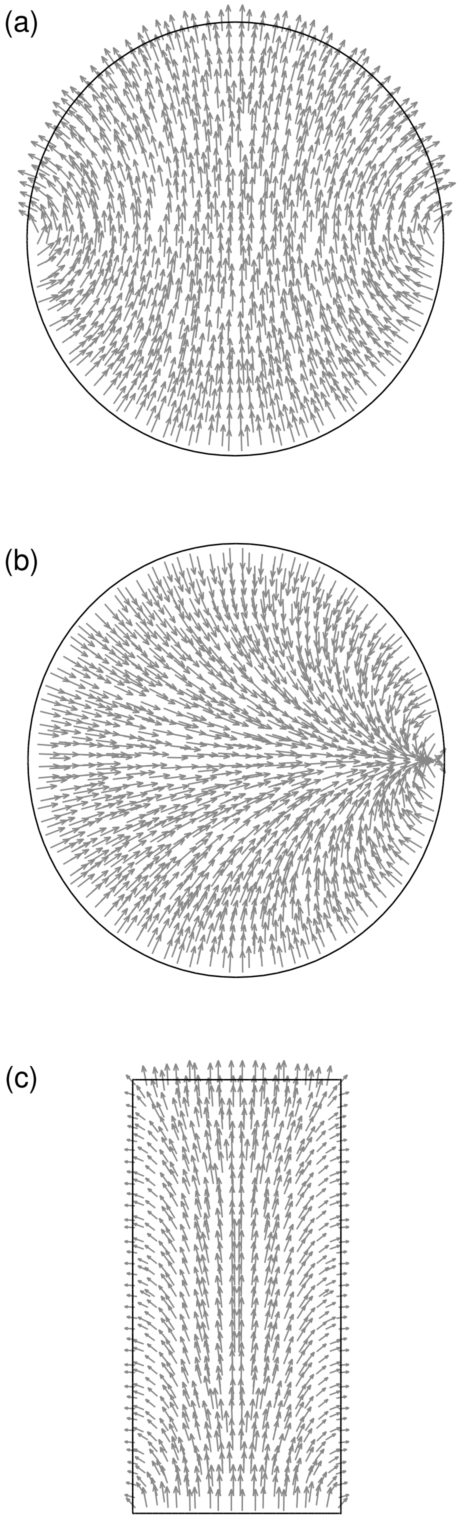

Figure 2.1: Numerical simulation of textures in various containers and zero applied field. (a) Pan-Am texture in a cylinder, (b) Boojum textures in a sphere and (c) Mermin-Ho texture in a cylinder.

which in the case of continuous vortices in zero magnetic field, have a soft core size of the same order as the slab thickness . The ends of the vortex line at the slab boundaries are terminated by point singularities (known as boojums). Therefore, the vortex cores in a slab can be either isolated or overlapped depending on the angular velocity and the direction and magnitude of applied magnetic field.

In section 2.2 an outline of how textures were calculated in this work is given. Section 2.3 then gives examples of one-dimensional textures. The effect of orbital ferromagnetism on these textures is calculated in section 2.4, then examples of textures in two-dimensions are covered in section 2.5 including domain walls and vortices.

2.2 Calculating textures

All of the texture calculations described in this chapter utilize the hydrodynamic (or London) limit where the length scale of any textural variations in the superfluid is greater than the coherence length ξ. This means that the A-phase order parameter (eqn. 1.2) holds for the whole superfluid and the energy depends on the spatial variation of **l** and **d**.

The free energy density in a frame where the normal fluid is at rest ($v_n = 0$) is then

$$\begin{aligned} f_{gr} \;=\; & \frac{1}{2}\rho_{s\perp}\tilde{\mathbf{v}}_{\mathbf{s}}^2 + \frac{1}{2}\left(\rho_{s\parallel} - \rho_{s\perp}\right)\left(\mathbf{l}\cdot\tilde{\mathbf{v}}_{\mathbf{s}}\right)^2 + C\left(\tilde{\mathbf{v}}_{\mathbf{s}}\cdot\nabla\times\mathbf{l}\right) - C_0\left(\mathbf{l}\cdot\tilde{\mathbf{v}}_{\mathbf{s}}\right)\left(\mathbf{l}\times\operatorname{curl}\mathbf{l}\right) \\ & + \frac{1}{2}K_s\left(\nabla\cdot\mathbf{l}\right)^2 + \frac{1}{2}K_t\left(\mathbf{l}\cdot\nabla\times\mathbf{l}\right)^2 + \frac{1}{2}K_b\left|\mathbf{l}\times\left(\nabla\times\mathbf{l}\right)\right|^2 \qquad (2.1) \\ & + \frac{1}{2}K_4\nabla\cdot\left[\left(\mathbf{l}\cdot\nabla\right)\mathbf{l} - \mathbf{l}\left(\nabla\cdot\mathbf{l}\right)\right] + \frac{1}{2}\rho_{sp\parallel}\left|\left(\mathbf{l}\cdot\nabla\right)\mathbf{d}\right|^2 + \frac{1}{2}\rho_{sp\perp}\sum_{ij}\left[\left(\mathbf{l}\times\nabla\right)_i d_j\right]^2 \end{aligned}$$

where $\tilde{v}_s = (2m_3/\hbar)v_s$.

The first line of terms in equation 2.1 are due to the kinetic energy of the anisotropic superfluid, the next four terms are from distortions of **l** and the final two terms are due to the bending of $\mathbf{d}$. $\rho_{s\perp}$ and $\rho_{s\|}$ are the superfluid density components perpendicular and parallel to $\mathbf{l}$ respectively and $\rho_{sp\perp}$ and $\rho_{sp\|}$ are the components of spin rigidity.

The superfluid velocity is not independent of the $\mathbf{l}$-texture, but is related through the Mermin-Ho condition (equation 1.12):

$$\nabla \times \tilde{\mathbf{v}}_{\mathbf{s}} = \frac{1}{2} \sum_{ijk} e_{ijk}\, l_i \nabla l_j \times \nabla l_k$$

The other free-energy terms which determine the texture are the dipole-dipole interaction

$$f_d = -\frac{1}{2} \lambda_D \left(\mathbf{d} \cdot \mathbf{l} \right)^2 \tag{2.2}$$

and the interaction with an external magnetic field

$$f_h = \frac{1}{2} \Delta\chi \left(\mathbf{d} \cdot \mathbf{H} \right)^2 \tag{2.3}$$

where λ_D is a positive coefficient and $\Delta\chi = \chi_\perp - \chi_\|$ is the magnetic susceptibility anisotropy.

Comparing the dipolar energy to both the gradient energy and magnetic energy gives the dipole-unlocking length, $\xi_D = (\rho_{sp\|}/\lambda_D)^{1/2} \sim 10\,\mu\text{m}$, and the dipole-unlocking field, $H_D = (\lambda_D/\Delta\chi)^{1/2} \sim 2\,\text{mT}$.

The calculations presented in the following sections make use of the following dimensionless parameters: $K_b/\rho_{sp\|} = 1.5$, $K_s/\rho_{sp\|} = 0.5$ and $\rho_{sp\perp}/\rho_{sp/\|} = 2.0$ which are values at T_c; the dimensionless slab thickness used was $D/\xi_D = 25$; and the applied field was written in units of $h_D = H/H_D$.

For length scales greater than ξ_D and $H < H_D$ then the texture can be considered as dipole-locked ($\mathbf{l} \equiv \mathbf{d}$) to a good approximation. The total free energy density then simplifies to

$$\begin{aligned} f &= \frac{1}{2} \rho_{s\perp} \tilde{\mathbf{v}}_{\mathbf{s}}^2 + \frac{1}{2} \left(\rho_{s\|} - \rho_{s\perp} \right) \left(\mathbf{l} \cdot \tilde{\mathbf{v}}_{\mathbf{s}} \right)^2 + C \left(\tilde{\mathbf{v}}_{\mathbf{s}} \cdot \nabla \times \mathbf{l} \right) - C_0 \left(\mathbf{l} \cdot \tilde{\mathbf{v}}_{\mathbf{s}} \right) \left(\mathbf{l} \times \operatorname{curl} \mathbf{l} \right) \\ &+ \frac{1}{2} K_s' \left(\nabla \cdot \mathbf{l} \right)^2 + \frac{1}{2} K_t' \left(\mathbf{l} \cdot \nabla \times \mathbf{l} \right)^2 + \frac{1}{2} K_b' \left| \mathbf{l} \times \left(\nabla \times \mathbf{l} \right) \right|^2 \\ &+ \frac{1}{2} K_4 \nabla \cdot \left[\left(\mathbf{l} \cdot \nabla \right) \mathbf{l} - \mathbf{l} \left(\nabla \cdot \mathbf{l} \right) \right] + \frac{1}{2} \Delta\chi \left(\mathbf{l} \cdot \mathbf{H} \right)^2 \end{aligned} \tag{2.4}$$

where

$$\begin{aligned} K_s' &= K_s + \rho_{sp\perp} \\ K_t' &= K_t + \rho_{sp\perp} \\ K_b' &= K_b + \rho_{sp\|} \end{aligned}$$

are the dipole-locked splay, twist and bend energy components respectively. Hence, the effect of dipole-locking is to increase the bending energy of **l**. In the Ginzburg-Landau limit ($T \to T_c$) these coefficients are equal, $K_b' = K_s' = K_t'$. All dipole-locked calculations in the following sections used this limit.

Pure divergence terms in the free-energy density were neglected in calculating textures but such terms can make a non-vanishing contribution to the total energy, so they are included in the calculations of free-energy.

The equilibrium textures are those that minimize the free energy. These were found by using the calculus of variations [40] to find the Euler equations. These were solved using commercially available software [41] using the appropriate boundary conditions and an initial guess at the solution. The processing power of modern computers has meant that what were once difficult numerical problems can now be solved much more quickly and with far greater ease.

2.3 One-dimensional textures

We consider an infinite slab of ^{3}He-A with boundaries in the xy plane and an applied magnetic field in the z-direction, $\mathbf{H} = H(\hat{\mathbf{z}})$. The influence of flow is neglected. The texture can be written as

$$\begin{aligned} \mathbf{l} &= \sin\theta(z)\,\hat{\mathbf{y}} + \cos\theta(z)\,\hat{\mathbf{z}} && (2.5) \\ \mathbf{d} &= \sin\phi(z)\,\hat{\mathbf{y}} + \cos\phi(z)\,\hat{\mathbf{z}} && (2.6) \end{aligned}$$

where θ is the angle between **l** and $\hat{\mathbf{z}}$ and ϕ is the angle between **d** and $\hat{\mathbf{z}}$. The texture is one-dimensional because both these variables are only allowed to vary in the z-direction.

The boundary conditions are

$$\theta = 0 \text{ at } z = \pm\frac{1}{2}D \tag{2.7}$$

$$\frac{d\phi}{dz} = 0 \text{ at } z = \pm\frac{1}{2}D. \tag{2.8}$$

There have been several previous theoretical studies of such textures in a slab geometry. Fetter used variational methods to obtain approximate analytical solutions [42, 43, 44], then Hook *et al.* found exact solutions numerically for both the dipole-locked [45] and dipole-unlocked [46] regimes. John Hook has also written an excellent review on the properties of a slab of ^{3}He-A in a magnetic field [47]. This section reproduces the calculations of Hook, but with a greater slab thickness.

The free-energy density in the dipole-locked ($\theta = \phi$) case is

$$f = \frac{1}{2}K_b'\left(\frac{d\theta}{dz}\right)^2 + \frac{1}{2}\Delta\chi H^2 \cos^2\theta \tag{2.9}$$

and the Euler equation is

$$K_b'\frac{d^2\theta}{dz^2} = -\frac{1}{2}\Delta\chi H^2 \sin(2\theta). \tag{2.10}$$

Solutions for the angle of $\mathbf{l}$ in the center of the slab, $\theta(0)$, and the value of θ averaged over the slab are shown in figure 2.2. The uniform texture distorts at the Fréedericksz transition field,

$$H = \frac{\pi}{D}\left(\frac{K_b'}{\Delta\chi}\right)^{1/2}. \tag{2.11}$$

The free-energy density including dipole-unlocking effects is

$$\begin{aligned} f &= \frac{1}{2}K_s \sin^2\theta\left(\frac{d\theta}{dz}\right)^2 + \frac{1}{2}K_b\cos^2\theta\left(\frac{d\theta}{dz}\right)^2 + \frac{1}{2}\rho_{sp\perp}\sin^2\theta\left(\frac{d\phi}{dz}\right)^2 \\ &\quad + \frac{1}{2}\rho_{sp\parallel}\cos^2\theta\left(\frac{d\phi}{dz}\right)^2 - \frac{1}{2}\lambda_D\cos^2(\theta-\phi) + \frac{1}{2}\Delta\chi H^2\cos^2\phi \end{aligned} \tag{2.12}$$

leading to the following Euler equations for θ and ϕ

$$\begin{aligned}
&\left(K_s \sin^2\theta + K_b \cos^2\theta\right) \frac{d^2\theta}{dz^2} \\
&= \left[\left(\rho_{sp\perp} - \rho_{sp\|}\right)\left(\frac{d\phi}{dz}\right)^2 - \left(K_s - K_b\right)\left(\frac{d\theta}{dz}\right)^2\right] \sin\theta\cos\theta \\
&+\lambda_D \cos\left(\theta - \phi\right)\sin\left(\theta - \phi\right) \qquad (2.13)
\end{aligned}$$

$$\begin{aligned}
&\left(\rho_{sp\perp} \sin^2\theta + \rho_{sp\|} \cos^2\theta\right) \frac{d^2\phi}{dz^2} \\
&= -2\left(\rho_{sp\perp} - \rho_{sp\|}\right) \sin\theta\cos\theta \frac{d\theta}{dz}\frac{d\phi}{dz} - \lambda_D \cos(\theta - \phi)\sin(\theta - \phi) \\
&-\Delta\chi H^2 \cos\phi\sin\phi. \qquad (2.14)
\end{aligned}$$

Solutions for these equations for the slab thickness used in this experiment are shown in figures 2.3, 2.4 and 2.5. Dipole-unlocking effects only become important near the slab boundaries and in fields, $H > H_D$, so in small fields the texture can be considered to be dipole-locked to a good approximation.

2.4 Effect of Orbital Ferromagnetism

The orbital ferromagnetism contributes a small energy term,

$$f_{ferro} = -\mathbf{M_l} \cdot \mathbf{H} = |M_l|\, \mathbf{l} \cdot \mathbf{H} = -M_l H \cos\theta, \qquad (2.15)$$

where M_l is the orbital magnetization. This term breaks the degeneracy between the states with **l** parallel and antiparallel to **H** since the orbital moment tends to favour being parallel to H (i.e. **l** antiparallel to **H**). The following sections describe the effect of orbital ferromagnetism on textures in a slab at low and high magnetic fields. The dimensionless value of orbital ferromagnetism used in the calculations was $M_l/(\Delta\chi H_D) = -10^{-4}$, corresponding to Leggett's estimate [21].

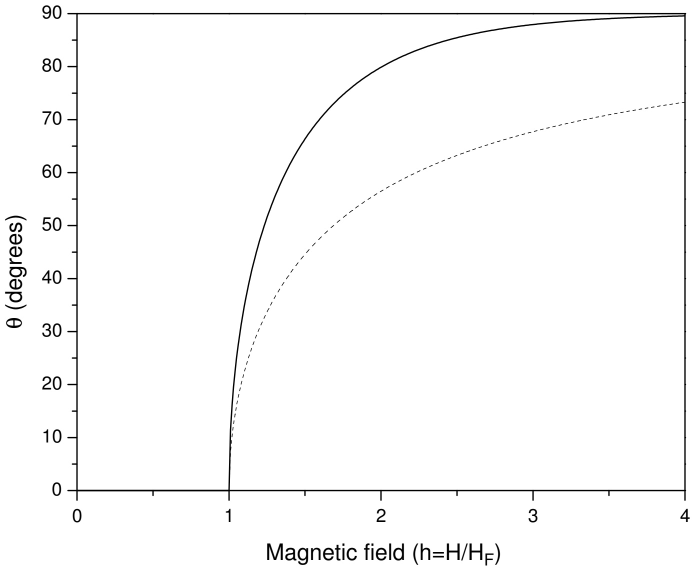

Figure 2.2: Dipole locked texture at the center of the slab (solid line) and averaged over the slab (dashed line).

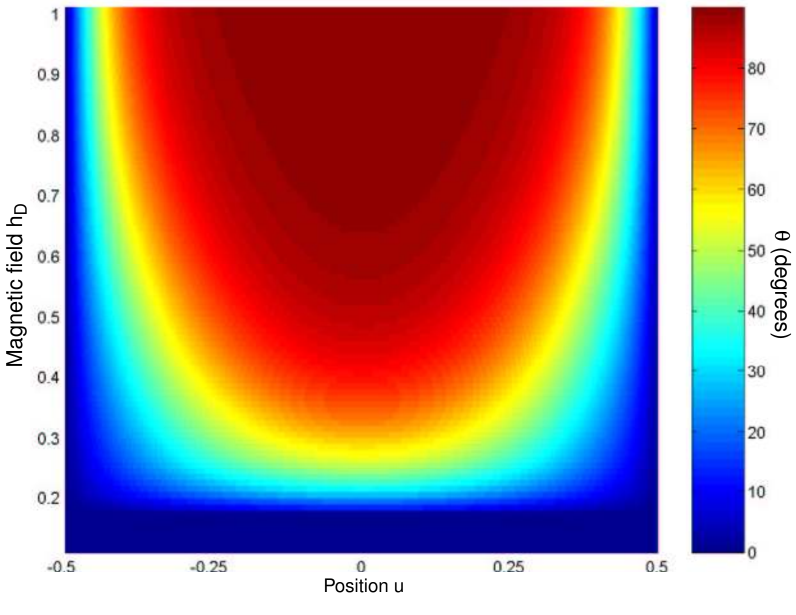

Figure 2.3: Contour plot **l**-texture for $D = 25\xi_D$. The Fréedericksz transition field $H_F = 0.19 H_D$

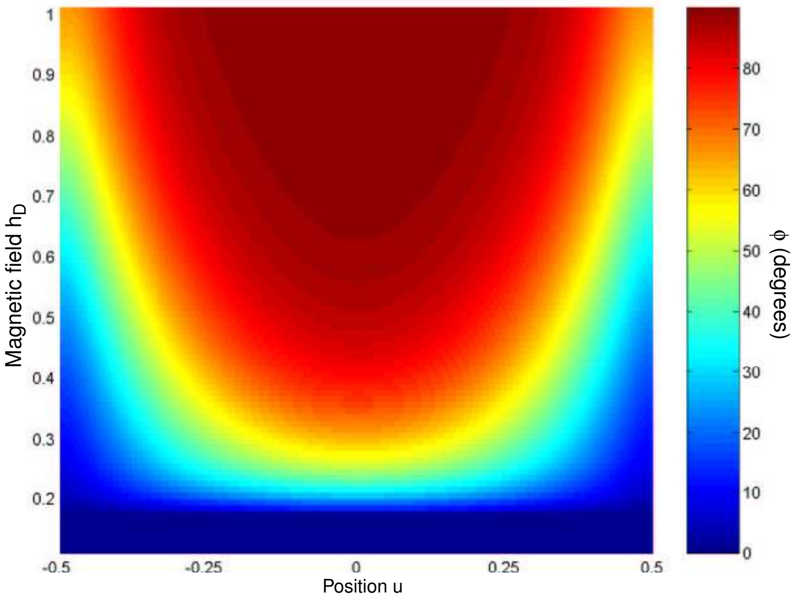

Figure 2.4: Contour plot of **d**-texture for $D = 25\xi_D$.

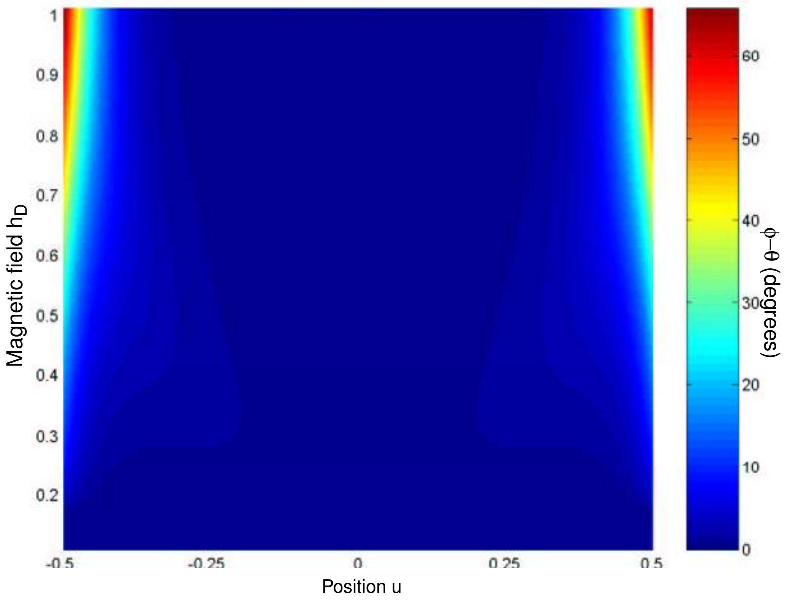

Figure 2.5: Contour plot of the angle between **d** and **l**, the dipole-unlocking angle, for $D = 25\xi_D$.

2.4.1 Low Fields

John Hook was the first to consider the effect of orbital ferromagnetism on dipole-locked textures at fields $H \simeq H_F$ [45]. The Euler equation is

$$K'_b \left(\frac{d^2\theta}{dz^2} \right) = -\frac{1}{2} \Delta\chi H^2 \sin 2\theta + M_l H \sin\theta. \tag{2.16}$$

The distortion of the texture is small when $H \simeq H_F$, so $\sin\theta \simeq \theta$, giving

$$K'_b \left(\frac{d^2\theta}{dz^2} \right) = -\theta \left(\Delta\chi H^2 - M_l H \right) \tag{2.17}$$

This has the solution

$$\theta = \theta_0 \sin kz \tag{2.18}$$

where

$$k^2 = \frac{\Delta\chi H^2 - M_l H}{K'_b}. \tag{2.19}$$

Application of the boundary conditions (equation 2.7) gives $kD = n\pi$, where n is an integer. If $n = 1$ then

$$\left(\frac{H_F}{H_{F0}} \right)^2 - \frac{M_l}{\Delta\chi H_{F0}} \left(\frac{H_F}{H_{F0}} \right) - 1 = 0 \tag{2.20}$$

where H_{F0} is the Fréedericksz transition field in the absence of orbital ferromagnetism (equation 2.11). Solving this quadratic equation to first order in $M_l/(\Delta\chi H_{F0})$ gives the modified Fréedericksz transition field

$$H_F = H_{F0} \pm \frac{M_l}{2\Delta\chi} \tag{2.21}$$

where the different signs correspond to the states where $\mathbf{l}$ is initially parallel (-) and antiparallel (+) to $\mathbf{H}$. The difference is $\Delta H_F = M_l/\Delta\chi \sim 2 - 4 \times 10^{-3}$ Gauss, which should be independent of temperature since M_l and $\Delta\chi$ have approximately the same temperature dependence. A slab of thickness 0.25 mm should have $\Delta H_F/H_F \sim 1 \times 10^{-3}$, a very small effect but one that could be measurable. Preliminary attempts to measure this effect are described in chapter 5.

2.4.2 High Fields

In order to study the effect of orbital ferromagnetism at $H > H_F$ then equation 2.15 must be added to equation 2.12 and the solutions of the Euler equations then found numerically. Figure 2.6 shows the effect of orbital ferromagnetism on the **l**-texture in the center of the slab ($\theta(0)$) for fields close to H_F.

In the absence of orbital ferromagnetism both $\theta(0)$ and $\phi(0)$ tend asymptotically towards $\pi/2$ at high magnetic fields. The orbital ferromagnetism causes the unlocking angle $|\phi - \theta|$ to increase with increasing **H** since **l** now favours being antiparallel to **H**. In this case $\theta(0)$ is approximately given by

$$\theta(0) \simeq \frac{\pi}{2} \pm \frac{M_l H}{\lambda_D} \tag{2.22}$$

where the difference in sign again corresponds to **l** either initially antiparallel or parallel to **H**.

At very high magnetic fields the ferromagnetic energy will become greater than the dipolar energy. For the case where **l** is initially antiparallel to **H** a uniform **l**-texture will be restored with **d** perpendicular to **l** everywhere. Using the small angle approximations for θ and putting $\phi = \pi/2$ simplifies the Euler equation to

$$K_b \left(\frac{d^2\theta}{dz^2} \right) = -\theta \left(\lambda_D - M_l H \right) \tag{2.23}$$

which can be solved in a similar way to the low field approximation. The critical field at which the uniform texture is restored is

$$H_c = \frac{1}{M_l} \left(\lambda_D - K_b \frac{\pi^2}{D^2} \right) \tag{2.24}$$

which is 9763 H_D for the parameters given in section 2.2. At such high fields the A1 phase is stable down to 0.7 T_c where the A-phase transition takes place [48]. At this temperature the dimensionless parameters that determine the texture are $K_b/\rho_{sp\parallel} = 2.3$, $K_s/\rho_{sp\parallel} = 0.46$ and $\rho_{sp\perp}/\rho_{sp\parallel} = 1.5$ including a strong energy gap correction of 1.24. Performing the calculations using these parameters makes only a slight change (∼1%) to the texture in the high field region, giving $H_c = 9642$.

In the case where **l** is initially parallel to **H** then at high fields the texture in the center becomes aligned in the opposite direction to that at the slab boundaries, resulting in a higher free-energy compared to the previous case. Therefore, at some point this metastable state should change to the ground state through either an extrinsic process (such as the growth of a domain of the other state) or an intrinsic process (a global instability). The value of $\theta(0)$ at high fields for both these states is shown in figure 2.7.

If the field is applied parallel to the slab boundaries ($\mathbf{H} = H\hat{\mathbf{y}}$) then **d** remains uniform ($\phi(z) = 0$) but **l** will again try to become antiparallel to **H**. The angle of **l** in the center of the slab for small distortions from the uniform texture is given by

$$\theta(0) = \frac{M_l H}{\lambda_D}\left[\frac{2\sinh(qD/2)}{\sinh qD} - 1\right] \tag{2.25}$$

where $q^2 = \lambda_D/K_b$. In the case of thick slabs the angle can be approximated as $\theta(0) \simeq -M_l H/\lambda_D$.

2.5 Two-dimensional textures

Although the above one-dimensional calculations give some useful insights into textures in a slab, a more realistic model is needed so that topological defects in the texture can be studied. In this section the textures associated with a planar domain wall and a radial Anderson-Toulouse vortex are calculated. The dipole-locked limit and the Ginzburg-Landau regime is used in both cases in order to simplify the calculations.

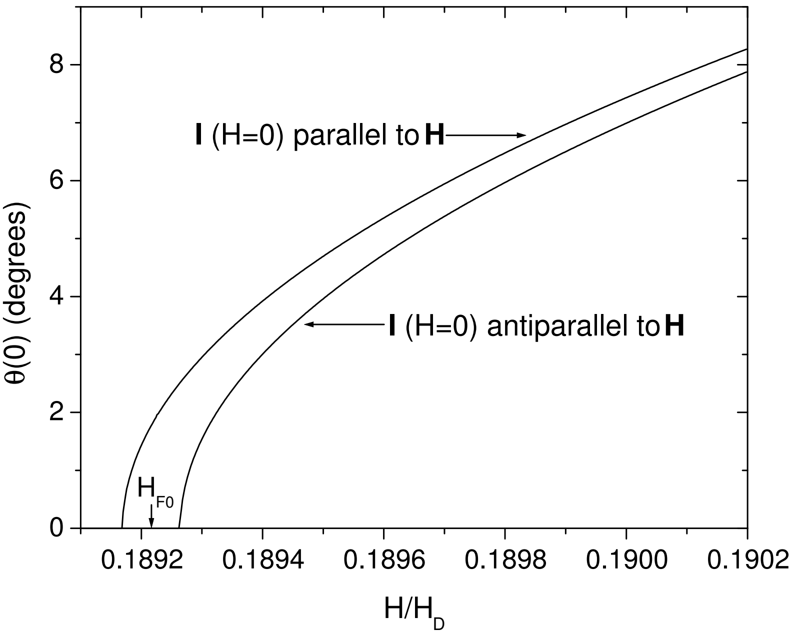

Figure 2.6: Effect of orbital ferromagnetism on Fréedericksz transition field.

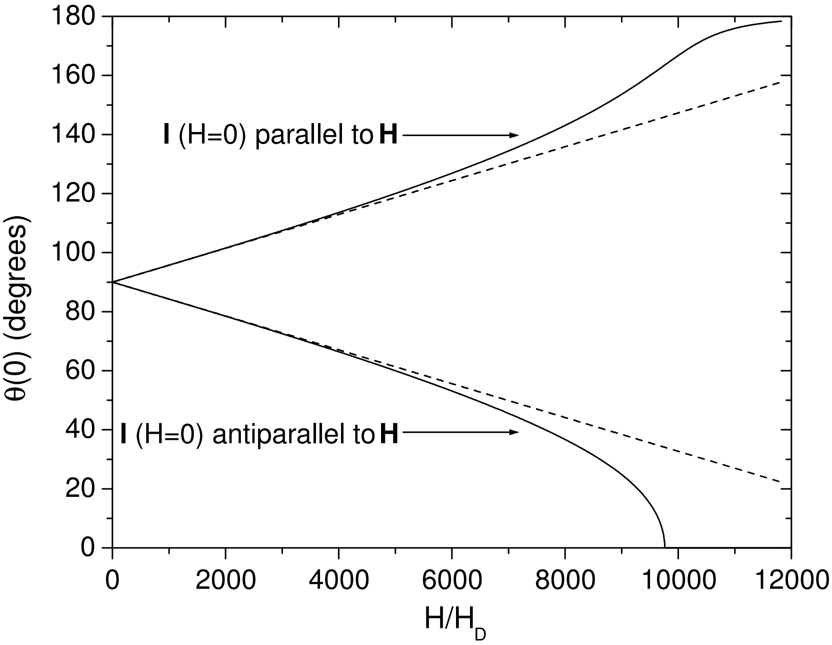

Figure 2.7: Angle between **l** and $\hat{\mathbf{z}}$ at high fields. The dashed lines show the approximate solution given by equation 2.22. The low field region (figure 2.6) cannot be resolved on this scale.

2.5.1 Domain walls

We again consider the same slab geometry as in section 2.3 but with a two-dimensional texture of the form

$$\mathbf{l} = \sin\alpha(y,z)\,\hat{\mathbf{y}} + \cos\alpha(y,z)\,\hat{\mathbf{z}} \tag{2.26}$$

which gives a free-energy density,

$$f = \frac{1}{2}K_b'\left[\left(\frac{d\alpha}{dy}\right)^2 + \left(\frac{d\alpha}{dz}\right)^2\right] + \frac{1}{2}\Delta\chi H^2\cos^2\theta. \tag{2.27}$$

The Euler equation is

$$K_b'\left(\frac{d^2\alpha}{dy^2} + \frac{d^2\alpha}{dz^2}\right) = -\frac{\Delta\chi H^2}{2}\sin 2\alpha \tag{2.28}$$

Maki [49] has found a variety of solutions to this equation in the zero field case.

A domain wall can be simulated using the boundary conditions

$$\begin{aligned} \alpha &= 0 \text{ when } z = \pm D/2 \text{ and } y < 0 \\ \alpha &= \pi \text{ when } z = \pm D/2 \text{ and } y > 0 \end{aligned}$$

which result in the **l**-texture at the boundary changing from down to up at $y = 0$. Such a situation could occur if the A-phase is independently nucleated in different regions in the slab. Such a domain wall is shown in figure 2.8. The regions of **l**-up and down are separated by a wall where **l** lies parallel to the boundaries. The width of the wall is comparable to the slab thickness. Applying a magnetic field perpendicular to the slab leads to the domain wall increasing in size but for $H < H_F$ the uniform texture is restored far away from the wall. When $H > H_F$ the bulk texture also bends over the in the center of the slab. At high fields $H > 3H_F$ the texture closely resembles that in the one-dimensional case, apart from the region close to the two line singularities at the boundaries at $y = 0$. Applying a magnetic field parallel to the boundaries would lead to the width of the domain wall decreasing. Dipole-unlocked domain walls are also possible. These occur on the boundary between domains of **l** antiparallel and parallel to **d**. An example

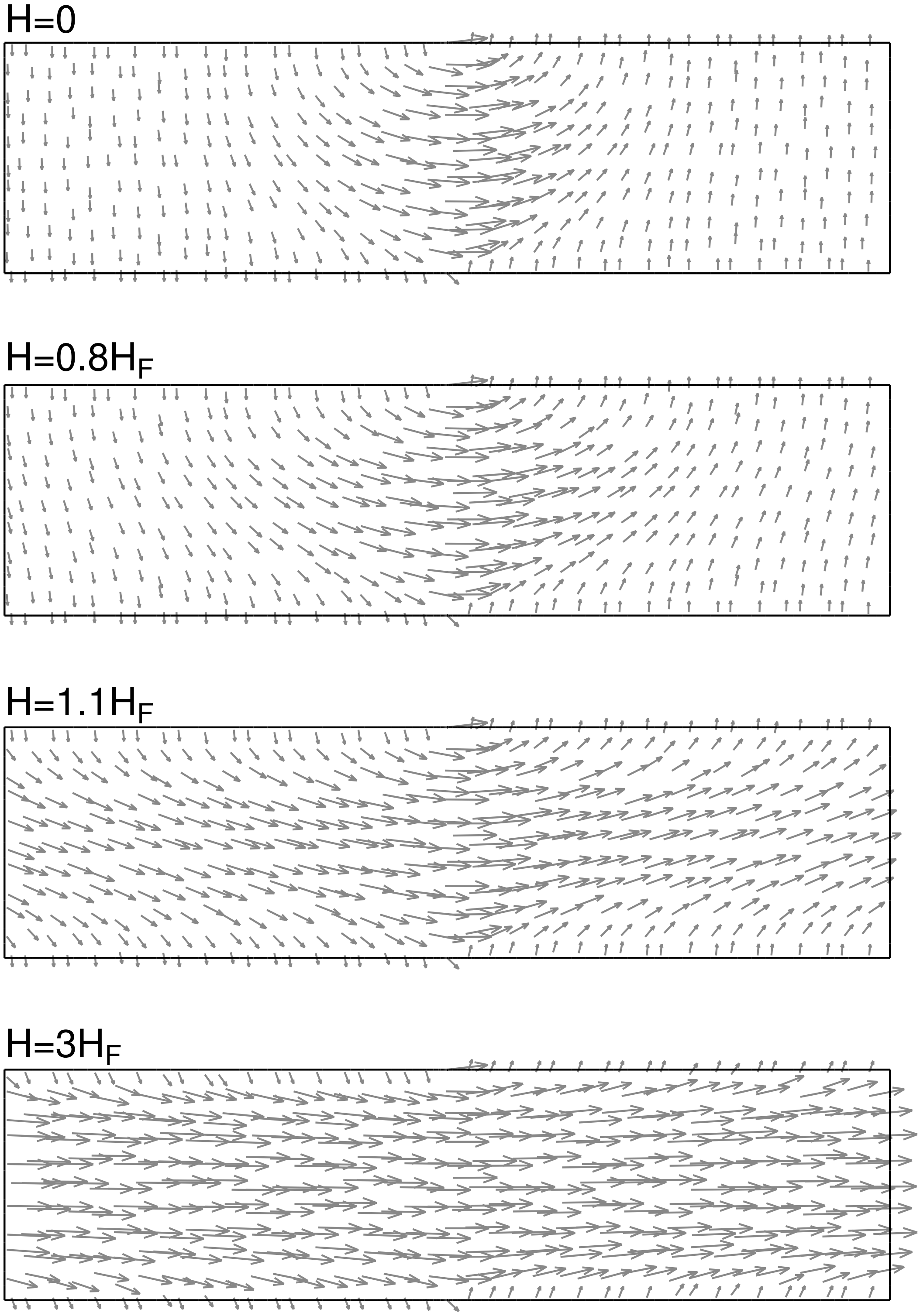

$H=0$

$H=0.8H_F$

$H=1.1H_F$

$H=3H_F$

Figure 2.8: Dipole-locked domain wall in magnetic fields applied perpendicular to the slab boundary.

would be a wall where **l** is up on one side of the wall and down on the other but **d** is in the same direction on both sides. Such a wall would have a width $\sim \xi_D$, much less than the width of the dipole-locked domain wall in order to minimize the dipolar energy contribution.

2.5.2 Radial AT Vortices

When a slab of ^{3}He-A is rotated in a low field and at low angular velocity then it is expected that an array of doubly quantized Anderson-Toulouse (AT) vortex lines are created, with the vorticity concentrated in the soft core. At the slab boundaries the vortex lines terminate in point singularities known as boojums. There are three simple types of AT vortex (see figure 2.9): radial, circular and hyperbolic. For anticlockwise circulation, the radial and circular lines are set in a uniform **l**-down texture and the hyperbolic in a uniform **l**-up texture. The direction of the texture is reversed for clockwise circulation.

The radial texture is the easiest to calculate since the **l**-texture has no azimuthal component:

$$\mathbf{l} = \sin\beta(r,z)\,\hat{\mathbf{r}} + \cos\beta(r,z)\,\hat{\mathbf{z}}. \tag{2.29}$$

Equation 1.12 is satisfied by writing the superfluid velocity in the rotating frame as

$$\tilde{\mathbf{v}}_{\mathbf{s}} = \left(\frac{1-\cos\beta}{r} - \frac{2r}{a^2}\right)\hat{\boldsymbol{\phi}} \tag{2.30}$$

where the last term ensures that the velocity (in a coordinate system rotating with angular velocity Ω) goes to zero at the outer radius of the unit cell,

$$a = \left(\frac{2\hbar}{2m_3\Omega}\right)^{\frac{1}{2}}. \tag{2.31}$$

The Euler equation is

$$\begin{aligned} K_b'\left(\frac{d^2\beta}{dr^2} + \frac{d^2\beta}{dz^2} + \frac{1}{2}\frac{d\beta}{dr} - \frac{\cos\beta\sin\beta}{r^2}\right) + \frac{1}{2}\Delta\chi H^2 \sin 2\beta \\ -\rho_\perp\left(\frac{(1-\cos\beta)\sin\beta}{r^2} - \frac{\sin\beta}{a^2}\right) = 0. \end{aligned} \tag{2.32}$$

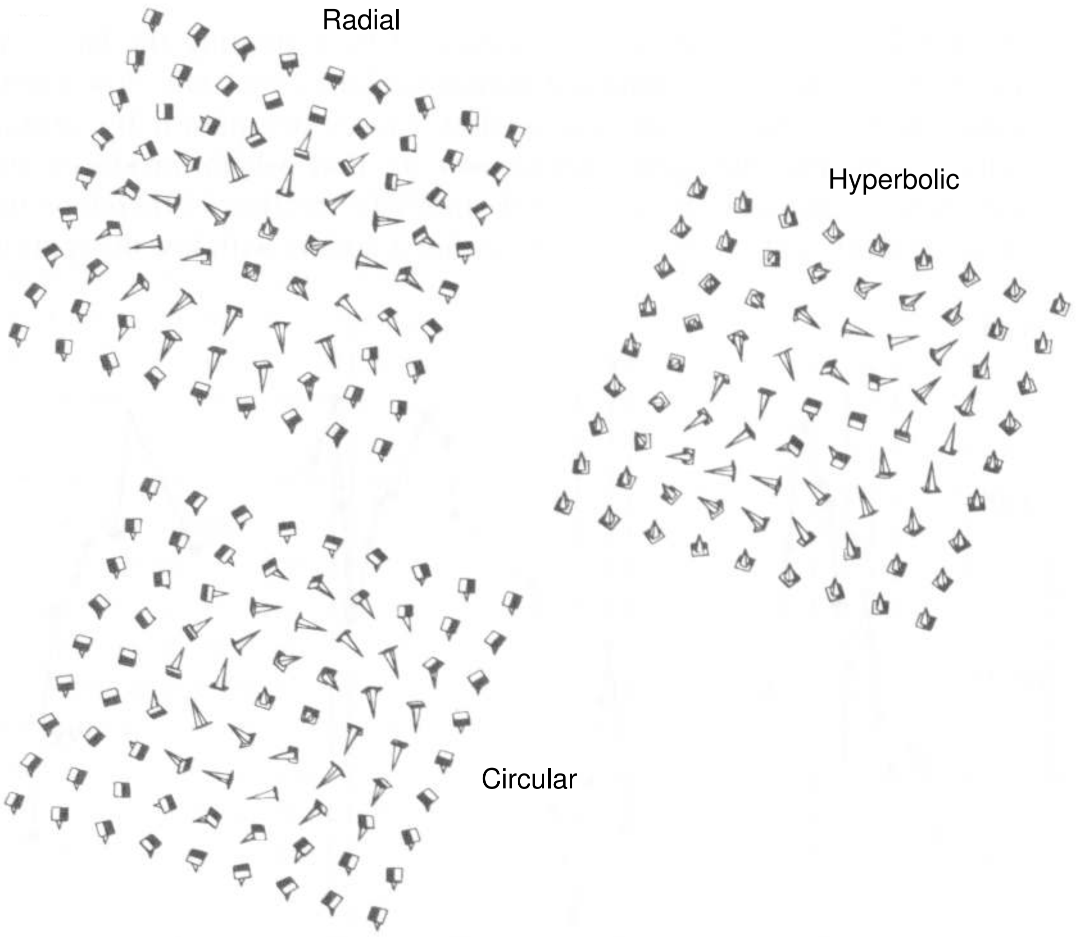
Radial
Hyperbolic
Circular

Figure 2.9: The texture and phase of three simple types of AT vortex for anti-clockwise circulation. Taken from [50].

Equation 2.32 was solved by Hu *et al.* [51] (with $a = \infty$ and $H = 0$) for both the circular and hyperbolic boojum textures in a half space. They also came up with an approximate solution for the radial AT vortex in a slab geometry and its free-energy.

The boundary conditions are

$$\begin{aligned} \beta &= 0 \text{ at } r = 0 \\ \beta &= \pi \text{ at } r = a \\ \beta &= \pi \text{ at } z = \pm D/2. \end{aligned} \tag{2.33}$$

Numerical solutions to equation 2.32 for various values of a (i.e. different angular velocities) in zero field are shown in figure 2.10. At low Ω the uniform texture is restored away from the soft core of the vortex. As Ω increases the amount of uniform texture decreases until eventually the soft core starts to get squashed inwards, increasing the bending energy.

The effect of magnetic field on the vortex texture is shown in figure 2.11. For $H < H_F$ the soft core radius grows as field increases, but the uniform texture outside the core remains. When $H > H_F$ the bulk texture also distorts and the vorticity becomes concentrated in two places: the vortex core ($r = 0$) and the outer radius of the unit cell ($r = a$). This seems to be unrealistic, it is likely that the circular symmetry used in these calculations would be broken and the texture would gain an azimuthal component [52].

When superfluid ^{3}He-A is cooled slowly through the superfluid transition whilst rotating, the vortices with the lowest free-energy should be nucleated. The free-energy of the radial AT vortices discussed above has been calculated by integrating the free-energy density over the volume of the unit cell. A small inner cut-off radius of $(D/100)$ was used in the center to avoid problems from the boojum singularities.

The free-energy of the radial AT vortex is shown in figure 2.12. At small values of a the energy tends towards that of the energy of the vortex in a geometry where

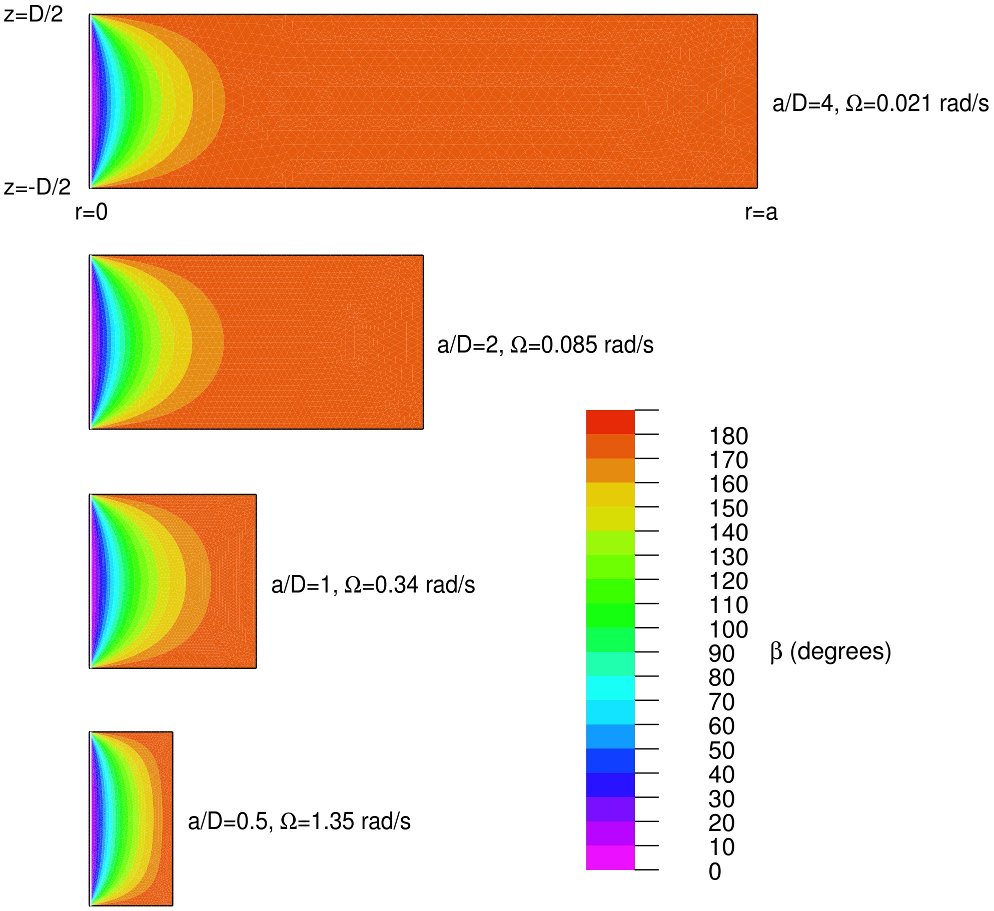

Figure 2.10: Contour plots of the texture of radial AT vortices at various angular velocities.

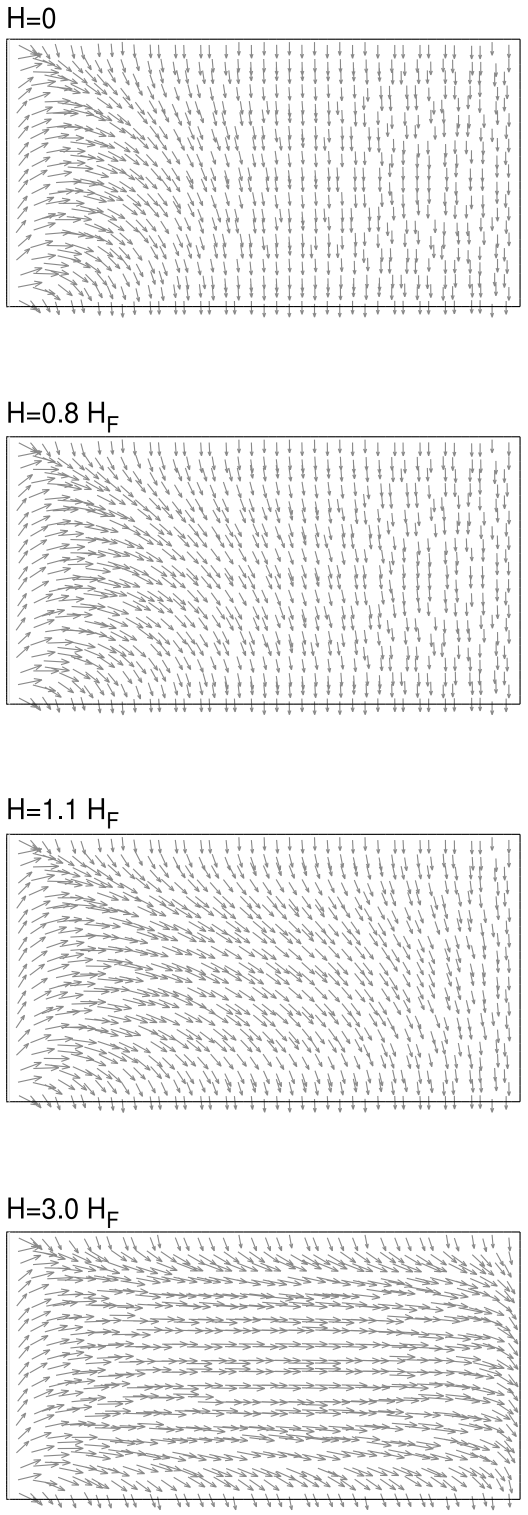

$H=0$

$H=0.8\ H_F$

$H=1.1\ H_F$

$H=3.0\ H_F$

Figure 2.11: Texture of a radial AT vortex in magnetic fields applied perpendicular to the slab boundaries.

$D = \infty$. The guessed solution of Hu *et al.* [51] is higher in energy because it is not the true free-energy minimum although it shows the same variation of energy with unit cell size when $a/D > 1$. The free energy varies logarithmically with a/D when $a/D > 1$ since outside the soft core the velocity field is inversely proportional to the distance from the vortex center.

Figure 2.13 shows the energy of the radial AT vortices in several different magnetic fields (up to H_F) as a function of angular velocity for $D = 250\,\mu m$. The magnetic contribution to the free-energy of the uniform texture, $0.5\Delta\chi H^2\pi a^2 D$, has been subtracted to give the energy of the vortex line relative to the uniform texture. The approximate free-energy of two singular phase vortices,

$$F_{2singular} = 2\pi D\rho_s \left(\frac{\hbar}{2m_3}\right)^2 \left[\ln\left(\frac{a}{\xi}\right) - \frac{3}{4}\right] \tag{2.34}$$

is also shown for comparison. The gradient for the two singular vortices($N = 1$) is half that for the AT vortex ($N = 2$) since the energy varies with N^2. For $\Omega > 0.1\,\mathrm{rad/s}$ the AT vortex has lower energy and hence is more likely to be nucleated during cooling through T_c, whereas phase vortices should occur at lower angular velocities. Application of a magnetic field leads to AT vortices becoming the equilibrium state at lower angular velocities. The phase diagram for these vortices is shown in figure 2.14.

A more complete theoretical treatment is clearly necessary to get a fuller understanding of the equilibrium vortex structures formed at T_c in a slab geometry. Three dimensional texture calculations are needed to calculate the equilibrium textures of both AT and singular vortices. Also, the circular unit cell approximation used in the above calculations should be replaced by a full calculation for an array of vortices. Dipole-unlocking effects should be included for magnetic fields $H \geq H_D$.

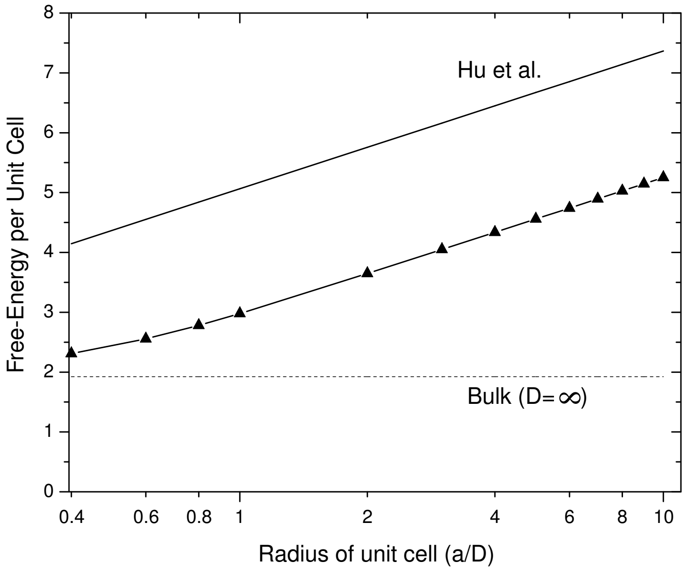

Figure 2.12: Free energy of a radial AT vortex in a slab. The energy of the same vortex in bulk and the estimated energy by Hu *et al.*[51] are also shown. The units of free energy used are $4\pi D\rho_{\perp}\left(\hbar/2m_3\right)^2$.

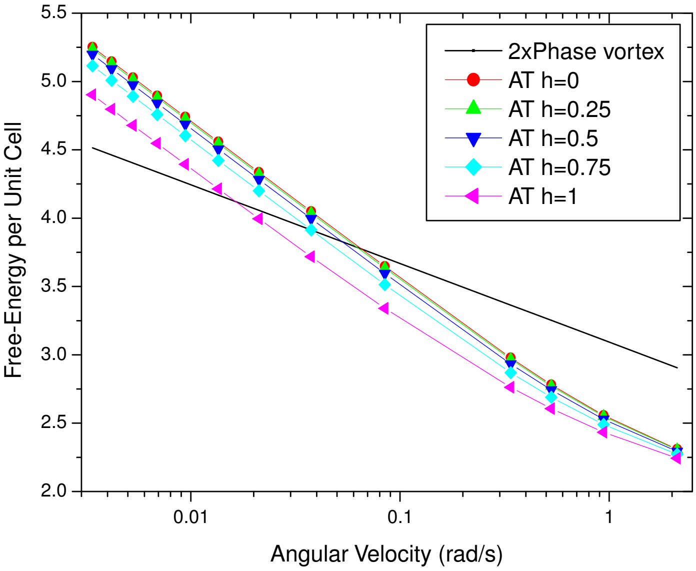

Figure 2.13: Free energy of AT vortex in a magnetic field ($h = H/H_F$) as a function of angular velocity for $D = 250\,\mu m$. The energy of two singular phase vortices (with $\xi = 1000\,\dot{A}$) is shown for comparison. The units of free energy are the same as in figure 2.12.

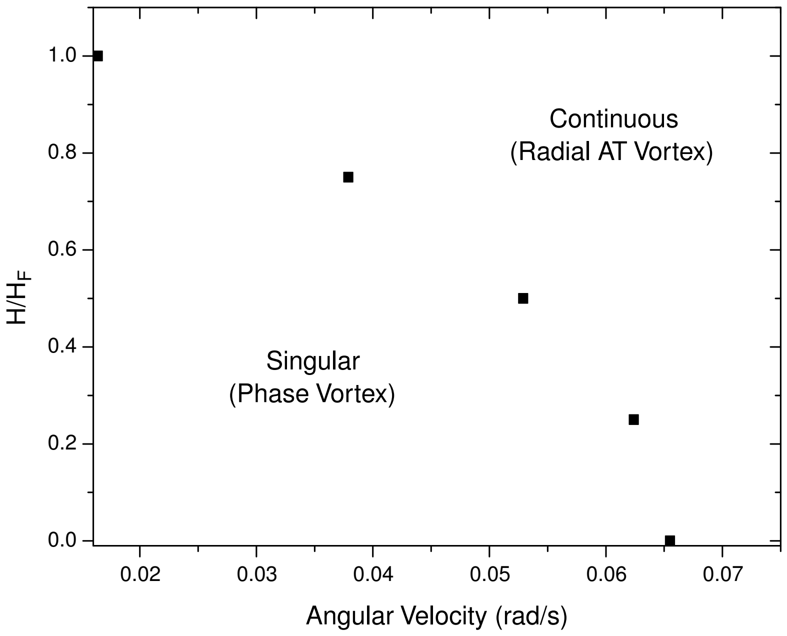

Figure 2.14: Phase diagram for singular vortex in a uniform **l** texture and continuous radial AT vortices.

Chapter 3

The Torsional Oscillator

3.1 Introduction

The original aim of this experiment was to measure the orbital ferromagnetism of ^{3}He-A and so this dictated the design of the experimental cell. Two possible methods were investigated. The first was to try to measure the orbital magnetization directly using a dc-SQUID magnetometer. Calculations showed that the maximum flux transfer in the SQUID that could be expected from several slabs of ^{3}He-A was around 5×10^{-3} flux quanta [53]. This is about the same order of magnitude as the expected noise level in the SQUID assuming that the direction of texture could be reversed on timescales of the order of hours [27], hence making any direct measurement difficult. The second possibility was to detect the influence of the orbital ferromagnetism on textural transitions such as the Fréedericksz transition and the expected effects have been described in detail in the previous chapter. There are several techniques that are sensitive to textures in ^{3}He-A [47], although no method has yet been developed that allows the texture across the whole slab to be determined (such as those used for liquid crystals [54]). Instead the techniques currently available for ^{3}He-A are sensitive to the average texture and a model is then needed to compare with the experimental data. A torsional oscillator was chosen for this experiment, a technique that was first used in a superfluid experiment by Andronikashvili [55], where he measured the normal fluid density of ^{4}He by using a stack of parallel plates suspended on a torsion fibre. The resonant frequency of a torsional oscillator is

$$\nu_0 = \frac{1}{2\pi}\sqrt{\frac{C}{I}} \tag{3.1}$$

where I is the moment of inertia of the torsion head and C is the torsion constant of the oscillator.

3.2 Equations of motion

The hydrodynamics of a slab of superfluid ^{3}He-A (with thickness D and radius R) contained in a torsional oscillator have been extensively discussed by Hook *et al.* [46, 56]. The following is a brief outline of the equations of motion of a torsional oscillator.

The angular motion of the slab boundaries (contained in the xy plane) about the z-axis is

$$\mathbf{\Omega_w} = \Omega_0\, e^{i\omega t}\, \hat{\mathbf{z}}. \tag{3.2}$$

If the fluid is isotropic, incompressible and irrotational then the equation of motion can be written as

$$\rho_n \frac{\partial v_n}{\partial t} = \eta \frac{\partial^2 v_n}{\partial z^2} \tag{3.3}$$

where η is the viscosity of the fluid. The solution is

$$\mathbf{v_n} = \frac{r\Omega_0\, e^{i\omega t}\cosh(Kz)}{\cosh\left(KD/2\right)}\, \hat{\boldsymbol{\phi}}, \tag{3.4}$$

where

$$K = (1+i)\left[\frac{\rho_n \omega}{2\eta}\right]^{1/2}. \tag{3.5}$$

The reciprocal of the real part of K is the viscous penetration depth, $\delta = \sqrt{2\eta/\rho\omega}$, which describes how far the shear waves generated at the container boundaries travel into the fluid. A correction for fluid slip at the boundaries can be introduced [56] but the slip length is negligible in comparison to the slab thickness for this experiment.

The force exerted per unit area on the container walls at $z = \pm D/2$ by the fluid is

$$\mathbf{F} = -\eta \left[\frac{\partial \mathbf{v_n}}{\partial z} \right]_{z=\pm D/2} \tag{3.6}$$

and it is convenient to write the force per unit area on the walls in dimensionless form $(F_1 + iF_2)$ using

$$2\mathbf{F} = -iD\rho\omega(F_1 + iF_2) r\Omega_0 \, e^{i\omega t} \, \hat{\boldsymbol{\phi}} \tag{3.7}$$

hence giving

$$F_1 + iF_2 = \frac{\rho_n}{\rho} \frac{\tanh{(KD/2)}}{KD/2}. \tag{3.8}$$

F_1 and F_2 are related to the resonant frequency (ν_R) and bandwidth (ν_B) of the torsional oscillator by

$$(\nu_R - \nu_0) = -AF_1 \tag{3.9}$$

$$(\nu_B - \nu_{NB}) = -BF_2 \tag{3.10}$$

where A and B are related constants given by

$$2A = B = \frac{\pi \nu_0 \rho R^4 D}{2I} \tag{3.11}$$

and ν_{NB} is the non-hydrodynamic contribution to the bandwidth which is found to be negligible in comparison to the hydrodynamic contribution to the bandwidth at mK temperatures in this experiment.

3.3 Construction

The torsion head, shown in figure 3.1, was made in two halves from Stycast 1266 epoxy. The top piece was made from a 4mm thick by 15mm diameter piece which was polished on both sides using a lapping machine. The finest abrasive used was $3\mu m$ powder making the Stycast transparent and enabling the completed cell cavity to be inspected with a microscope.

The bottom piece was made by casting Stycast against a polished aluminium negative. When the Stycast had set the piece was machined to the required 15 mm diameter and most of the excess aluminium was removed. The depression for the head of the torsion rod and the fill line were also machined. Any remaining aluminium was then slowly etched away using a solution of 3 molar NaOH.

The pieces were designed so that when they were pushed together a gap 0.25 mm thick and 10 mm diameter would be left. A small amount of freshly mixed Stycast was added to the corner of the female half and the pieces were pushed together and rotated by hand until the contact surface had been completely covered. The cell was then clamped in a vice until the epoxy had set. The 1 mm reinforcement cavity around the circumference of the cell was then filled by adding partially set epoxy whilst the cell was slowly rotated in a lathe. The cell was left to rotate until the Stycast has set, then any excess epoxy was machined away. The completed cell was inspected with a microscope to check that no epoxy had leaked into the cavity.

The torsion rod used in this experiment (see figure 3.3) was machined from a piece of 1 inch diameter ‘half-hard’ BeCu rod [57]. It was then thoroughly degreased before being heat treated at $315°C$ for two hours in a helium atmosphere. The cell was then lightly glued to the head of the torsion rod before the head was covered with Stycast.

A second torsion rod (the lower torsion rod on figure 3.3) was made in the same way but with a resonant frequency ~ 140 Hz. This rod acted as a vibration filter to prevent unwanted vibration from reaching the upper torsion rod. The two oscillators were sealed together using an indium o-ring.

3.4 Magnetic shielding and DC coil

The magnetic field in the z-direction was provided by a superconducting coil of length 35 mm and diameter 22 mm wound from 0.1μm diameter NbTi wire with a CuNi matrix. The main winding had 592 turns on 2 layers and there was an inner notch at both ends with 100 turns on 5 layers. The room temperature resistance of the coil was $3.3\,k\Omega$. The calculated field profile along its axis is shown in figure 3.2. The calculations were performed by treating each turn as a circular loop [58] and then summing over all the loops. The calculated coil constant, including the effect of the superconducting shield [59], is 125.0 Gauss/A.

A Nb cylinder was used as a magnetic shield. The cylinder was open at one end and the other was closed apart from 3 small holes used to hold the coil in place. PTFE and Stycast spacers was used to hold the coil firmly in position inside the shield as well as ensuring their axes were aligned. The shield (and coil) was then suspended from the mixing chamber of the cryostat and the torsional oscillator was attached to the nuclear demagnetization stage via an indium o-ring seal. The overall cell assembly is shown in figure 3.3.

3.5 Electronics

The torsional resonance of the oscillator was driven and detected electrostatically. The circuits used are shown in figure 3.4, similar to those used in a previous Manchester torsional oscillator experiment [60]. The electrodes were made from brass and these were positioned against the flat face of the vibration filter, so that there was a small gap, d, separating the electrodes from the flat face. Bias voltages, $V_0 \simeq 270$ V, were provided by 30 9V batteries wired in series. The torsional oscillator was driven with a sinusoidal signal, $V_1 e^{i\omega t}$, provided by an Agilent 33120A synthesizer. The current generated by the motion of the torsional oscillator, i_d, was amplified by a current sensitive SR570 pre-amplifier and then

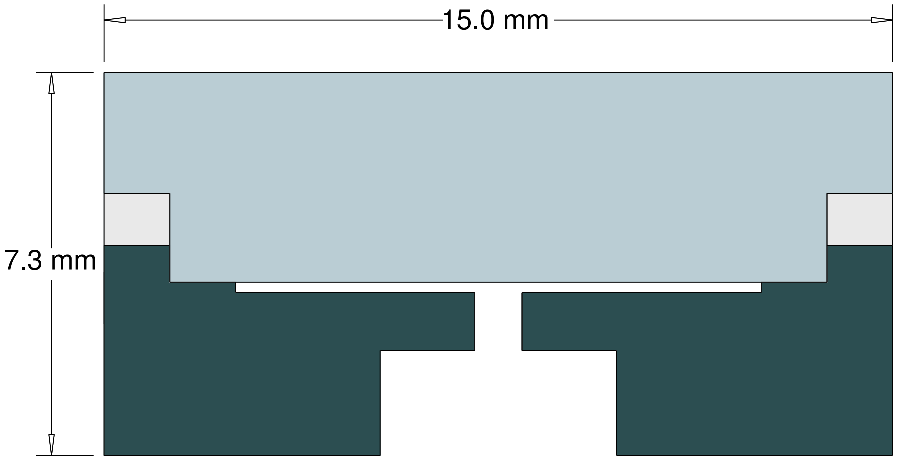

Figure 3.1: Scale diagram of the Stycast 1266 torsion head.

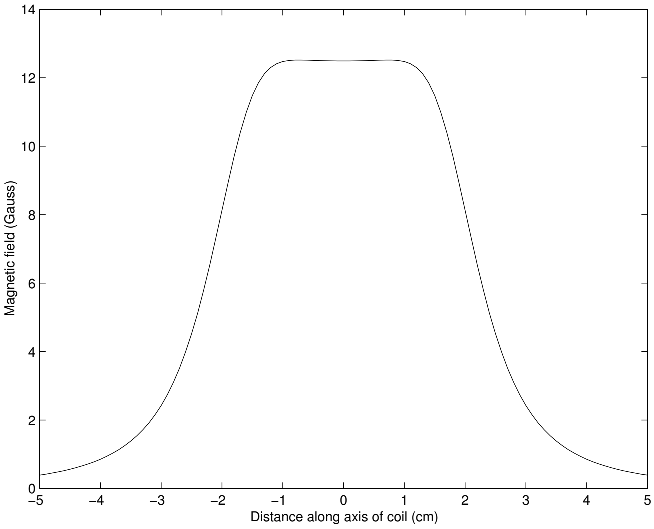

Figure 3.2: Magnetic field profile along axis of coil for a current of 100mA. The effect of the Nb shield has been taken into account.

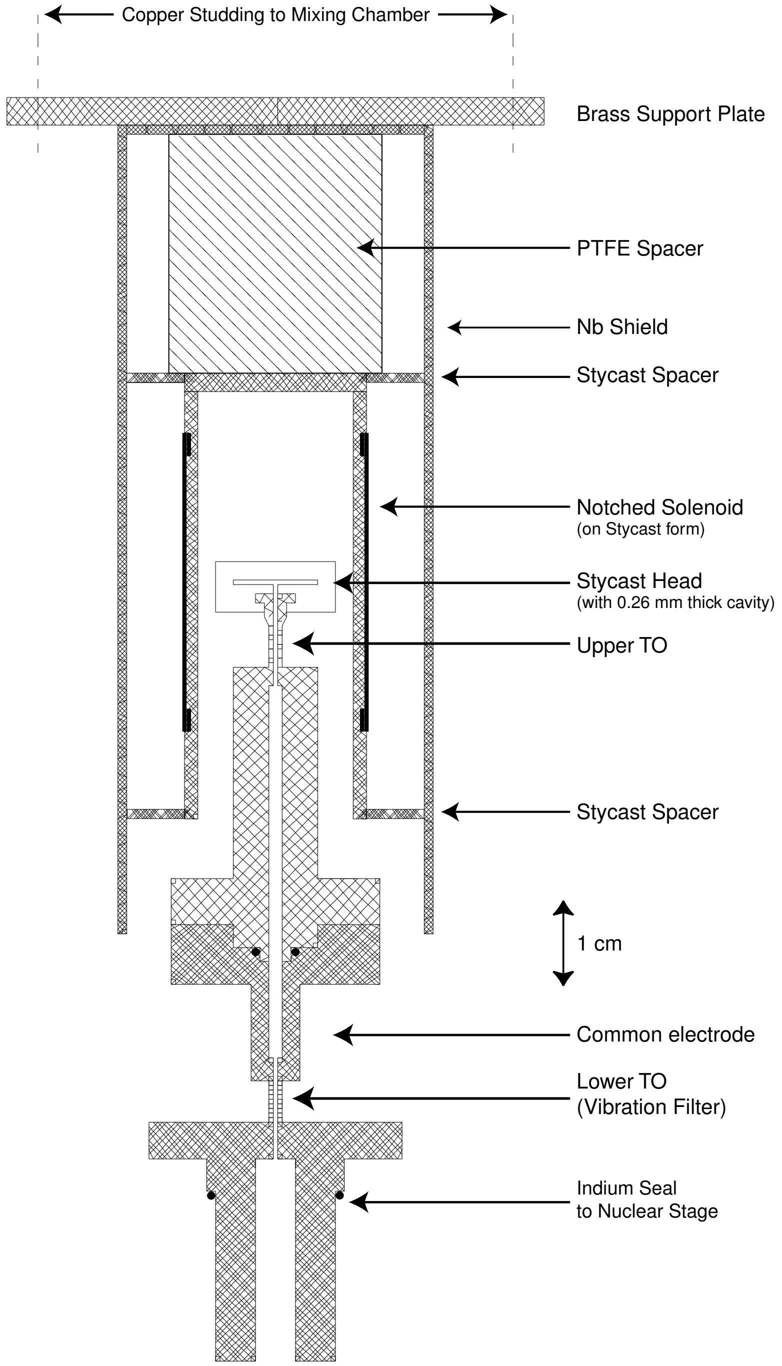
Copper Studding to Mixing Chamber
Brass Support Plate
PTFE Spacer
Nb Shield
Stycast Spacer
Notched Solenoid
(on Stycast form)
Stycast Head
(with 0.26 mm thick cavity)
Upper TO
Stycast Spacer
1 cm
Common electrode
Lower TO
(Vibration Filter)
Indium Seal
to Nuclear Stage

Figure 3.3: Experimental setup. The superconducting shield and DC coil were suspended from the mixing chamber. The two torsional oscillators were attached to the nuclear stage of the cryostat. Another shield constructed from mu-metal was later placed around the niobium shield in order to reduce the amount of trapped magnetic field (see chapter 5). Most of the measurement presented in the following chapters were taken with this second shield in place.

measured with a SR830 lock-in amplifier.

The force acting on the drive electrode (with capacitance C) is

$$F \simeq \frac{CV_0^2}{2d} + \frac{CV_0V_1e^{i\omega t}}{d} \tag{3.12}$$

and the current entering into the pre-amp is

$$i_d \simeq iV_0C_1e^{i\omega t} \tag{3.13}$$

where C_1 is the amplitude of the AC component of the capacitance of the detect electrode.

3.6 Control Method

The routine used to control the torsional oscillator was originally devised by John Hook and is outlined briefly below.

The torsional resonance is a lorentzian. The in-phase and quadrature voltages measured by the lock-in (V_x and V_y respectively) can be written as

$$V_x + iV_y = \frac{iCV_d/2}{\nu_R - \nu + i\nu_B/2} \tag{3.14}$$

where V_d and ν are the drive voltage and frequency. C is a constant known as the torsional oscillator constant which can be determined at resonance ($\nu = \nu_R$), giving

$$V_{x0} = \frac{CV_d}{\nu_B} \tag{3.15}$$

where V_{x0} is the in-phase voltage at resonance.

The torsional oscillator was calibrated by sweeping ν through the resonance (figure 3.5 shows an example). A least squares fit to a lorentzian curve then gave the phase, C and the offsets on V_x and V_y. The phase was adjusted so that V_x was a maximum (V_{x0}) on resonance.

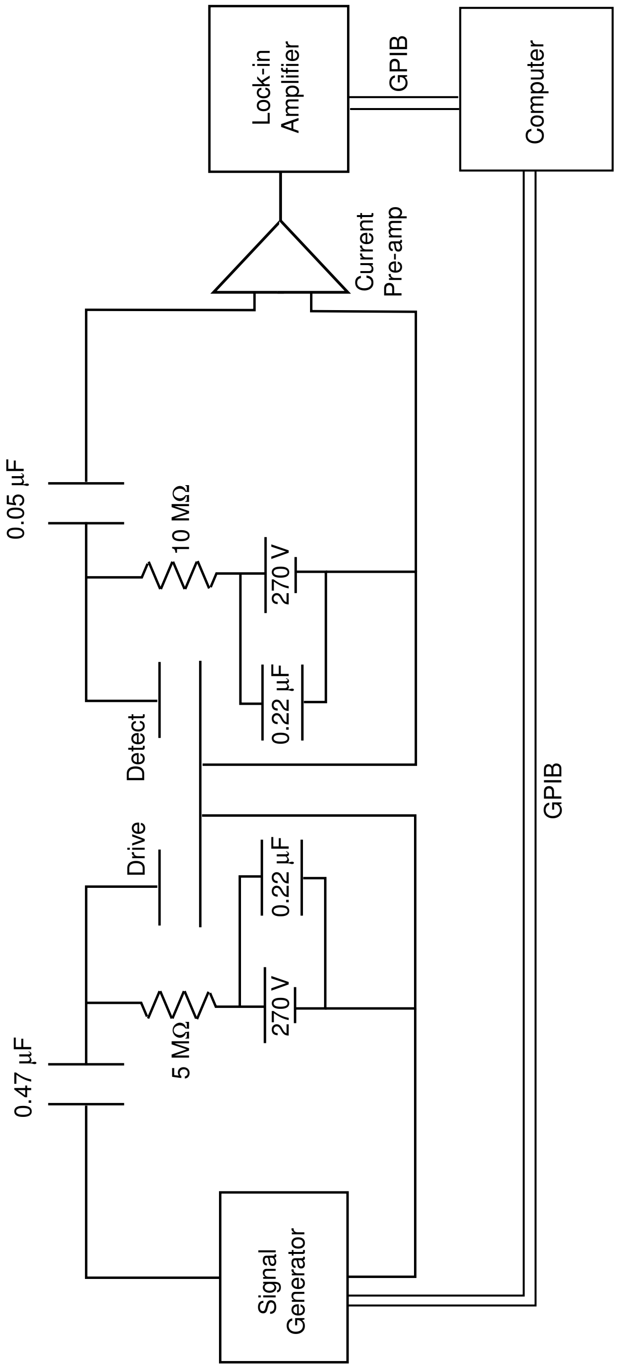
Lock-in Amplifier
GPIB
Computer
Current Pre-amp
0.05 µF
10 MΩ
270 V
0.22 µF
Detect
Drive
0.22 µF
270 V
5 MΩ
0.47 µF
GPIB
Signal Generator

Figure 3.4: Circuit used for driving and detecting the motion of the torsional oscillator. The 0.05 μF capacitor used on the detect side is a metallised polypropylene film capacitor that was found to have the lowest DC current leakage compared to various other types of capacitor.

The torsional oscillator control program used several results that follow from equation 3.14:

$$\begin{aligned} V_{x0} &= V_x + \frac{V_y^2}{V_x} && (3.16) \\ \nu_B &= \frac{CV_d}{V_{x0}} && (3.17) \\ \nu_R &= \nu + \frac{\nu_B V_y}{2V_x}. && (3.18) \end{aligned}$$

Usually the oscillator was driven near resonance. The lock-in outputs were monitored by the computer and ν_R and ν_B were calculated. If the current ν was more than $0.1\nu_B$ away from ν_R then the drive frequency would be changed towards ν_R by an amount typically $0.1(\nu_R - \nu)$, so that the oscillator was always being driven at a frequency close to the resonant frequency. The drive voltage was kept constant, usually at 250 mV.

The torsional oscillator was calibrated by plotting the resonant frequency against bandwidth for normal ^{3}He over an approximate temperature range 2.5 mk to 20 mK. The hydrodynamic equations 3.8 and 3.9 were fitted to the curve using A,B and ν_0 as adjustable parameters. Such a curve and the corresponding fit are shown in figure 3.6. The fit parameters obtained were $A = 177.6$ mHz, $B = 353.4$ mHz, $\nu_0 = 628.3653$ Hz. The value of $A/B = 0.503$ deviates from the theoretically predicted value of 0.5 by 0.5%, a good indication that the behaviour of the oscillator is well described by the hydrodynamic theory outlined in section 3.2.

3.7 Thermometry

Most experiments conducted at millikelvin temperatures use an independent thermometer. The Manchester Rotating Cryostat was fitted with two such devices, an LCMN and a vibrating wire thermometer [60], during the course of this experiment. However, due to technical reasons neither of these thermometers functioned properly. Hence the behaviour of the torsional oscillator itself was used to provide a temperature scale for both normal ^{3}He and ^{3}He-A with a uniform texture.

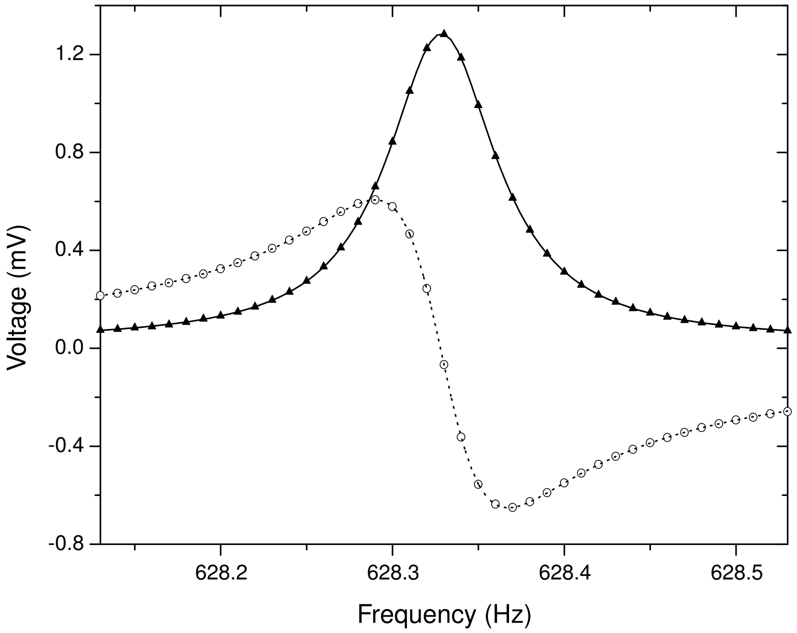

Figure 3.5: Resonance curve for the torsional oscillator containing ^{3}He at 29 bar and 17 mK. The triangles and circles are the in-phase (V_x) and quadrature (V_y) voltages respectively.

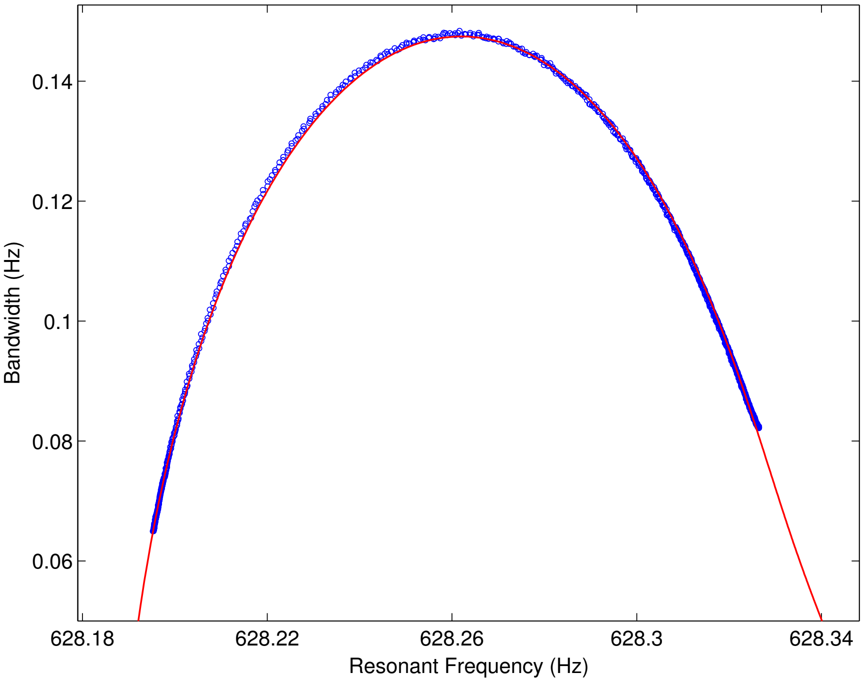

Figure 3.6: Hydrodynamic curve for normal ^{3}He . The solid line is a fit using the theory described in section 3.2 with the fit parameters given in section 3.6. The high frequencies correspond to high temperatures where $\delta < D$ and the low frequencies to temperatures just above T_c where $\delta > D$. The maximum in the bandwidth occurs when $\delta \sim D$.

3.7.1 Normal ^{3}He

The calibration parameters given in the previous section can be used to convert measured values of ν_R and ν_B into values of F_1 and F_2 which can then be used to find $x = D/2\delta$ using

$$\frac{F_1}{F_2} = \frac{B(\nu_R - \nu_0)}{A(\nu_B - \nu_{NB})} = \frac{\tan x\left(1 - \tanh^2 x\right) + \tanh x\left(1 + \tan^2 x\right)}{\tan x\left(1 - \tanh^2 x\right) - \tanh x\left(1 + \tan^2 x\right)}. \tag{3.19}$$

The values of ν_R and ν_B at the superfluid transition were used to accurately determine the slab thickness D since the density and viscosity of ^{3}He at the superfluid transition have been measured and hence the viscous penetration depth at T_c, δ_c is known. This showed that $D = 260 \pm 2\,\mu m$.

The viscosity of the normal fluid is then given by

$$\eta = \frac{\pi\rho\nu_R}{4x^2}. \tag{3.20}$$

Several groups have made detailed measurements of the viscosity of normal ^{3}He . Carless *et al.* [61] used a vibrating wire to show that the viscosity at 29.3 bar is well determined by

$$\eta = \frac{1}{7.10T^2 + 14.5} \tag{3.21}$$

where T is the temperature in mK according to the Alvesalo temperature scale [62], which needs to be multiplied by a factor of 0.89 [12] to agree with accepted temperature scales.

Combining equations 3.20 and 3.21 gives the temperature in terms of parameters that can be obtained from the torsional oscillator,

$$T = 0.89\left[\frac{1}{7.10}\left(\frac{4x^2}{\pi\rho\nu_R D^2} - 14.5\right)\right]^{\frac{1}{2}} \text{ mK}. \tag{3.22}$$

Figure 3.7 shows how resonant frequency varies as a function of temperature for normal ^{3}He .

3.7.2 Superfluid ^{3}He-A

The measured values of ν_R and ν_B were again used to find x using equation 3.19. The component of superfluid density perpendicular to **l**, $\rho_{s\perp}$, was then found by using equation 3.8. Hook *et al.* [56] found that $\rho_{s\perp}$ as a function of temperature was to a good approximation given by the theoretical equation

$$\rho_{s\perp} = \frac{4\alpha}{1 + \frac{1}{3}F_1^s(1 - 4\alpha)} \tag{3.23}$$

where F_1^s is a Fermi liquid parameter and α is an integral given by

$$\alpha\left(\frac{\Delta}{k_B T}\right) = \frac{3}{8}\int_0^{\pi/2} d\theta \sin^3\theta \left[1 - Y_0\left(\frac{\Delta \sin\theta}{k_B T}\right)\right] \tag{3.24}$$

where Δ is the A-phase energy gap, k_B is Boltzmann's constant and Y_0 is a Yosida function. They found that their data fitted best when Δ was multiplied by a factor of 1.24, which allows for the effects of strong coupling. The calculation of $\Delta/k_b T$, α and Y_0 are discussed in appendix B of [56].

The reduced temperature as a function of resonant frequency is shown in figure 3.8. The temperature of the transition from B-phase to A-phase calculated using the above method deviates by $\leq 1\%$ from the accepted value. This discrepancy is perhaps due to the non-uniform textures created during such a transition, showing that the frequency and bandwidth shifts due to non-uniform textures in zero field are small and that the thermometry is still accurate to a good approximation.

3.8 Textures in a slab of ^{3}He-A in a torsional oscillator

There are several ways in which a uniform **l**-texture can distort when a vertical magnetic field is applied. John Hook and co-workers [46, 56] have considered three possible ways in which a one-dimensional texture (see section 2.3) can distort. They are radial, azimuthal and planar and are illustrated in figure 3.9. The

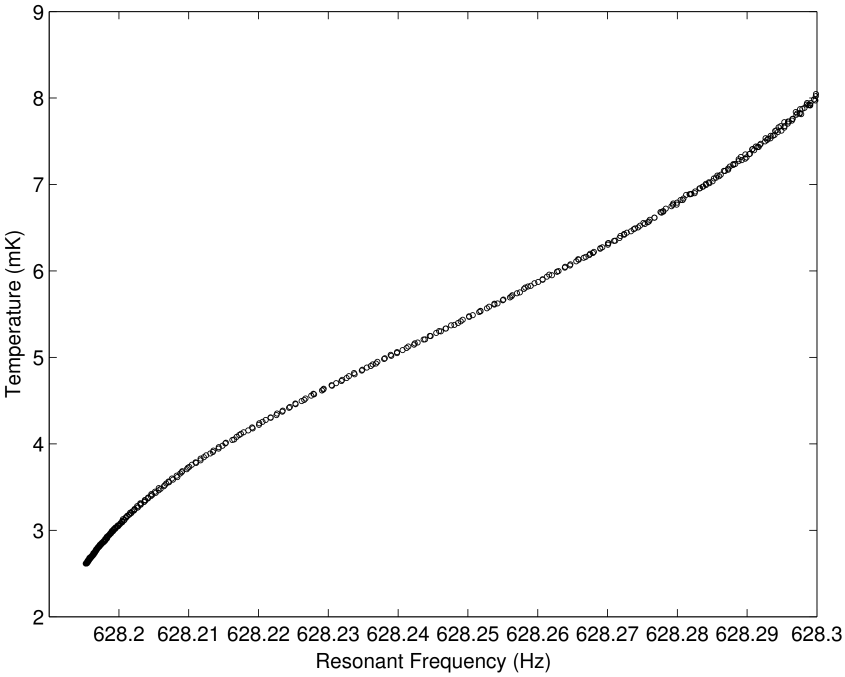

Figure 3.7: Temperature as a function of resonant frequency for normal ^{3}He .

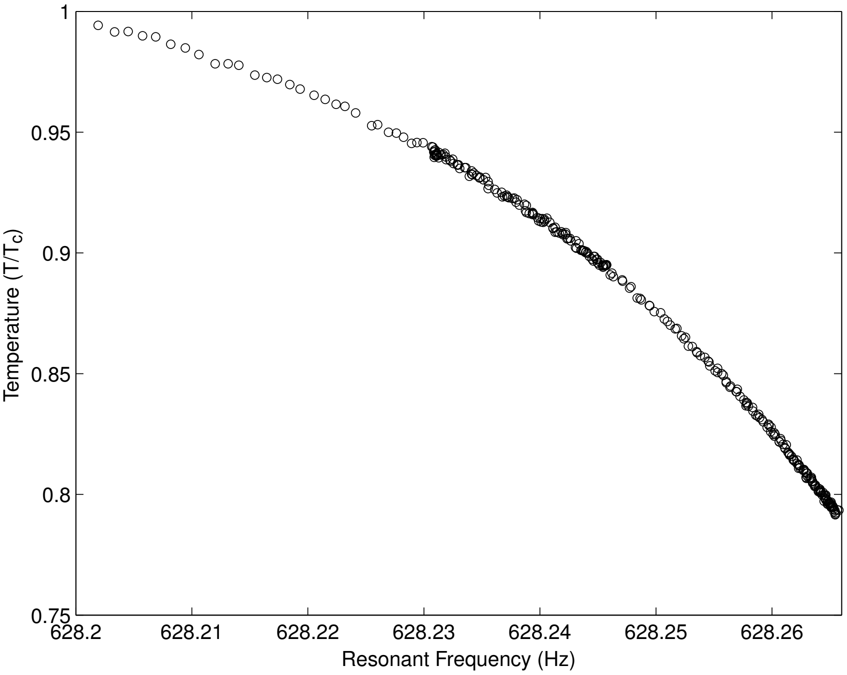

Figure 3.8: Temperature as a function of resonant frequency for superfluid ^{3}He-A
.

textures for these transitions can be written as

$$\begin{aligned}\text{Radial:}\quad \mathbf{l} &= \sin\theta\,\hat{\mathbf{r}} + \cos\theta\,\hat{\mathbf{z}}\\ \text{Azimuthal:}\quad \mathbf{l} &= \sin\theta\,\hat{\boldsymbol{\phi}} + \cos\theta\,\hat{\mathbf{z}}\\ \text{Planar:}\quad \mathbf{l} &= \sin\theta\,\hat{\mathbf{y}} + \cos\theta\,\hat{\mathbf{z}}.\end{aligned}$$

The type of distortion that will occur can depend on several factors. Applying the magnetic field at a non-zero angle to the slab normal results in a planar texture, or if the field had a radial component then a radial texture could be formed. Azimuthal textures can be made to occur by increasing the drive velocity amplitude to a value where the oscillatory flow is large enough to influence the texture.

The hydrodynamic equations for each of these have been described in detail in [46] and so are not repeated here. The shifts in F_1 and F_2 are different for each of these distortions since the contribution from different components of the viscosity and superfluid density tensors is different for each distortion. Hook *et al.* [56] were able to find values for the five independent coefficients of viscosity and the anisotropy in superfluid density $(\rho_{s\perp} - \rho_{s\|})$ by fitting the hydrodynamic theory to measured values of F_1 and F_2 for planar textures produced by applying the field at an angle to the slab. These values, and the textures calculated in section 2.3, have been used to calculate the expected shifts in F_1 for the three different distortions including the effect of orbital ferromagnetism for cases when the applied field is parallel and antiparallel to $\mathbf{l}$. These predictions for low fields are shown in figure 3.10 although the magnitude of the orbital moment used is two orders of magnitude greater than expected in order to make the differences between the two states visible.

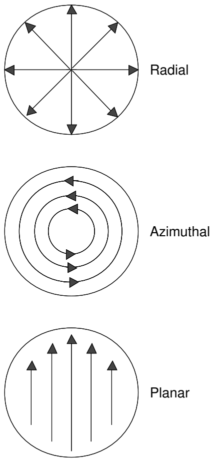

Figure 3.9: Three possible ways in which the texture in a slab can distort. The effect of the slab boundaries upon **l** have not been included.

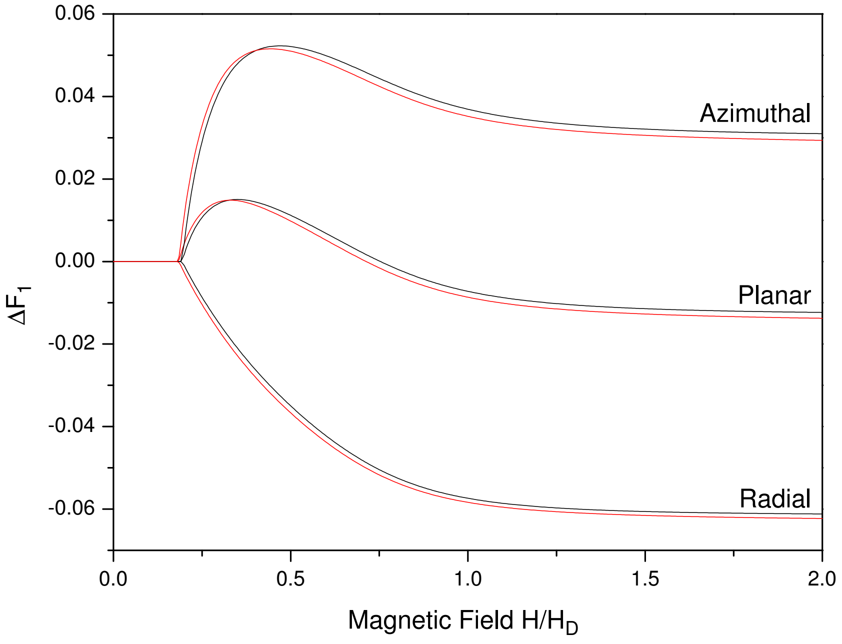

Figure 3.10: Change in F_1 (i.e. resonant frequency) as a function of applied magnetic field for azimuthal, planar and radial textures. The red and black lines are for the states with **l** initially parallel and antiparallel to **H** respectively. The difference between the two is due to the orbital magnetic moment. In this case the magnitude of the orbital moment is 100 times the predicted value [21] in order to make the differences between the two states visible.

Chapter 4

The Rotating Cryostat

4.1 Introduction

The experiments described in this thesis were performed using the Manchester Rotating Cryostat. Detailed descriptions of the cryostat have been given elsewhere [63, 64], so only a brief overview is given in the following section. The main purpose of this chapter is to document some of the changes that have been made to the cryostat in order to make this work possible. No discussion of the cryogenic techniques necessary for all low temperature experiments is given. An excellent account of such methods can be found in [59].

During the early stages of the experiment the time that the ^{3}He liquid could be maintained in the superfluid A-phase was severely limited by a large heat leak, which is described in section 4.3. Detailed studies of vibration of the cryostat have been carried out and these are detailed in section 4.4, followed by a description in section 4.5 of how these problems were overcome.

4.2 Overview of the cryostat

The rotating cryostat is shown schematically in figure 4.1. The cryostat is housed in a shielded room that rests upon a 70 tonne concrete block whose foundations are isolated from those of the main physics building. The dewar and cryogenic insert are hung from a circular aluminium platform and racks containing electrical instruments are attached to the top of this platform. A drive pulley, suspended from the roof of the shielded room, is connected to the rotating platform by a tetrahedral aluminium frame and a plywood disc so that lateral forces are not transmitted to the platform. The pumping and gas lines needed for the dilution fridge pass through rotating vacuum seals and electrical power and instrument communication is passed through a slip ring. The rotating platform is supported by air bearings mounted on a triangular frame. There are three circular thrust pads to provide lift and three rectangular lateral pads which define the axis of rotation of the cryostat. The compressor which supplies air bearings was upgraded to a more powerful model and the three circular thrust pads were redesigned in order to provide more lift. The cryostat is rotated using a stepper motor located outside the shielded room. A rubber belt couples the drive from the motor to the drive pulley. Gearing has been added during this work such that the motor now has to rotate 55/15 times faster in order to achieve the same angular velocity as before. This has improved the stability of the rotation since noise from the motor steps is less at higher motor speeds. Another beneficial effect is that both the minimum angular velocity (7×10^{-3} rad/s) and acceleration ($10^{-3}\,\text{rad/s}^{-2}$) have been reduced.

The dilution refrigerator is an Oxford Instruments 400 unit that has been modified so that the still pumping line is on the axis of rotation. The nuclear demagnetization stage [63] consists of a large piece of slotted copper attached to the mixing chamber using three vespel supports. Thermal contact to the ^{3}He liquid is provided by several copper discs coated in silver sinter. The nuclear stage is cooled by the mixing chamber via a thermal link consisting of several silver wires and an aluminium superconducting heat switch. The demagnetization magnetic field is

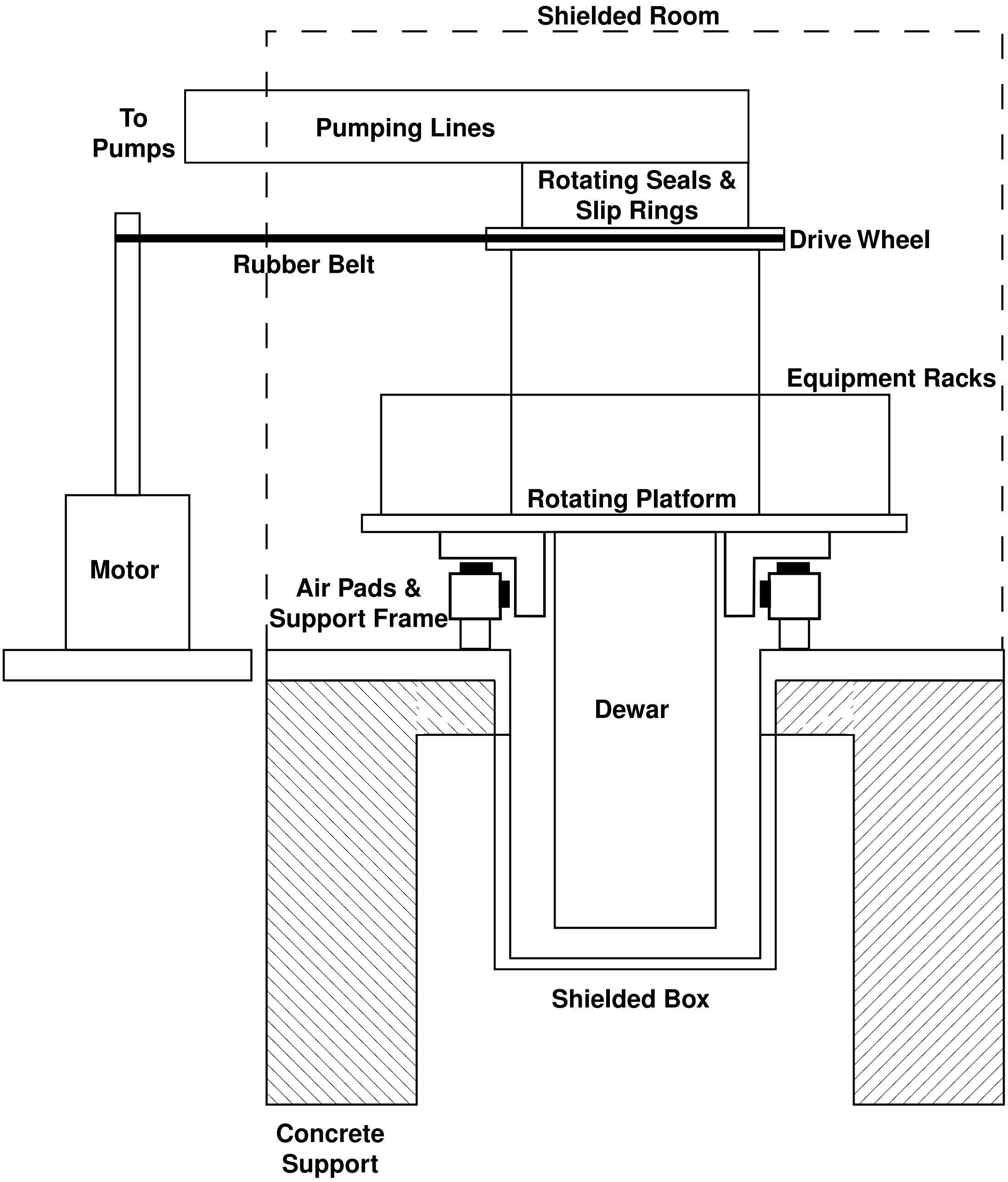
Shielded Room
To Pumps
Pumping Lines
Rotating Seals & Slip Rings
Drive Wheel
Rubber Belt
Equipment Racks
Rotating Platform
Motor
Air Pads & Support Frame
Dewar
Shielded Box
Concrete Support

Figure 4.1: Schematic diagram of the rotating cryostat. Access to the lower part of the cryostat is through a pit within the concrete block. The shielded room is completed by raising a steel box around the lower part of the cryostat. The three legs which support the cryostat were replaced by air springs during the course of this work (see section 4.5)

provided by an 8 Tesla Oxford Instruments superconducting solenoid mounted on the outside of the vacuum can. The nuclear stage was typically cooled for three days in an 8 T field prior to demagnetization reaching a temperature of around 15 mK.

The bottom of the nuclear stage is fixed to the inner radiation shield using nylon cord that is threaded between a vespel ring, that slides over a Stycast peg on the bottom of the copper piece, and a brass ring attached to the inside of the radiation shield to form a cartwheel structure. The inner and outer radiation shields and the outer radiation shield and vacuum can are held together in a similar way.

4.3 The heat leak problem

During early runs of the experiment it was discovered that there was a large heat leak into the nuclear stage which varied with the time of day and the demagnetization field. The heat leak reached a maximum value of about 1 μW, with a demagnetization field of 1 T, in the morning and decayed in the evening to a value around 300 nW overnight. This reduced the time taken to warm from the B-A phase transition to the normal state (a temperature difference of 0.36 mK at 29.34 bar) to a few hours, making the experiment very difficult to perform. In low demagnetization fields of around 0.1 T the heat leak was approximately 5 nW.

The heat leak varied approximately with the square of the demagnetization field, indicating that the problem was due to vibration. Any electrical conductor that vibrates in a magnetic field will generate eddy current heating [59],

$$\dot{Q}_e = PV\dot{B}^2/\rho_R, \tag{4.1}$$

where V and ρ_R are the volume and electrical resistance of the conductor, $\dot{B}$ is the time derivative of magnetic field seen by the conductor and P is a factor which depends upon the geometry of the conductor. Vibration measurements described in the next section show that the heat leak was chiefly due to external vibration causing relative motion between the nuclear stage and the demagnetization solenoid.

The heat leak was calculated using

$$\dot{Q} = \frac{n\lambda_n B^2}{\mu_0}\left(\frac{1}{T_1} - \frac{1}{T_2}\right)\frac{1}{\Delta t}, \tag{4.2}$$

where n is the number of moles of refrigerant in the main field, λ_n is the molar nuclear Curie constant of the refrigerant and Δt is the time taken for the nuclear stage to warm from temperature T_1 to T_2. In our case, $n = 4$ and $\lambda_n = 4 \times 10^{-12}$ Km^3/mol for Cu resulting in equation 4.2 becoming

$$\dot{Q} = \frac{8.576\, B^2}{\Delta t}\left(\frac{1}{T_1} - \frac{1}{T_2}\right), \tag{4.3}$$

where the temperatures are in mK and the magnetic field B is given as a percentage of the maximum field (8 T).

4.4 Vibration measurements

4.4.1 Vibration detectors

Extensive measurements of vibration were carried out in many places in the laboratory using Geospace GS11-D vertical vibration detectors [65]. Figure 4.2 shows the electrical circuit used to monitor the output of the vibration detectors. The output of each detector was passed through a low pass filter and then amplified using EG&G voltage preamplifiers with the gain set to 1000. The pre-amp output was then passed to a Hewlett Packard 54600A oscilloscope that was used to store several seconds of data (typically 4 s). A PC then took a fast Fourier transform of the stored signal so that the vibrations could be analyzed in terms of their frequency components.

The vertical vibration detectors showed that all parts of the lab suffered from vibration in the 5-30 Hz range, although the amplitude varied considerably between positions. Several example vibration spectra are shown in figure 4.3. The rotating platform was found to have the highest level of vibration and floating the platform on the air bearings made little difference. The platform level was two to three orders of magnitude greater than the level observed on the concrete block and the floor of the shielded room, suggesting that the cryostat had at least one mechanical resonance that was being excited by the vibration of the supporting concrete block. This was tested by attaching a mechanical oscillator to the platform. The oscillator was driven at a set frequency and the output of the vibration detector at the drive frequency was measured using a lock-in amplifier. The lock-in outputs as a function of drive frequency are shown in figure 4.4 for a vibration detector on the rotating platform and the horizontal coil on the bottom of the nuclear stage. Both of these show a large peak at ~ 13 Hz and some other peaks at higher frequencies.

A plot of the level of vibration on the rotating platform summed between frequencies from 5 to 30 Hz is shown in figure 4.5. There is a clear increase in vibration at 7am, followed by several other peaks during the daytime and a gradual decrease in the evening. This pattern is approximately the same each weekday but the amplitudes are three to four times lower during the weekend and the peaks are less sharp. The source of the vibration is unclear but the most likely candidate are buses and other heavy vehicles on the major road that is a short distance from the lab, although this has not been directly verified.

4.4.2 Search coils

The relative motion of the nuclear stage and the demagnetization solenoid was measured by placing four identical small coils, each with 3150 turns of Cu wire, in several different positions on the nuclear stage. Figure 4.6 shows where each of the coils was placed. Two were attached to the underside of the experimental platform and the other two to the very bottom of the slotted Cu piece, with the axis of the coils in each pair perpendicular to one another.

The voltage generated by motion of the coils in the magnetic field was measured and converted to a fast Fourier transform using exactly the same process and circuit as that used for the vibration detectors (figure 4.2). Example frequency spectra from the search coils are shown in figure 4.7. The peaks on the spectra are at exactly the same frequencies as the peaks on the vibration spectra obtained on the rotating platform (figure 4.3). The coil with the largest amplitude signal was the one at the bottom of the nuclear stage whose axis was perpendicular to the rotational axis of the cryostat, indicating that the Cu nuclear stage was moving like a solid pendulum. The summed voltage for frequencies between 5 Hz and 30 Hz as a function of time of day for this particular coil and the horizontal coil on the experimental platform are shown in figures 4.8 and 4.9. They both show a very similar time dependence to the vibrations of the platform.

4.5 Solutions to the vibration problem

Vibration isolation is one of the key elements in the design of modern cryostats (for example see [66]) and although care was taken to try and minimize the effects of vibration in the design of the rotating cryostat it still causes problems. There are several approaches that could be taken to solve the problem. One would be to try and eliminate the source of vibration but this is clearly not viable. Another would be to isolate the cryostat from the vibrations of the concrete block and a third would be to prevent motion of the nuclear stage relative to the solenoid by securing them together more firmly. The changes made were a combination of the latter two approaches.

The first substantial change was to anchor a steel I-beam onto each of the two beams on the roof of the shielded room that support the weight of the drive pulley and rotating seals. This was done in order to stiffen the existing beams and prevent them from flexing. This slightly reduced the amplitude of vibration on the rotating platform but made very little difference to heat leak.

The next major change made was to install three Firestone Airmount 224 air springs [67] under each corner of the triangular support frame. Most of this work was performed by Derek Cousins and Steve May. The air springs have a natural frequency of around 2 Hz and hence are able to isolate the cryostat from most of the vibration occurring in the concrete block. Figure 4.10 shows how the air springs have been incorporated. Each air spring is housed in an aluminium container that limits the maximum horizontal and vertical movement to a few millimeters. This is needed in case the air bearings (or the compressor) fail which would lead to friction between the cryostat and the bearings and as a consequence a large torque on the support frame would be exerted and hence a shearing force on the air springs if their horizontal motion was not constrained. The pressure in each air spring is controlled by a Newport levelling valve [68] positioned adjacent to each leg which acts to keep the air springs inflated to a constant height. The compressed air is supplied by the compressor that also supplies both sets of air bearings.

Figure 4.11 shows vibration spectra measured on the rotating platform with the air springs inflated. The vibration is at least three orders of magnitude smaller than before the air springs were fitted (see figure 4.3a). There is also a peak at $\sim$2.5 Hz which corresponds to the natural frequency of the air springs.

The motion between the nuclear stage and magnet has been reduced by doubling the number of spokes on each of the three cartwheels that hold the bottoms of the nuclear stage, radiation shields and vacuum can together. The most notable difference this has made is that the cryostat is now much less sensitive to disturbance caused during helium and nitrogen transfers and also when the cryostat is accidently knocked. The dilution unit was also stiffened by inserting extra support rods between the still plate and the plate below the concentric heat exchanger.

The heat leak, with the air springs inflated and the improved cartwheels installed, is now ≤ 10 nW at a demagnetization field of 1 T, an improvement of two orders of magnitude compared to the situation before the air springs were installed. This means that the time taken for the experiment to warm through temperature region of the A-phase at 29 bar at constant field is now one week, even with many hours of rotation each day. The cryostat has been rotated up to 1 rad/s with the air springs inflated without any problems. There is some low frequency vibration ($\sim$2-5 Hz) when the cryostat is rotating but this does not cause any significant increase of the heating of the nuclear stage. Overall, the improvements have made a considerable difference and the cryostat is performing better than ever.

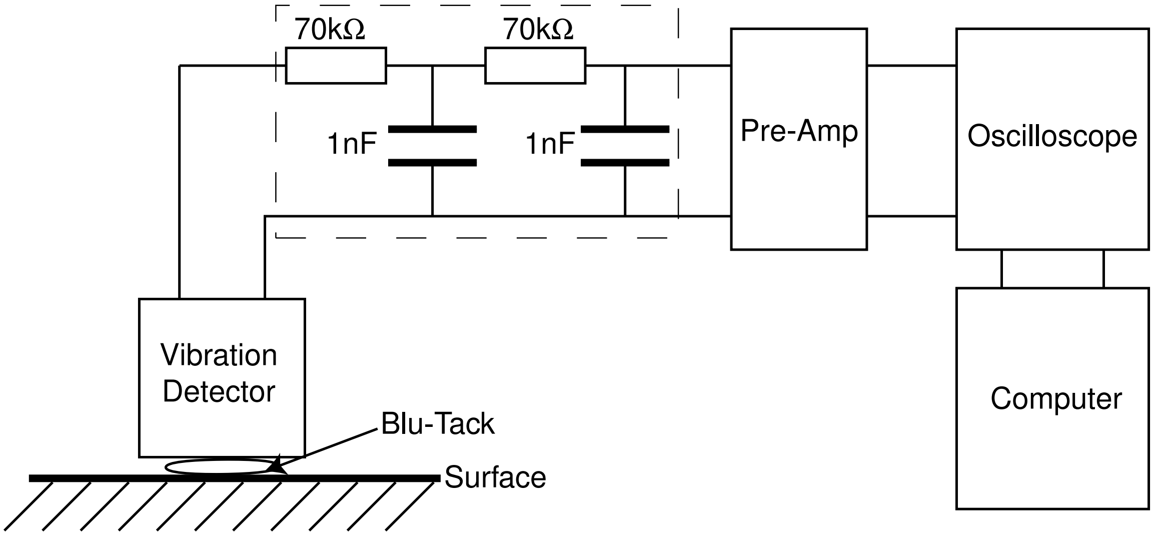
70kΩ
70kΩ
1nF
1nF
Pre-Amp
Oscilloscope
Vibration Detector
Computer
Blu-Tack
Surface

Figure 4.2: Circuit used to obtain vibration spectra.

(a) Rotating platform

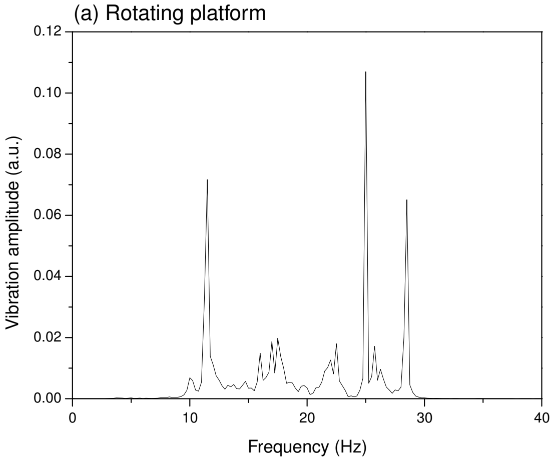

(b) Concrete block

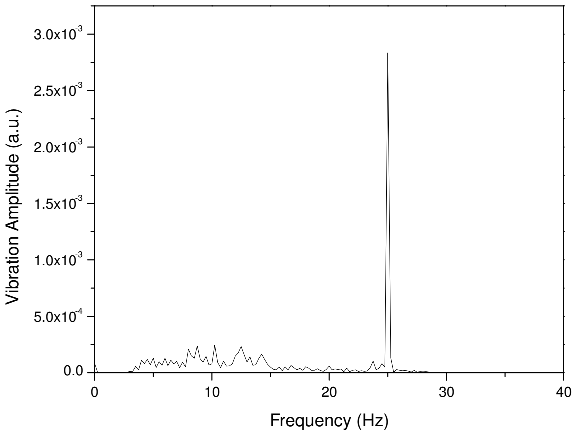

(c) Basement cryostat

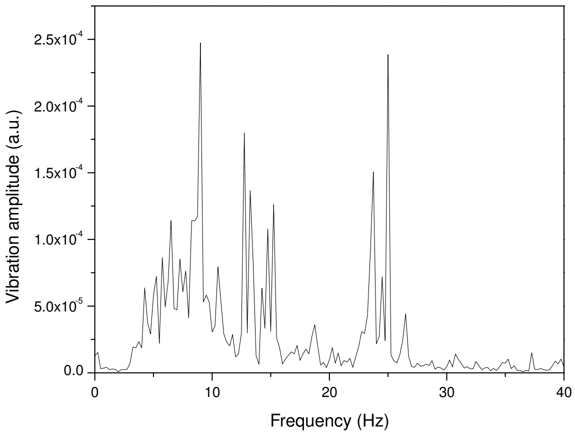

Figure 4.3: Example vibration spectra on (a) the rotating platform, (b) the concrete block which supports the rotating cryostat and (c) on the support frame of the other Manchester demagnetization cryostat which is located in the basement.

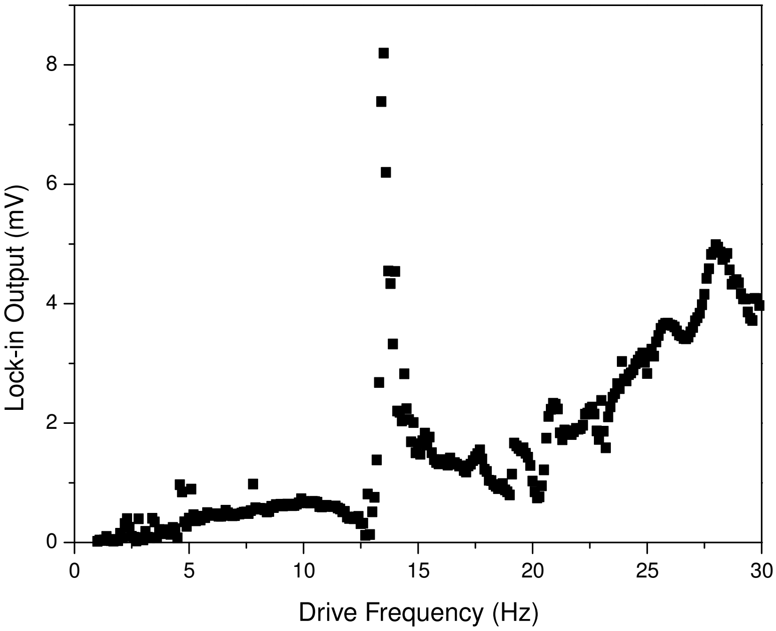

(a) Rotating platform

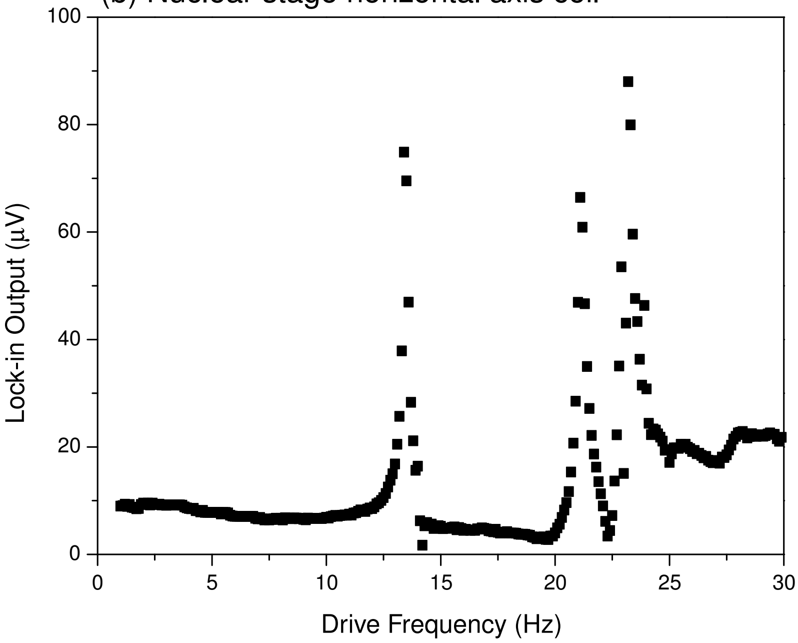

(b) Nuclear stage horizontal axis coil

Figure 4.4: Resonance curves for (a) vibration detector on rotating platform and (b) horizontal coil on the bottom of the nuclear stage.

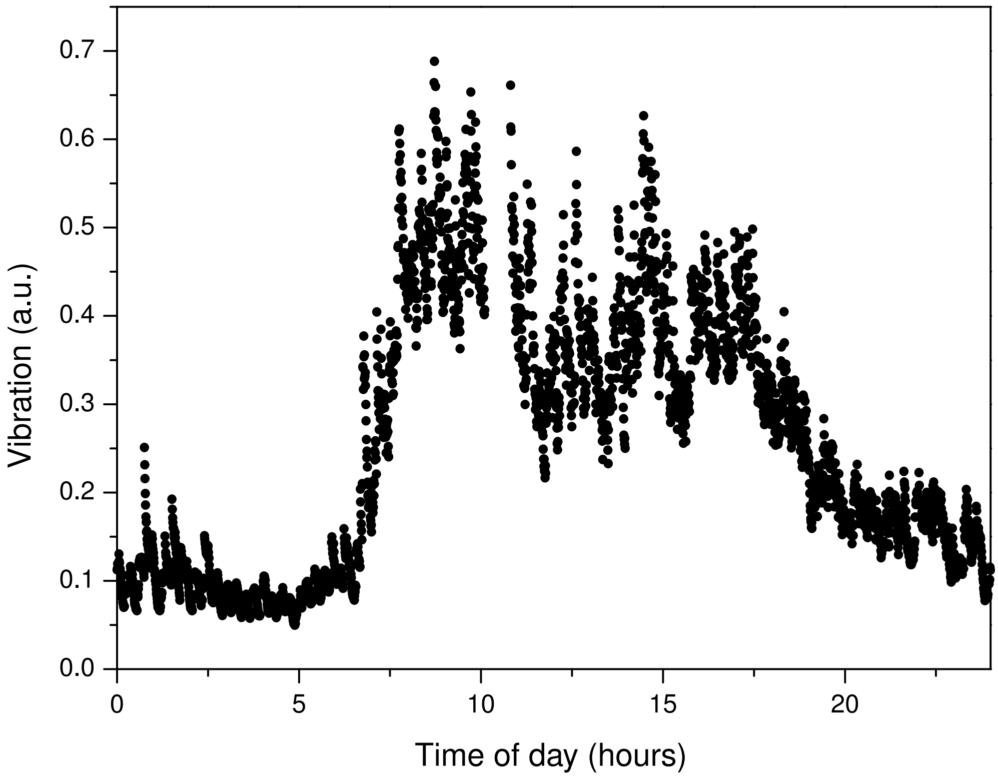

Figure 4.5: Level of vibration between 5 and 30 Hz over a 24 hour period.

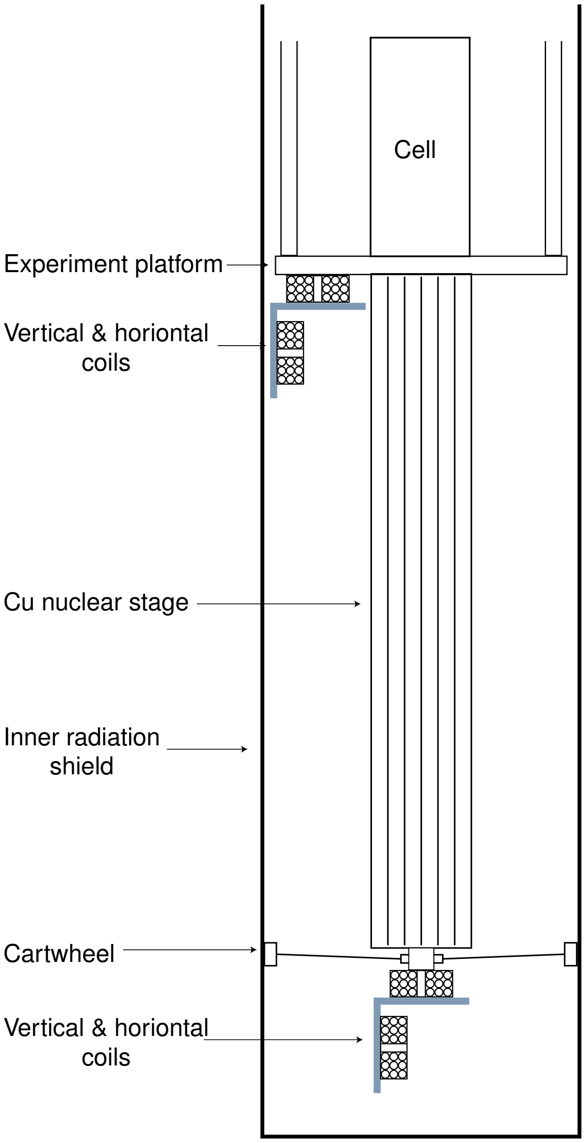
Cell
Experiment platform
Vertical & horiontal coils
Cu nuclear stage
Inner radiation shield
Cartwheel
Vertical & horiontal coils

Figure 4.6: Location of coils used to measure relative motion between the nuclear stage and magnet.

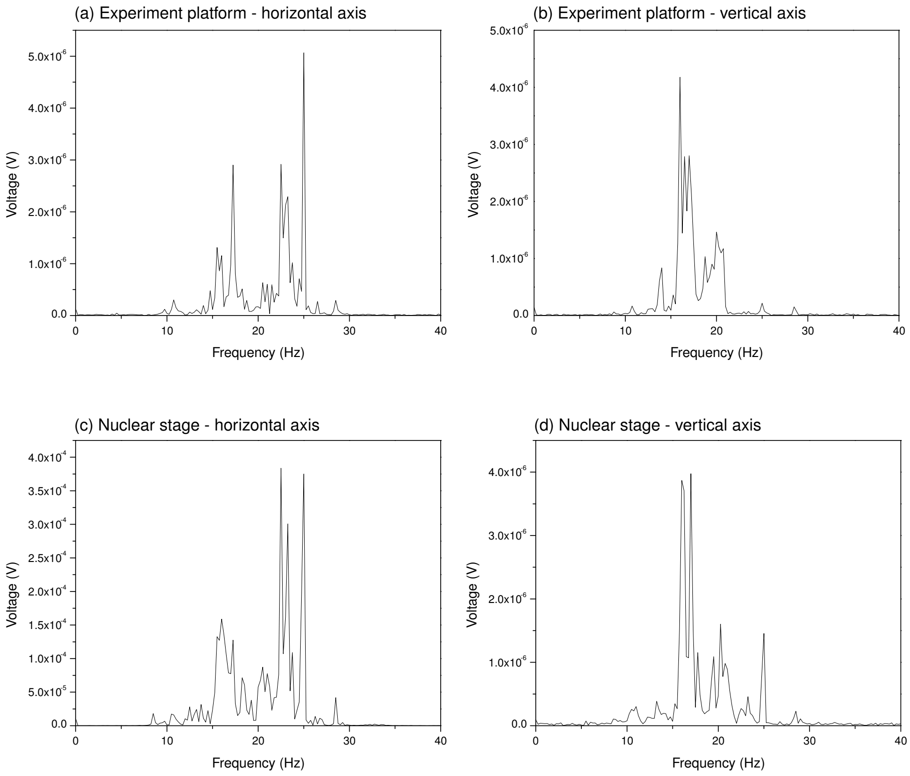

Figure 4.7: Example voltage spectra from each of the four search coils.

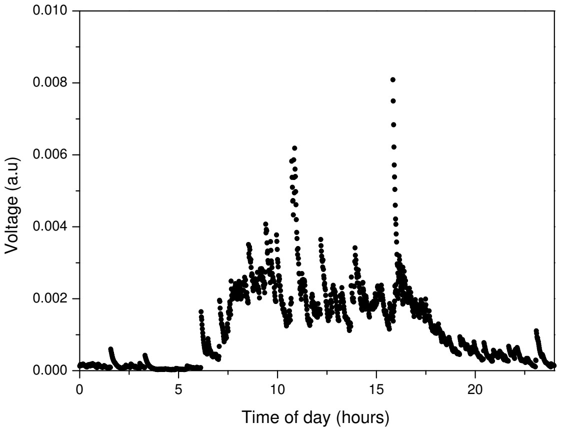

Figure 4.8: Variation of vibration for the horizontal coil on the bottom of the nuclear stage as a function of time of day.

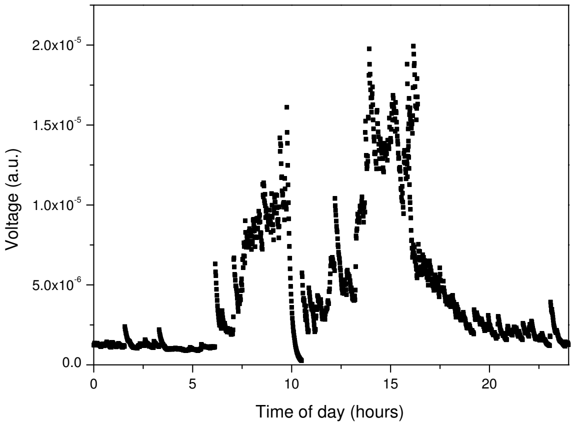

Figure 4.9: Variation of vibration for the horizontal coil on the experimental platform as a function of time of day.

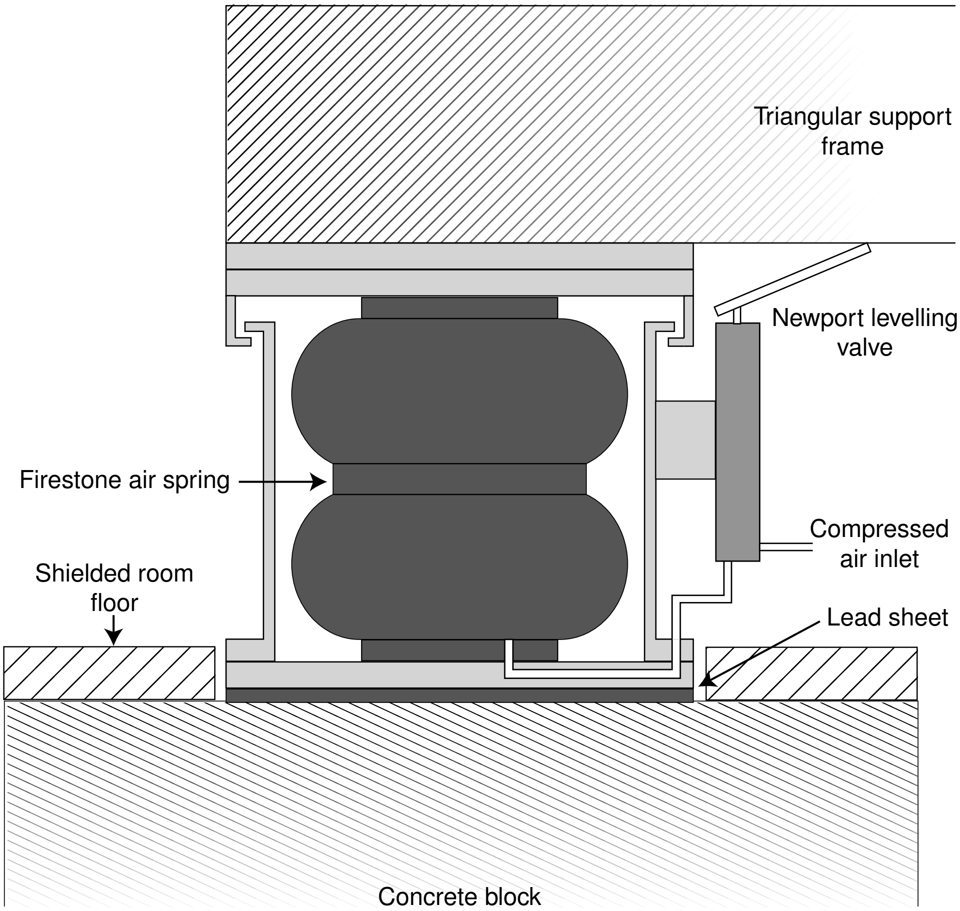
Triangular support frame
Newport levelling valve
Firestone air spring
Compressed air inlet
Shielded room floor
Lead sheet
Concrete block

Figure 4.10: Air spring assembly.

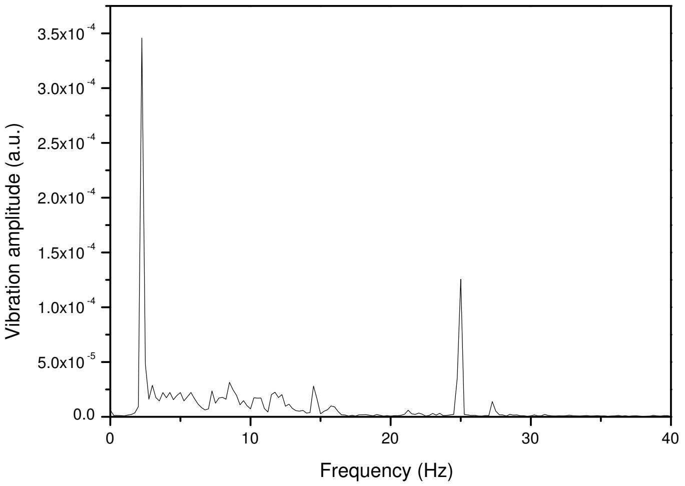

Figure 4.11: Vibration spectrum on the rotating platform with the air springs inflated. The corresponding spectrum before the air springs were installed is shown in figure 4.3a.

Chapter 5

Effect of rotation on texture formation

5.1 Introduction

In section 2.1 it was shown that uniform textures are needed in order to observe any quantitative effect due to orbital ferromagnetism. We have investigated the conditions needed to produce a uniform texture. The uniformity of the texture is characterized by the frequency shift obtained on sweeping magnetic field through the Fréedericksz field, H_F. A uniform texture shows a larger frequency shift than a non-uniform texture due to a greater change in superfluid density ($\rho_{s\perp} \rightarrow \rho_{s\|}$).

Section 5.2 outlines how the field sweeps were performed and analyzed and gives some examples for various textures. The effect of rotation whilst cooling through the superfluid transition is described in section 5.3 and possible explanations are then given in section 5.4.

5.2 Field sweeps

The method used for measuring the frequency and bandwidth of the torsional oscillator was described in section 3.6. Just before the start of a sweep the computer would estimate the present resonant frequency and change the drive frequency to this value, then the drive frequency and voltage were kept constant during the field sweep. The field sweep was then started after a short pause to allow the oscillator to adjust to the change in drive frequency. The coil current was provided by an Agilent 6628A DC precision current source. The current was typically ramped in 1 mA steps, although often with smaller steps close to H_F. A pause of duration 6 seconds normally followed each step and then the lock-in outputs were measured 60 times over the next six seconds and the average values were then used to calculate ν_R and ν_B using equations 3.16 - 3.18. The time constant of the lock-in was 3 seconds.

Figures 5.1 and 5.2 shows the response of the torsional oscillator for both directions of magnetic field. There is a clear asymmetry between the two. The Fréedericksz transition occurs at a different coil current. The difference in this example is 2.2 Gauss, far greater than the expected effect of orbital ferromagnetism. This is caused by a vertical component of magnetic field that became trapped inside the Nb shield when it became superconducting. It is for this reason that it is better to sweep field in the same direction and reverse the direction of $\mathbf{l}$ when trying to observe the effect of orbital ferromagnetism.

The magnitude of the trapped field was found to be greatest if the box that completes the shielded room was raised before cooling down the cryostat. It seems that the box has become slightly magnetized due to the main demagnetization solenoid being ramped up and down over a period of many years. The trapped field was therefore minimized to 0.8 Gauss by cooling down the cryostat (and hence cooling the Nb shield into the superconducting state) before raising the box. A magnetic shield made from a high permeability material known as mu-metal was

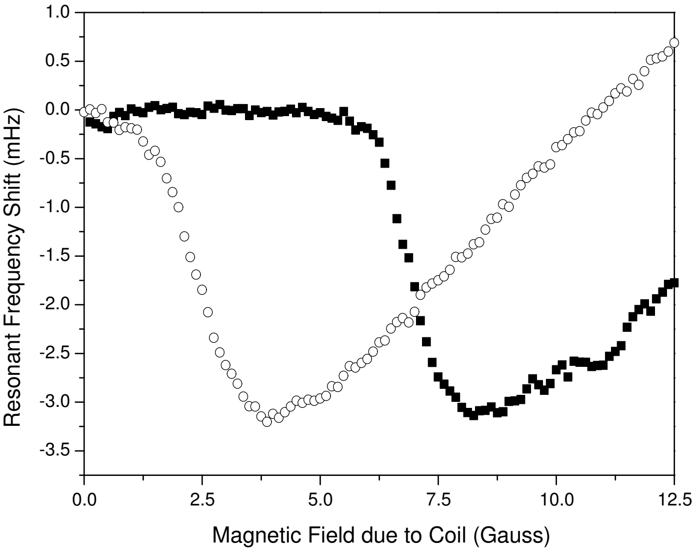

Figure 5.1: Resonant frequency shift for field swept in opposite directions. The difference is due to the presence of a 2.2 G trapped field.

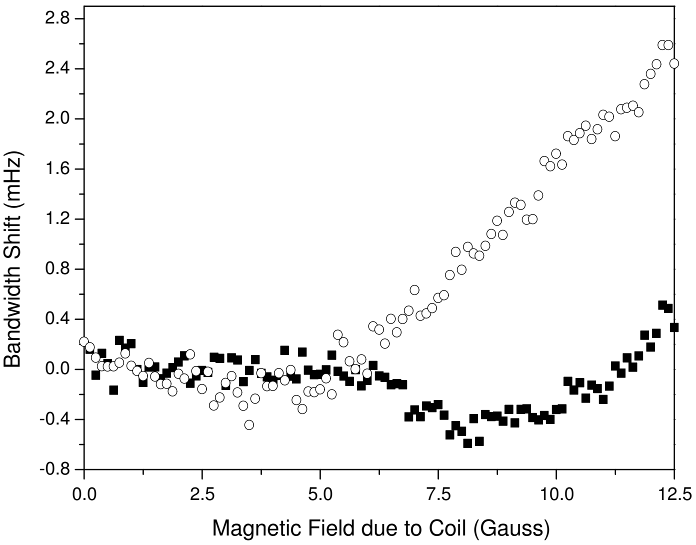

Figure 5.2: Shift in bandwidth for field swept in opposite directions.

added in later runs of the experiment to reduce the trapped field to such a low level that it could not be resolved between fields sweeps in opposite directions. In all the following measurements that are presented in this and later chapters either the trapped field has been measured and subtracted from the data or the data was taken after the installation of the mu-metal shield.

Figures 5.3 and 5.4 shows two example field sweeps at a temperature of $\sim 0.88T_c$. One is for a uniform **l**-texture prepared by cooling slowly through T_c whilst rotating the cryostat (more details are given in the following section) and the other for a highly non-uniform texture that was formed by warming from the B-phase into the A-phase, apparently causing a poly-domain sample with many regions of **l**-up and down. In this case there is no sharp Fréedericksz transition due to the presence of domain walls (see section 2.5.1) and the frequency shift is small due to small change in the average superfluid density. It has also been found that such a texture can support a persistent current due to vortices becoming pinned after rotation has been stopped. More details are given in chapter 7.

The field sweeps were all taken whilst the ^{3}He was slowly warming. The effect of temperature drift during the sweeps was removed by subtracting a straight line found by a least squares fit to data points taken at low field (before the texture distorts) of the sweep of interest and the following sweep. The frequency was then scaled such that the scaled frequency $\bar{\nu_R}$ was equal to one when $H < H_F$ and zero at the minimum frequency. It was found that the scaled frequency data around H_F was well represented by the following empirical function

$$\bar{\nu_R} = \left(1 + \mathrm{e}^{p_1(H-p_2)}\right)^{-0.5} \tag{5.1}$$

where p_1 and p_2 are fitting parameters. The Fréedericksz transition field is then found by extrapolating tangent to the curve. Figure 5.5 shows an example.

In theory the resonant frequency should have an infinite slope at the Fréedericksz transition for a uniform texture in an infinite slab (see chapter 2). In practice there are several factors which can cause the transition to become rounded. Firstly, a real

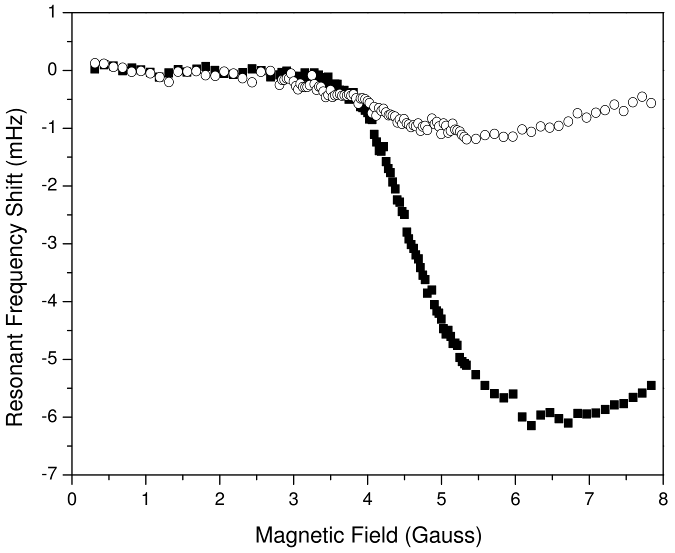

Figure 5.3: Resonant frequency shift for a uniform texture (closed square) and a non-uniform texture (open circle) created by warming from the B-phase.

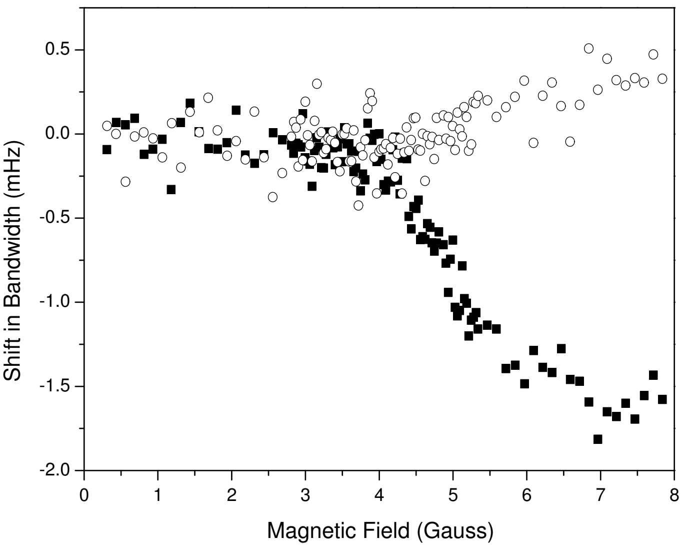

Figure 5.4: Shift in Bandwidth for uniform (closed square) and non-uniform textures (open circle).

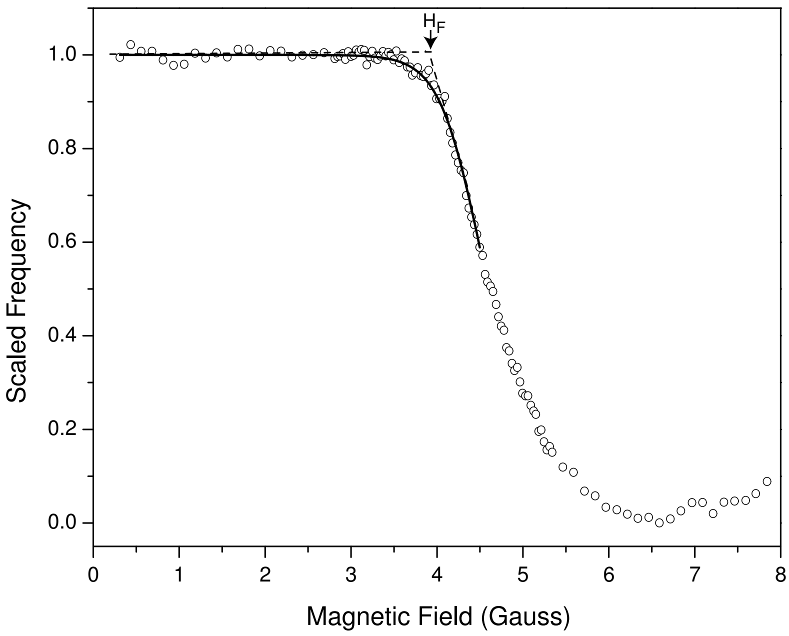

Figure 5.5: Scaled frequency as a function of magnetic field at 0.9 T_c. The solid line is a least squares fit using equation 5.1. The dashed lines show how the Fréedericksz transition field is estimated.

slab has a finite size and is bounded by a perimeter wall. The boundary condition that **l** must be perpendicular to the perimeter wall results in a region of distorted texture at the outer edge of the slab (see figure 6.6) which will increase in size when a magnetic field is applied (even for fields less than H_F). This will cause rounding of the Fréedericksz transition with the severity of the rounding depending on the aspect ratio ($2R/D$) of the slab [69]. In our case the aspect ratio of 40 means that the effect of the outer edge can be ignored. Further rounding of the transition can be caused if the slab upper and lower boundaries are not parallel (i.e. a position dependent slab thickness) then the transition would occur at different places in the slab at different magnetic fields since $H_F \propto 1/D$. This is unlikely though since the normal state measurements fit the hydrodynamic theory so well (see chapter 3). Another possibility is that the magnetic field is inhomogeneous over the volume of the slab but this again is unlikely since the coil was carefully designed to provide a homogeneous field. The most likely cause of rounding in this case is probably due to the direction of magnetic field being at a slight angle to the normal to the slab boundaries. The design of the experiment would probably have to be changed in order to rectify this.

5.3 Effect of rotation

Rotating the cryostat during slow cooling into superfluid state is expected to produce an array of vortices with the lowest free energy. It was shown in section 2.5.2 that in our geometry continuous (Anderson-Toulouse (AT)) vortices should be produced in preference to singular vortices when angular velocities greater than 0.066 rad/s are used. A previous experiment in Manchester [27], which also used a slab geometry with a slab thickness of 0.1 mm, showed that cooling into the superfluid state while rotating could produce a uniform texture. It is thought that this is due to the effect of the AT vortices since they favour being embedded in a texture of a particular direction. Rotation in the opposite direction to that used during cooling through the transition leads to either vortices of higher energy being created or the direction of the texture has to be reversed. It is likely that both processes occur and enough bursts of rotation eventually leads to a uniform texture of the opposite orientation to the original one. It is this ability to obtain and reverse uniform **l**-textures that led us to believe we might be able to detect the expected effect of orbital ferromagnetism by first measuring H_F for one direction of **l** then reversing the texture and again measuring H_F to look for small difference that the orbital ferromagnetism is expected to cause (see chapter 2).

The effect of varying the angular velocity during cooling through T_c has been investigated. The textural sample was prepared by starting rotation whilst in the normal state. The liquid was then cooled slowly (typically with a cooling rate of a few μK/min) into the superfluid state. Rotation was continued until the sample had cooled well below T_c and the cryostat was then stopped. The uniformity of the texture was then probed by sweeping the magnetic field and observing the maximum shift in resonant frequency ($\Delta\nu_{RM}$). Such measurement were done for zero applied field ($H = 0$) and in the small field ($H = 2.2\,\mathrm{G}$) that was trapped by the Nb shield. Any field applied in the vertical direction is likely to cause non-uniformity in the texture since it favours **d** (and hence **l**) to be parallel to the slab boundaries. Some people in the past have tried to improve the uniformity of the texture by applying a field of several hundred Gauss parallel to the boundaries [56] but they found this made little or no difference.

Figure 5.6 shows the maximum shift in resonant frequency $\Delta\nu_{RM}$ as a function of temperature for various rotation velocities that were used during cooling into the superfluid state in a vertical field of 2.2 G. $\Delta\nu_{RM}$ for a texture created by warming from the B-phase into the A-phase is also shown for comparison. This is found to create a highly non-uniform texture. The variation of $\Delta\nu_{RM}$ as a function of the preparation angular velocity for textures prepared with zero and non-zero magnetic field is shown in figure 5.6. For the zero field case, varying the angular velocity seemed to make little or no difference to the quality of the texture. There is scatter of around ±0.5mHz in the data as shown from the several samples prepared with $\Omega = 0.42$ rad/s. If several further short (e.g. a few minutes) bursts of rotation in the same direction as that used whilst cooling, and with high acceleration and deceleration (~ 0.04 rad/s^2), were applied then the texture could be improved slightly but not below the lower dashed line shown on the figure. Then any further rotations did not change $\Delta\nu_{RM}$ so this was interpreted as being the uniform texture. However, the application of a small field ($\sim 0.5H_F$) creates a minimum in $\Delta\nu_{RM}$ at Ω ~0.42 rad/s which is the uniform texture. Cooling at other angular velocities produces non-uniform textures but they can also be improved by a further burst of rotation in the original direction.

No detailed model has yet been found to explain this behaviour, but there are several speculations that we can make. It is possible that a different type of vortex, one that does not help to orientate the texture, is nucleated when a small field is applied such as the singular phase vortex described in chapters 1 and 2. This seems unlikely as it would contradict the calculated phase diagram shown in figure 2.14 which shows that singular vortices are less likely to occur at non-zero fields, but the observed effect could be due to vortices with structures more complicated than the radial AT vortex which was used to simplify calculations. It could also be due to the way in which AT vortices interact with each other and the surrounding bulk texture. The distance between the vortex centers for double-quantum vortices is

$$d \simeq \left(\frac{h}{2m_s\Omega}\right)^{1/2} \tag{5.2}$$

so the distance between vortices decreases as Ω increases. The calculations in chapter 2 show that the radial extent of the soft core of the vortices is comparable to the slab thickness, so that low angular velocities correspond to the regime where the cores are weakly interacting ($d >> D$) and high angular velocities lead to strongly interacting cores ($d < 2D$). In the weakly interacting case, the vortices may have little influence on the bulk **l**-texture surrounding them and so will not improve the quality of the textures compared to those prepared without rotation.

One might expect that the vortices will have a strong stabilizing influence on the surrounding texture for the case when the cores are almost overlapping ($d \geq D$). Then at angular higher velocities the texture is distorted by overlapping cores or perhaps an array of single quantum continuous vortices (such as Mermin-Ho) form, leaving behind a non-uniform texture when rotation is stopped.

Clearly further measurements and more theoretical calculations of possible vortex arrays and their free-energies are needed to clarify the situation. The zero-field measurements need to be extended to $\Omega > 0.46$ rad/s in order to see if the quality of the texture deteriorates in the same way that the non-zero field measurements do. Measurements at other fields would also help, such as determining if the minimum in $\Delta\nu_{RM}$ is dependent on the applied field. This should be the case if the reason for the minimum is due to near-overlapping of the vortex soft cores since applying a field perpendicular to the slab leads to the soft core size increasing, resulting in overlapping occurring at lower Ω. Similarly, a field applied parallel to the slab would reduce the size of the soft cores and hence increase the value of Ω at which the cores should overlap. So although these preliminary measurements cannot be fully explained they do show that such studies have the potential to help understand some of the dynamics of vortices in a slab.

5.4 Measurement of H_F

The measured values of $H_F D$ for both uniform and non-uniform textures that were prepared in a magnetic field of 2.2 G are shown in figure 5.8. The uniform textures are those prepared with $\Omega = 0.42$ rad/s and the non-uniform textures are those prepared with other values of Ω. The solid line shows the theoretical calculation, given by equation 2.11:

$$H_F D = \pi \left(\frac{K_b'}{\Delta\chi} \right)^{1/2} .$$

At temperatures below T_c the quantity $H_F D$ depends on the Fermi liquid parameters F_1^s,F_0^a and F_1^a as well as strong coupling corrections to the A-phase energy

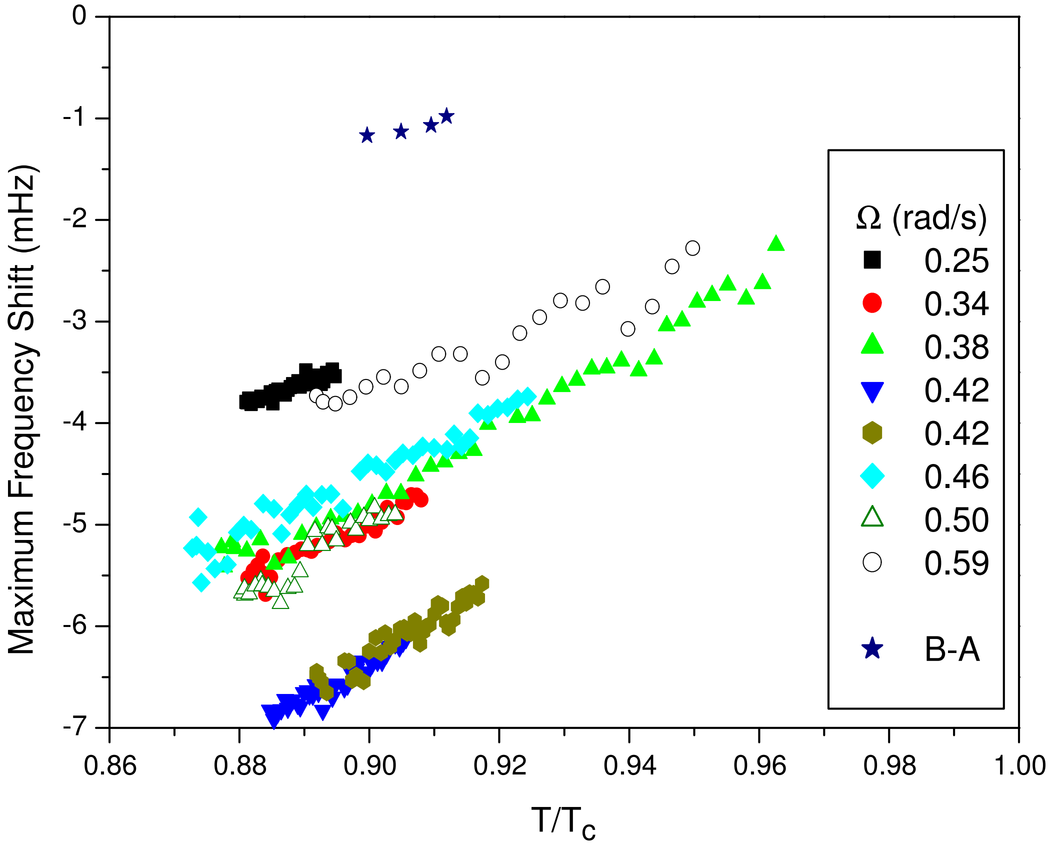

Figure 5.6: Maximum frequency shift for textures prepared with different rotation velocities during cooling through T_c in a magnetic field of 2.2 Gauss. The shifts observed for textures formed by warming from the B-phase are shown for comparison.

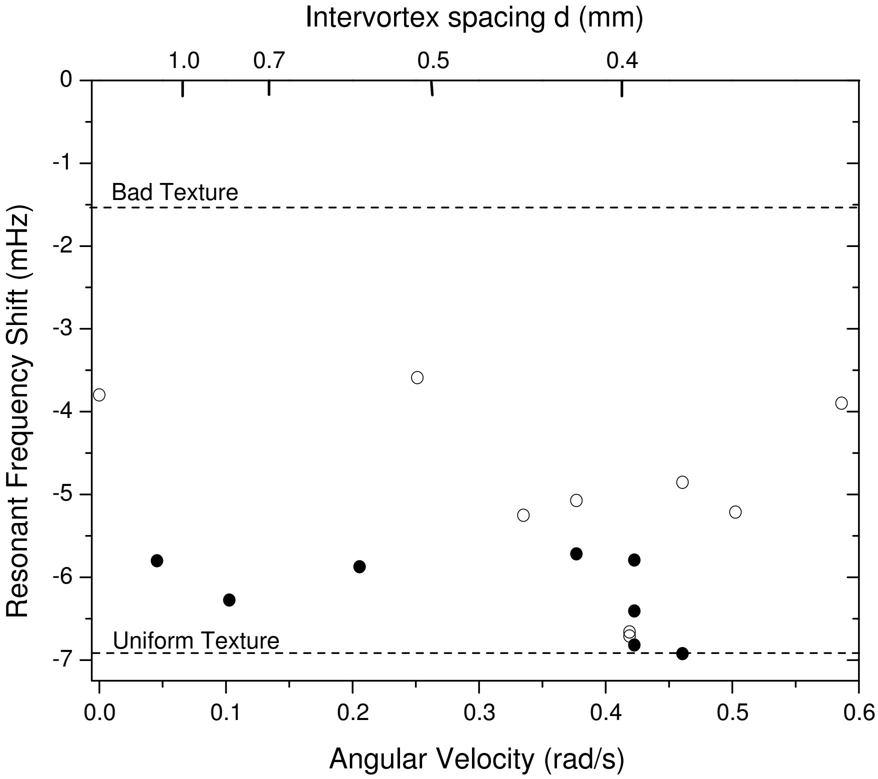

Figure 5.7: Maximum shift in resonant frequency at $T = 0.89T_c$ as a function of angular velocity during cooling through T_c. The open and closed circles are for textures prepared in a vertical field of 2.2G and zero field respectively. The upper dashed line denotes textures prepared by warming from the B phase and the lower line shows the lowest observed, which is thought to correspond to a uniform texture. The upper horizontal axis shows the intervortex spacing.

gap. The numerical evaluation of the susceptibility anisotropy, $\Delta\chi$, and the bending energy, K_b' is detailed in appendix C of [45]. In the present case, the BCS energy gap was used without any strong coupling energy corrections.

The measurements are below the theoretical curve but are in excellent agreement with the measurements of Hook *et al.* [18] (described in section 1.4.2). The uniform texture typically has higher values of H_F compared to the non-uniform textures, which is what would be expected since defects in the texture (such as the domain walls considered in chapter 2) provide a seed from which the distorted texture can grow. There is also less scatter in the measurements for the uniform texture. The spread in values for uniform textures is around 5% whereas it is almost 20% for the other textures, similar to the 15% spread observed by Hook and coworkers. The high spread is again likely to be due to the presence of defects of varying number and perhaps of different types. It is shown in chapter 7 that the presence of defects in the texture can lead to a persistent superflow remaining after rotation has been stopped, which reduces H_F because the superflow helps to distort the $\mathbf{l}$ texture.

The expected effect of orbital ferromagnetism, calculated in section 2.4, is to cause shifts in H_F of $\sim 0.1\%$ H_F between the zero field states that have $\mathbf{l}$ parallel and antiparallel to the field direction. No shifts in H_F have yet been observed in this experiment that can be attributed to the orbital ferromagnetism. Repeated field sweeps for a particular sample give values of H_F that have a scatter of $\sim$ 1%. The scatter is least when the heat leak into the superfluid is lowest indicating that thermal currents in the superfluid may be responsible for some of the scatter. As discussed above there is $\sim$ 5% scatter in the measurements of H_F for several samples of uniform textures. There is certainly no systematic shift between textures prepared with opposite senses of rotation (which it is thought leads to uniform textures with $\mathbf{l}$ up and down). This may indicate that, although the uniformity of the textures prepared whilst rotating during cooling is better in comparison to those produced without rotation, there may still be some defects present which can cause rounding of the transition and can also trap a small number of vortices

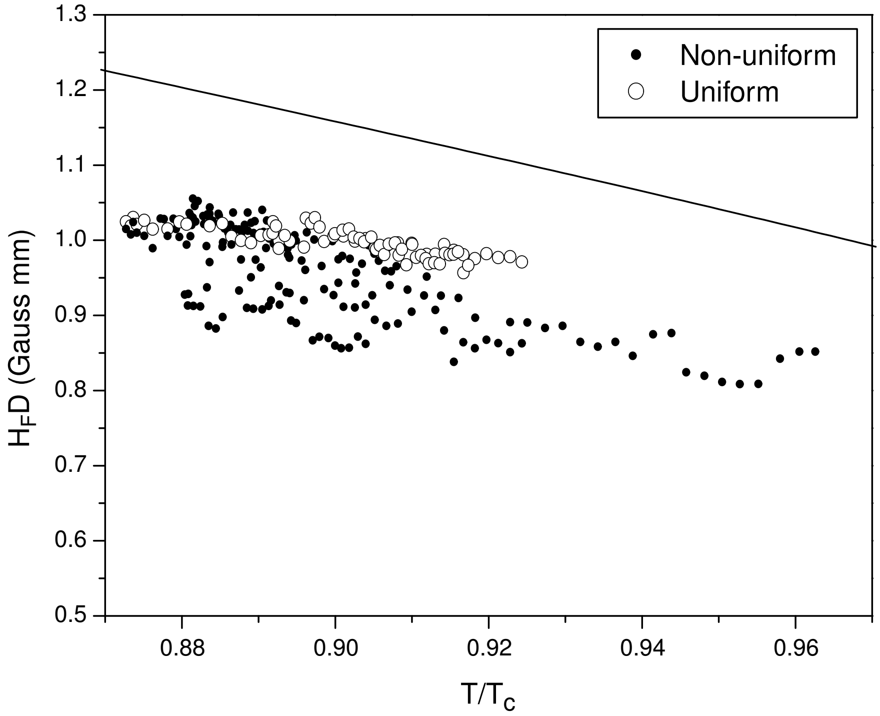

Figure 5.8: Measured values for H_FD for both uniform (empty circles) and non-uniform textures (solid circles) prepared in a magnetic field of 2.2 G. The solid line is a theoretical calculation described in the text. The uniform texture measurements are combined from three samples prepared whilst cooling into the A-phase at 0.42 rad/s and the non-uniform texture measurements are a compilation of six samples prepared by cooling with other angular velocities.

after rotation is stopped. Assuming that we have been able to obtain uniform textures, where the orbital magnetic moment of each Cooper pair is aligned in the same direction, then we can place an upper limit on the orbital magnetic moment of $10^{-10}\mu_B$ per atom. This is still an order of magnitude greater predicted value [21]. It seems that the best way to try and measure the orbital ferromagnetism would be to use much higher magnetic fields. It was shown in section 2.4.2 that at very high fields ($\sim$ 10 T) the ferromagnetic energy term dominates the dipolar term such that a uniform **l** texture is restored along with a uniform **d** texture that is perpendicular to **l**. Such an experiment may be possible using multi domain samples (in which case a rotating cryostat would not be needed) since domains with **l** antiparallel to **H** should grow at the expense of domains with **l** oriented in the opposite direction.

Chapter 6

Rotation while superfluid: uniform textures

6.1 Introduction

Some of the effects of rotating the cryostat while cooling into the A-phase were discussed in the last chapter where the vortex structures with the lowest free-energy should be formed. This chapter is concerned with the effects of starting and stopping rotation while already in the superfluid state. In this case the vortices that are formed are those with the lowest critical velocity, even if they do not have the lowest free-energy. The critical velocity for continuous vortices is lower than for singular vortices due to the much larger vortex core. Experiments in Helsinki have shown that singular vortices, as well as several other vortex structures, can be formed by rotation while cooling into the superfluid state [70, 71] but that rotation of the superfluid creates either double-quantum continuous vortices [72] or continuous vortex sheets [73] depending on how the cryostat is rotated (e.g. in the Helsinki experiments oscillatory rotation with high frequencies produces vortex sheets).

There are several reasons why continuous vortices in superfluid ^{3}He-A form a more ideal system that vortices in superfluid ^{4}He . The main reason is that the vortex core radii are much larger in ^{3}He making vortex free states possible since the vortices are less likely to be pinned by imperfections on the container walls. Also, vortex nucleation is an intrinsic process for ^{3}He whereas in superfluid ^{4}He it is generally an extrinsic process. In ^{3}He-A the boundary condition forces the $\mathbf{l}$ texture to be perpendicular to the container walls so that vortices are formed, due to an instability in the texture, at least a textural bending length ($\sim 10\,\mu$m) away from the walls.

The observed response of the torsional oscillator when the experiment is accelerated and decelerated is detailed in section 6.2 and a theoretical model of this behaviour is described in section 6.3. Measured values of the vortex critical velocity for uniform textures are presented in sections 6.4 and section 6.5 describes the a preliminary study of what happens when the cryostat is rotated in different directions. The effect of rotation upon non-uniform textures is described in the following chapter.

6.2 Acceleration and deceleration of a superfluid

When a superfluid initially at rest with respect to its container (with radius R) is then slowly rotated with angular velocity, Ω, the superfluid component will remain stationary ($v_s = 0$) and the normal fluid component will undergo solid body rotation ($v_n = r\Omega$), so a counterflow is generated over the whole container (figure 6.1a) . Further acceleration leads to the counterflow increasing until the critical velocity for vortex nucleation, v_c, is reached at the edge of the container. At this point a vortex will be formed at the edge of the container and this will then migrate towards the center due to the Magnus force acting on the vortex line (figure 6.1b) and the counterflow velocity at the edge of the slab simultaneously drops below v_c. Increasing Ω leads to a new vortex being nucleated each time

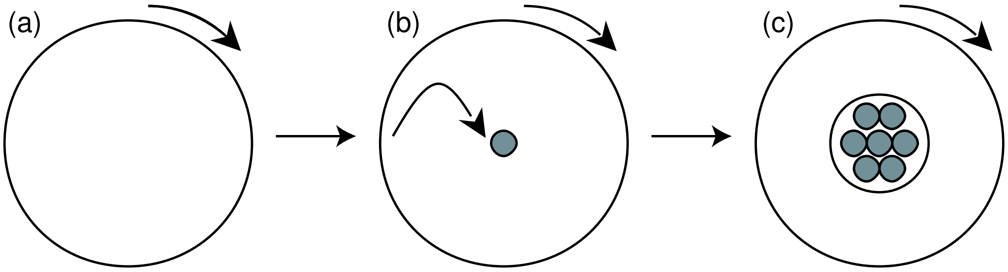

Figure 6.1: Accelerating superfluid (a) counterflow (b) vortex nucleation and (c) vortex cluster surrounded by a vortex free counterflow region.

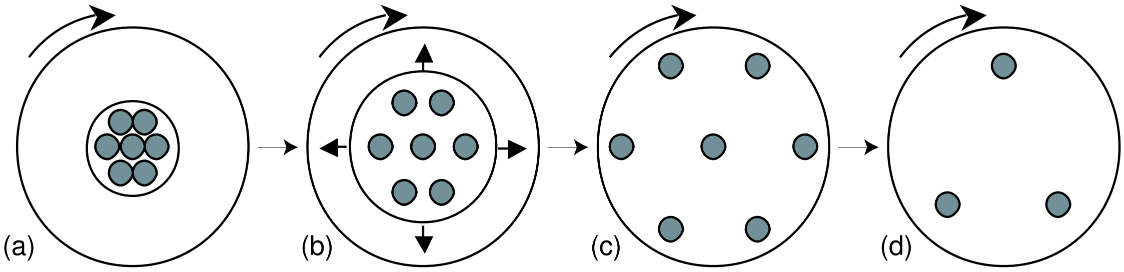

Figure 6.2: Decelerating superfluid (b) vortex cluster expands with a constant number of vortices, the counterflow region shrinks (c) the vortex cluster fills the whole container with no counterflow region (d) further deceleration results in vortices annihilating at the container walls.

the counterflow velocity at the edge of the container exceeds v_c so that a cluster of vortices form in the central region of the container surrounded by a vortex-free counterflow region near to the container walls (figure 6.1c). The radius of the vortex cluster in the continuum approximation, where the number of vortices $N_v \gg 1$, is

$$R_c = R_{eff}\sqrt{1 - \frac{\Omega_c}{\Omega}} \tag{6.1}$$

where R_{eff} and $\Omega_c = R_{eff}v_c$ is the radius and angular velocity at which the nucleation of the first vortex occur. The number density of vortices in the cluster is

$$n_v = \frac{2\Omega}{\kappa} \tag{6.2}$$

where κ is the circulation of each vortex ($\kappa = 2\kappa_0$ for double-quantum vortices). The motion of the vortices mimic solid body rotation so that counterflow inside the cluster is minimized ($\bar{v}_s \approx v_n$). The superfluid velocity outside the cluster is inversely proportional to radius. Thus the critical counterflow at R_{eff} is

$$v_n(R_{eff}) - v_s(R_{eff}) = \Omega R_{eff} - \frac{N_v\kappa}{2\pi R_{eff}} = v_c \tag{6.3}$$

where N_v is the number of vortices present,

$$N_v = \frac{2\pi R_{eff}^2}{\kappa}(\Omega - \Omega_c). \tag{6.4}$$

If Ω is now decreased from the maximum angular velocity reached, Ω_{max}, then the vortex array will start to expand with the number of vortices constant and the counterflow region will shrink (figure 6.2b). The radius of the cluster is then given by

$$R_c = R_{eff}\sqrt{\frac{1}{\Omega}\left(\Omega_{max} - \Omega_c\right)}. \tag{6.5}$$

Eventually the vortex cluster will fill the whole container ($R_c = R$), with no counterflow region (figure 6.2c), when the angular velocity reaches

$$\Omega_0 = \Omega_c + \frac{R_{eff}^2}{R^2}\left(\Omega_{max} - \Omega_c\right). \tag{6.6}$$

Further deceleration then leads to vortices annihilating at the container walls (figure 6.2d) with the density of vortices given by equation 6.2. Eventually all the vortices will have been annihilated unless there is some mechanism that pins some of the vortices, preventing them from annihilating, and leading to a metastable persistent superflow after rotation has been stopped.

6.3 Rotation sweeps

We now turn to examine the behaviour of ^{3}He-A in a slab when it is rotated. The sweeps of angular velocity were carried out using a similar procedure to the magnetic field sweeps (described in section 5.2). The rotation was changed in steps with a pause in between each step to allow the texture and vortices to settle. The pause allowed depended upon the increment in angular velocity and varied between 30 to 300 seconds. The resonant frequency and bandwidth of the oscillator were measured several times after the pause and the average value of these measurements was used. Then the angular velocity was changed and the procedure was repeated.

A typical plot of the behaviour of resonant frequency and bandwidth observed during a sweep of angular velocity is shown in figures 6.3 and 6.4. The cryostat was rotated from stationary to 0.42 rad/s and then back to stationary. At low angular velocities there is no change in frequency and bandwidth, until a critical value of angular velocity is reached and then there is a sharp transition both in the resonant frequency and in the bandwidth. This is because the counterflow at the edge of the slab reaches the Fréedericksz threshold velocity, v_F, and the texture in that region becomes distorted. Further increases of angular velocity then results in more texture becoming distorted. Eventually the critical velocity for vortex nucleation, v_c, is reached, leading to a vortex cluster in the center of the slab that increases in size with increasing angular velocity. The vortices are embedded in a region of uniform texture that extends slightly outside the cluster resulting in the resonant frequency increasing. The counterflow belt then consists of a narrow region of uniform texture and an outer region of distorted texture separated by the radius R_{UT} at which the counterflow is

$$v_n(R_{UT}) - v_s(R_{UT}) = v_F. \tag{6.7}$$

Deceleration then causes the vortex cluster to expand and the region of distorted texture shrinks, causing the resonant frequency to increase, until eventually the vortex cluster fills the whole slab and the resonant frequency returns to the starting value when $R_{UT} = R$. Further deceleration then leads to vortices annihilating at the outside walls of the slab. Both the frequency and bandwidth return to their original values when rotation has stopped.

There are thus five distinct regimes observed during the rotation sweeps. The first three occur during acceleration and the other two during subsequent deceleration. They are each described in order below:

1) When $\Omega < v_F/R$, there is a uniform texture throughout the whole slab ($R_{UT} = R$) and hence there will be no shift in the resonant frequency.

2) When $v_F/R \leq \Omega < \Omega_c$, the radius of the uniform texture is $R_{UT} = v_F/\Omega$ and the texture is distorted by the flow everywhere outside this radius. The amount of distortion is greatest near to the perimeter of the slab where the counterflow velocity is greatest.

3) When $\Omega_c \leq \Omega \leq \Omega_{max}$, there is a vortex cluster in the center of the slab with a radius given by equation 6.1 and the number of vortices is given by equation 6.4. The texture will be distorted when the counterflow exceeds the Fréedericksz velocity, so the radius of the region with uniform texture is found from

$$v_F = \Omega R_{UT} - \frac{R_{eff}^2}{R_{UT}} (\Omega - \Omega_c) \tag{6.8}$$

which has the solution

$$R_{UT} = \frac{1}{2\Omega} \left(v_F + \sqrt{v_F^2 + 4\Omega R_{eff}^2 (\Omega - \Omega_c)} \right). \tag{6.9}$$

4) When $\Omega_A = v_F R + R_{eff}^2 R^2 (\Omega_{max} - \Omega_c) \leq \Omega \leq \Omega_{max}$ during deceleration the vortex cluster expands with a constant number of vortices. The radius of the

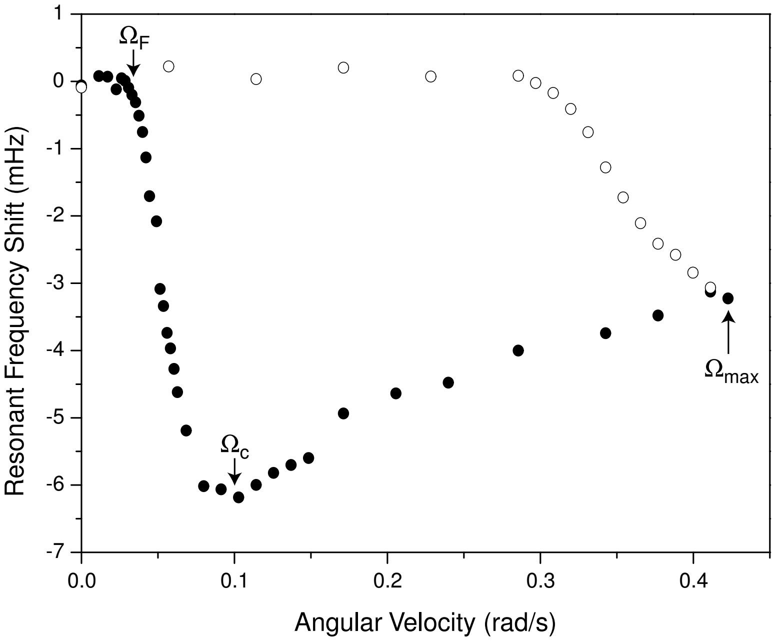

Figure 6.3: Resonant frequency of torsional oscillator during a sweep of rotation. The solid and open circles represent acceleration and deceleration respectively.

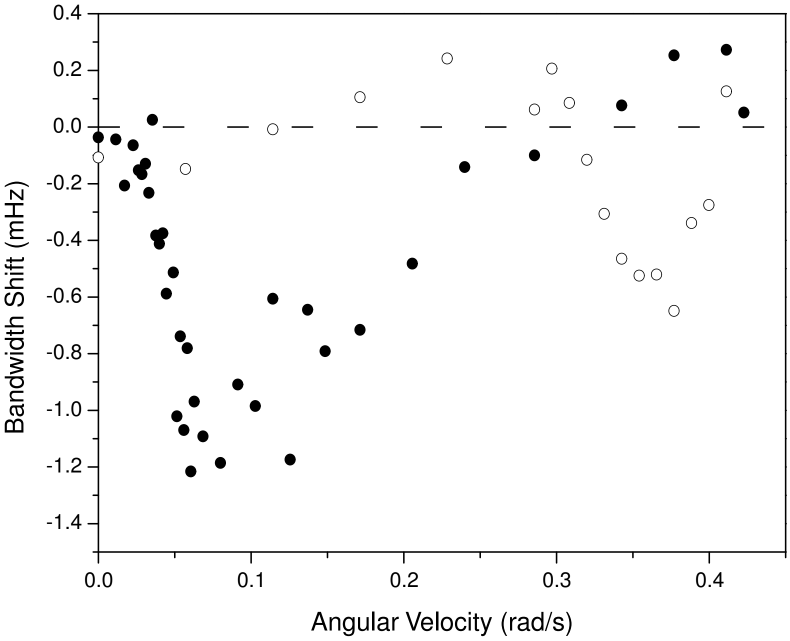

Figure 6.4: Bandwidth of torsional oscillator during a sweep of rotation. The solid and open circles represent acceleration and deceleration respectively.

uniform texture is then similar to the previous equation,

$$R_{UT} = \frac{1}{2\Omega}\left((v_F + \sqrt{v_F^2 + 4\Omega R_{eff}^2\left(\Omega_{max} - \Omega_c\right)}\right). \tag{6.10}$$

5) When $\Omega <= \Omega_A$ during deceleration the counterflow belt will only consist of uniform texture since the counterflow velocity has been reduced below the Fréedericksz velocity and so $R_{UT} = 1$.

Figure 6.5 combines the above five regimes, showing how R_{UT}/R varies as a function of angular velocity for a complete cycle of rotation between 0 and 0.5 rad/s.

The simplest way to convert R_{UT} into the torsional oscillator frequency shift is to assume that the distorted texture is purely azimuthal. This is a good approximation apart from the small region just outside R_{UT} where the texture is only slightly distorted and the region close to the slab boundaries where **l** is forced to be perpendicular to the walls. The frequency shift is given by

$$\Delta\nu_R = \Delta\nu_{Raz}\left(\left(\frac{R_{UT}}{R}\right)^4 - 1\right) \tag{6.11}$$

where the power of four allows for the fact that the frequency shift is greatest for fluid nearer to the outer perimeter of the slab since the contribution to the moment of inertia is proportional to R^4 and $\Delta\nu_{Raz}$ is a scaling factor that is adjusted to fit the experimental data.

Equation 6.11 and the simple model for R_{UT} were used to perform least squares fits to the experimentally observed frequency shifts during sweeps of rotation. Initially, R_{eff}, v_F, Ω_c and $\Delta\nu_{Raz}$ were all used as fitting parameters. It was found that R_{eff} appeared to be constant for all temperatures below $0.98T_c$ with an average value of $R_{eff} = 4.72 \pm 0.01$ mm (compared to the slab radius, $R = 5$ mm), giving the distance from the side walls where the vortices are created as $R - R_{eff} = 0.28$ mm. This is comparable to the slab thickness of 0.26 mm which is not surprising since the texture within one slab thickness from the slab perimeter is expected to be distorted and additionally constrained by the presence of another

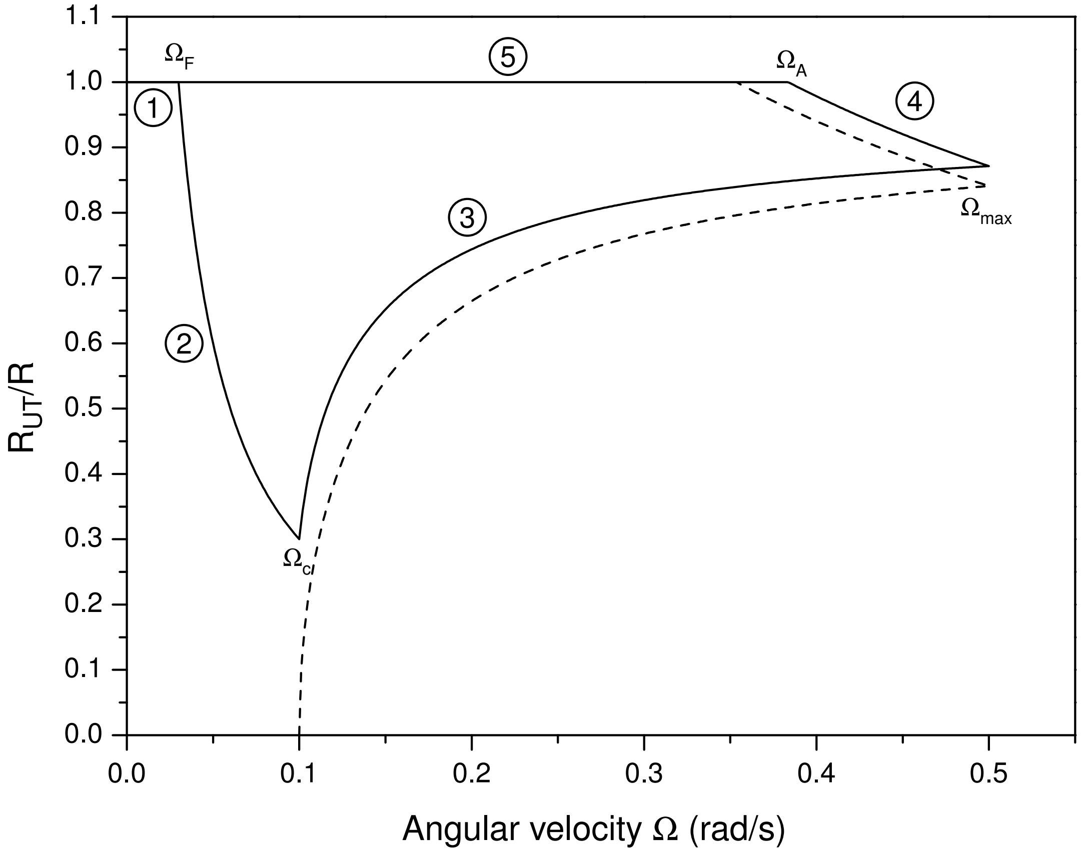

Figure 6.5: Radius of uniform texture region as a fraction of the radius of the slab as a function of angular velocity. The number on each region correspond to the regimes described in the text. The dashed line shows the radius of the vortex cluster.

boundary. A numerical simulation of the texture in close to the side walls is shown in figure 6.6 (similar to the calculations of Maki [49]). Figures 6.7 to 6.10 show the frequency shift for four rotation sweeps that were performed at approximately the same temperature but with different values of Ω_{max} and figures 6.11 to 6.14 show the frequency shifts for several rotation sweeps with the same value of Ω_{max} but at different temperatures. The solid lines are least squares fits using the model described above and three adjustable parameters (v_F, Ω_c and $\Delta\nu_{Raz}$). The overall quality of the fits is good considering the simplifying assumptions that are used in the model. There is rounding of the textural Fréedericksz flow transition, which is not accounted for in the model, due to the region of distorted texture at the outer perimeter where the texture will change even for angular velocities less than Ω_F. There is also some disagreement between the data and the model fits at angular velocities where there is a clear change in behaviour, such as at Ω_c. This is not surprising since the model is based upon extreme limits where there are either no vortices or very many vortices and so it is unlikely that the model will give a good description of the system at angular velocities that are in between these two regimes. The values of $\Delta\nu_{Raz}$ found from the fits are plotted against temperature in figure 6.15. Comparison with figure 5.6 shows that the frequency shifts caused by applying field and rotation are similar. The changes in the dimensionless parameter F_1 (see chapter 3) are of the right order of magnitude when compared to the expected responses of the torsional oscillator shown in figure 3.10.

6.4 Vortex critical velocity

The critical velocity for nucleation of double-quantum continuous vortices in ^{3}He-A has been extensively studied by the Helsinki group using NMR [74]. They used three different cylindrical sample containers with varying degrees of surface roughness. No systematic correlation between v_c and the roughness of the container used

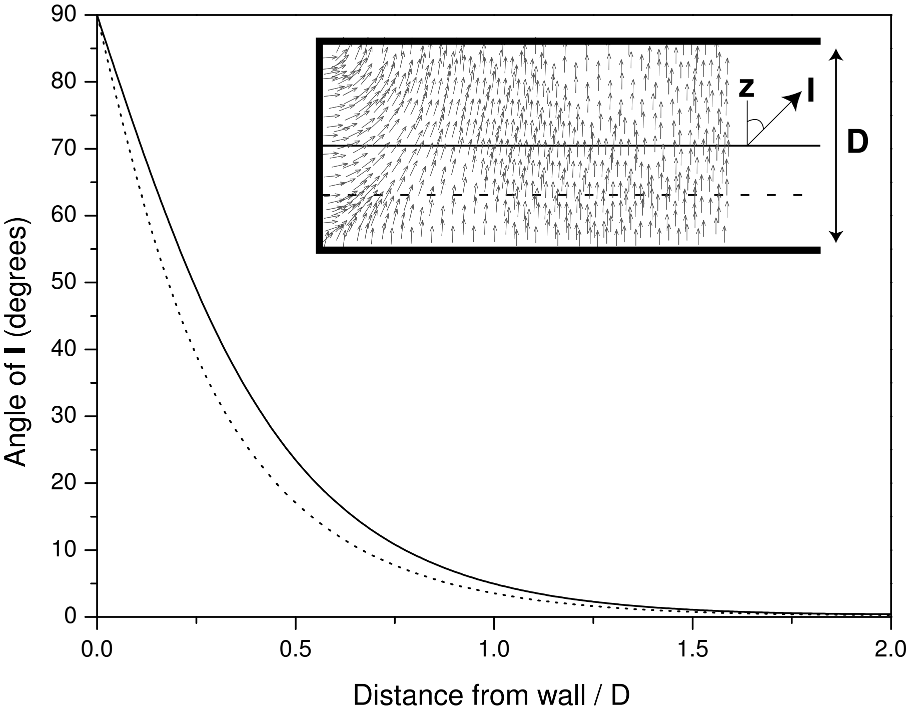

Figure 6.6: Numerical simulation of the angle between $\mathbf{l}$ and $\hat{\mathbf{z}}$ at $z = 0$ (solid line) and at $z = -D/4$ (dotted line) as a function of the distance from the side wall for a dipole-locked texture in zero field and no flow.

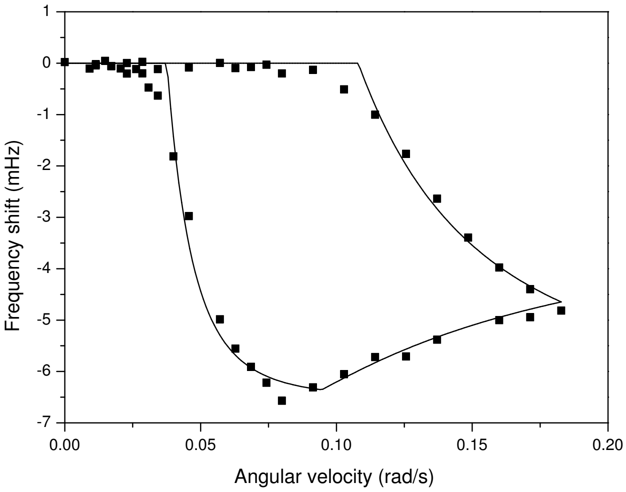

Figure 6.7: Rotation sweep with $\Omega_{max} = 0.183$ rad/s and $T = 0.91T_c$. The solid curve is a least squares fit using the model described in the text.

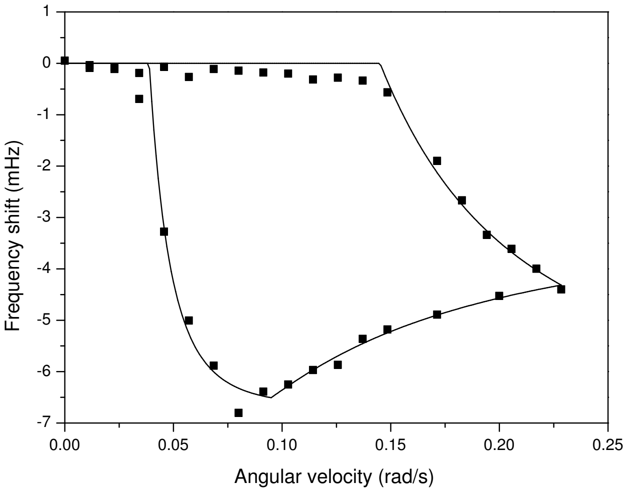

Figure 6.8: Rotation sweep with $\Omega_{max} = 0.228$ rad/s and $T = 0.92T_c$.

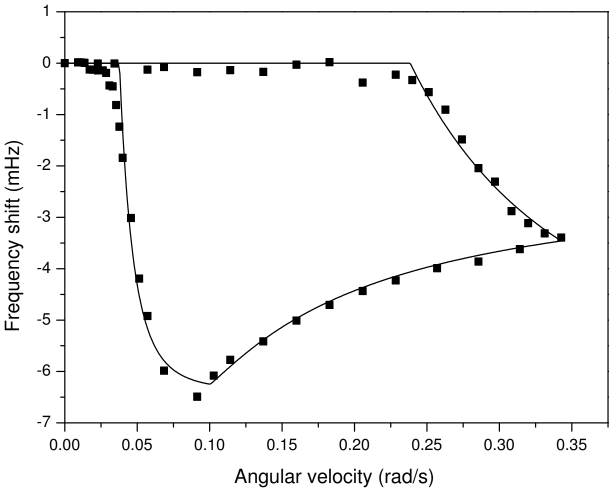

Figure 6.9: Rotation sweep with $\Omega_{max} = 0.343$ rad/s and $T = 0.92T_c$.

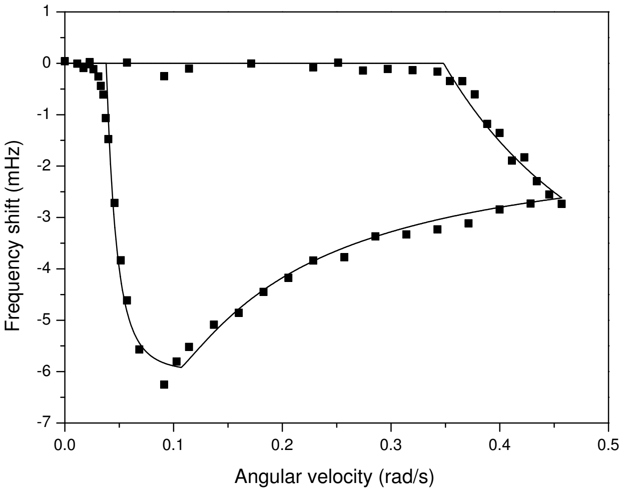

Figure 6.10: Rotation sweep with $\Omega_{max} = 0.457$ rad/s and $T = 0.92T_c$.

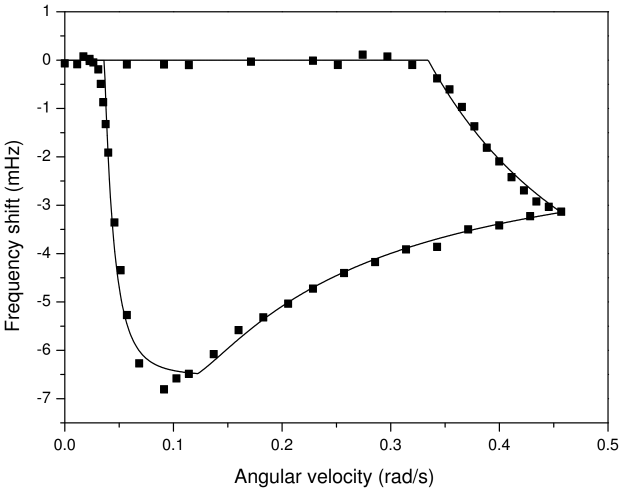

Figure 6.11: Rotation sweep with $\Omega_{max} = 0.457$ rad/s and $T = 0.89T_c$.

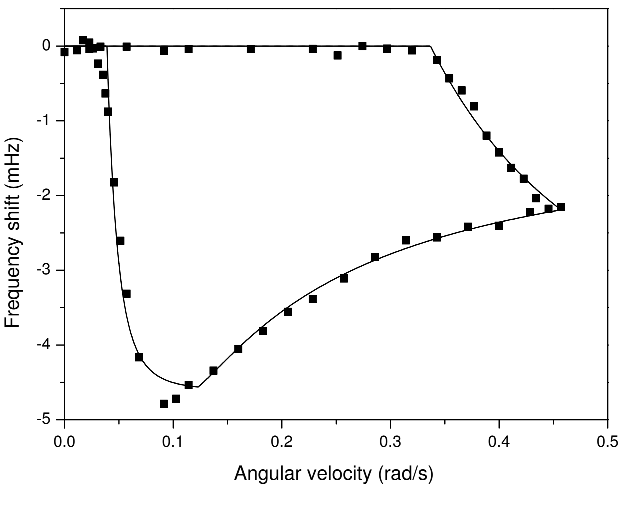

Figure 6.12: Rotation sweep with $\Omega_{max} = 0.457$ rad/s and $T = 0.95T_c$.

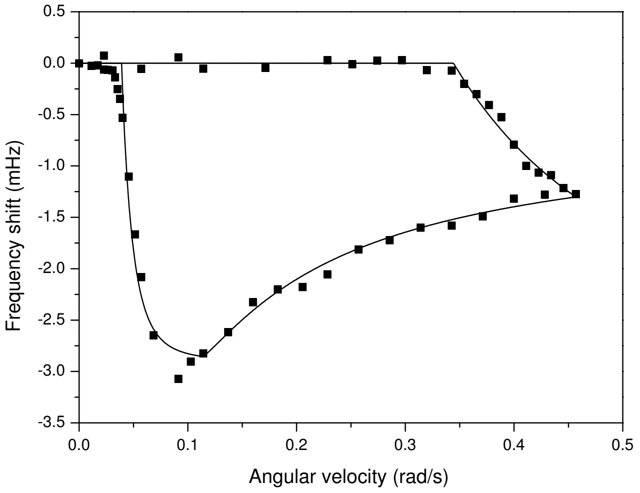

Figure 6.13: Rotation sweep with $\Omega_{max} = 0.457$ rad/s and $T = 0.97T_c$.

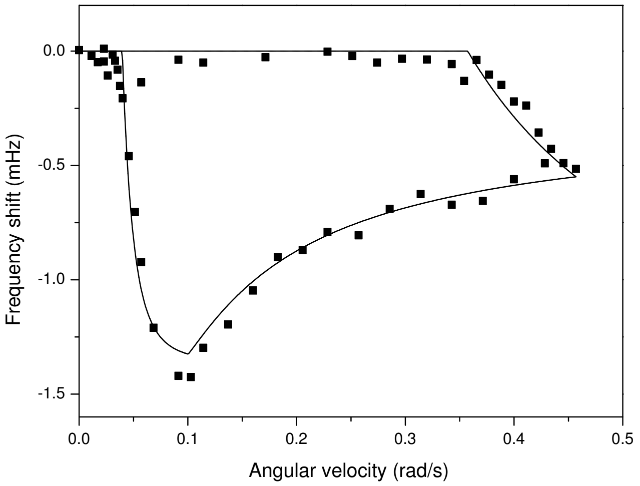

Figure 6.14: Rotation sweep with $\Omega_{max} = 0.457$ rad/s and $T = 0.99T_c$.

was found indicating that nucleation of vortices in ^{3}He-A is an intrinsic process. The values of v_c as a function of temperature showed considerable scatter, with the lower values around 0.25 mm/s and the upper values at 1.5 mm/s, although the scatter was reduced when the sample was slowly cooled into the superfluid state while rotating which should from the equilibrium texture and then reasonable agreement with the theoretically calculated critical velocities was obtained [75]. It was also found that vortices were sometimes formed in a burst like manner when ≈ 90 vortex lines were suddenly nucleated. This was explained as being due to a textural transition to a state where the critical velocity for vortex nucleation was lower.

Measurements of v_c at different temperatures for several samples that were thought to be uniform textures are shown in figure 6.16. The values are of the same order as the critical velocities found in the Helsinki experiment, a strong indication that the vortices are also continuous in our experiment. The scatter of the data is considerably less in comparison to the Helsinki work, probably because there is better control over the texture in our slab geometry.

6.5 Rotation sweeps in both directions

All of the rotation sweeps presented in the previous sections of this chapter were performed using the same direction of rotation as that used while cooling into the superfluid state. Rotation sweeps with the opposite sense of direction are slightly different. Figure 6.17 shows the frequency shifts for three rotation sweeps with small angular velocities ($|\Omega| < |\Omega_c|$) for different directions of rotation. The magnitude of Ω_F is noticeably reduced for the first sweep in the opposite direction and for all further sweeps in either direction with $|\Omega| < |\Omega_c|$. This difference is due to a small persistent superflow near the edge of the slab consisting of approximately 15 quanta of circulation caused by vortices remaining in the slab. Rotation in the opposite direction helps to unpin these vortices and results in a lower value of Ω_F.

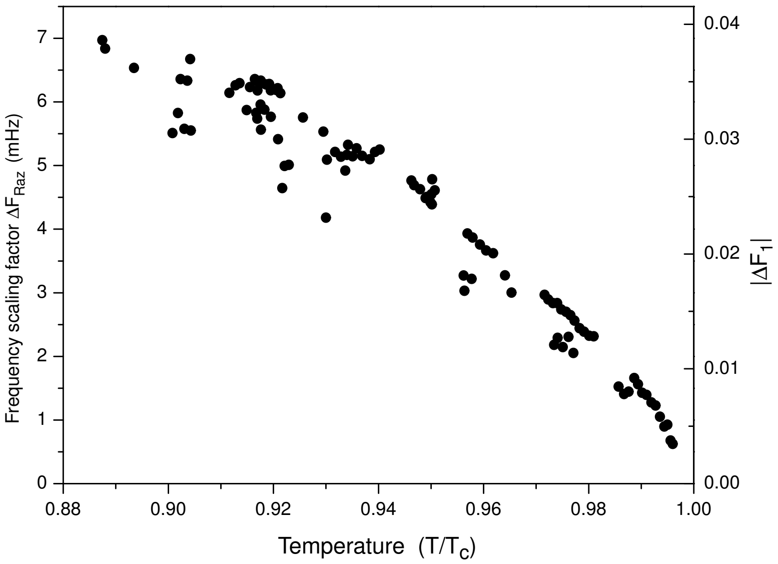

Figure 6.15: Frequency scaling factor obtained from least squares fits as a function of temperature.

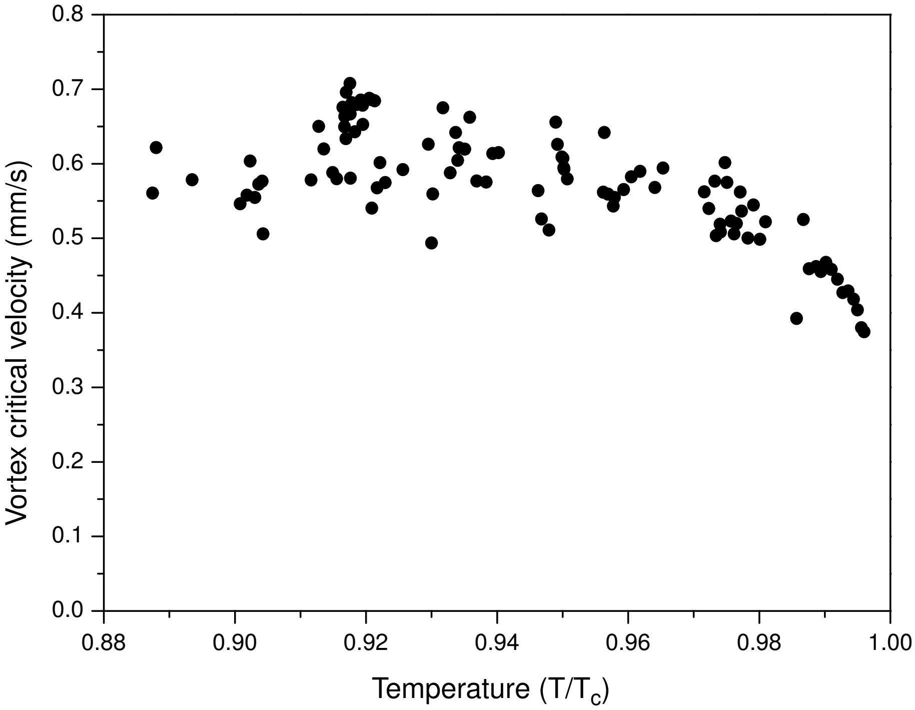

Figure 6.16: Critical velocity for vortex nucleation as a function of temperature. The critical angular velocity is $\Omega_c = v_c/R_{eff}$ where R_{eff} is the effective radius of 4.72 mm.

Figure 6.18 shows a series of rotation sweeps that were all performed in the same direction as that used while cooling. The first sweep was done before any rotation in the opposite direction and then all subsequent sweeps were performed after the cryostat had been rotated for one minute in the opposite direction at very small angular velocities. These further sweeps have values of Ω_F that are shifted to lower and lower angular velocities with steps in between each value corresponding to a reduction in the number of vortices that are trapped. The fact that the vortices can be unpinned by rotation at very small angular velocities in the other direction suggests that they are only weakly pinned. The source of the pinning is currently unknown but it is possible that extrinsic influences such as imperfections in the epoxy surfaces or the edge of the fill line in the center may play a role. The next chapter describes the much stronger pinning caused by defects in the texture.

Figure 6.19 show several rotation sweeps for both directions of rotation after the trapped vortices have been removed. There is still a small difference between the two directions with the sweeps in the original direction of rotation showing a much more rounded transition. Every sample of uniform texture that has been studied so far has shown this slight asymmetry after pinned vortices have been removed. A possible explanation for the difference is that in every single domain **l** texture there should always be one quantum of circulation at the outer perimeter due to the bending of the **l** texture to satisfy the boundary condition (see figure 6.6), resulting in a small but well defined persistent current. It is hoped that numerical simulations will show if this is the correct explanation.

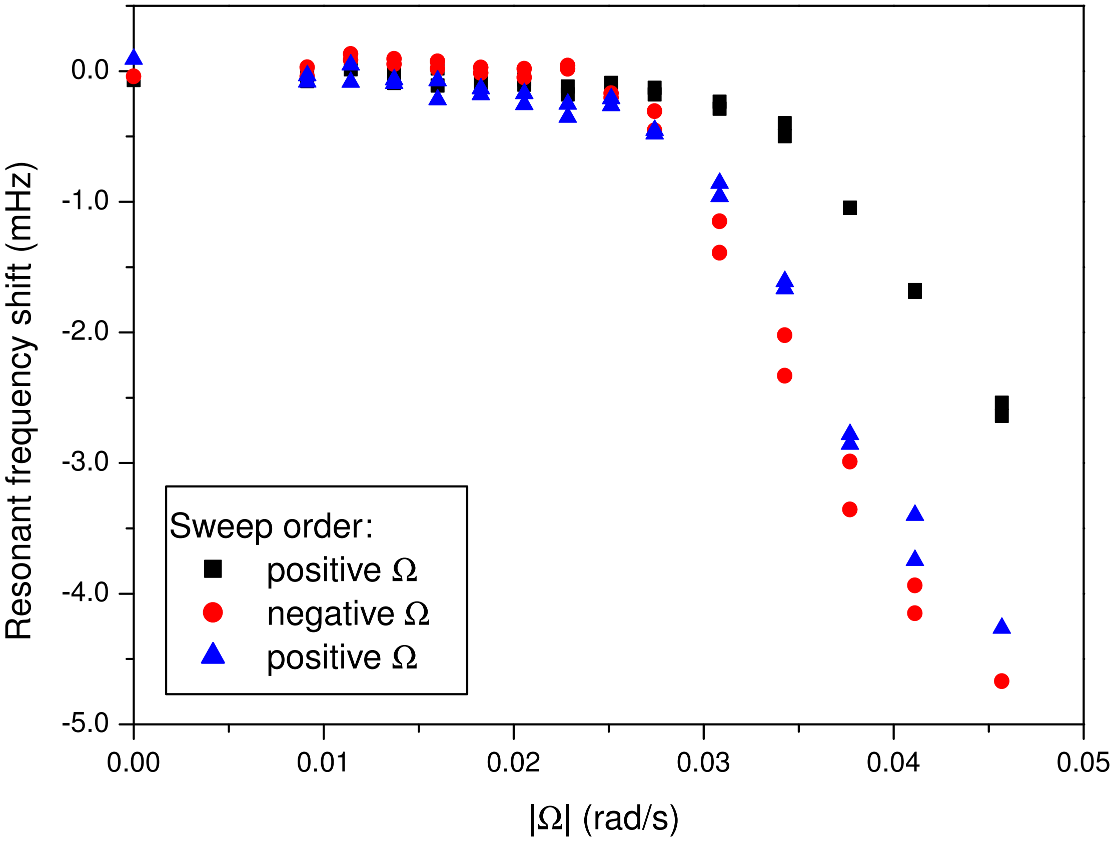

Figure 6.17: The frequency shift for three rotation sweeps with different directions of rotation. The black symbols are for a sweep performed with the same direction of rotation as that used while cooling (positive Ω). A sweep in the opposite direction (red symbols) was then performed followed by another sweep in the original direction (blue symbols).

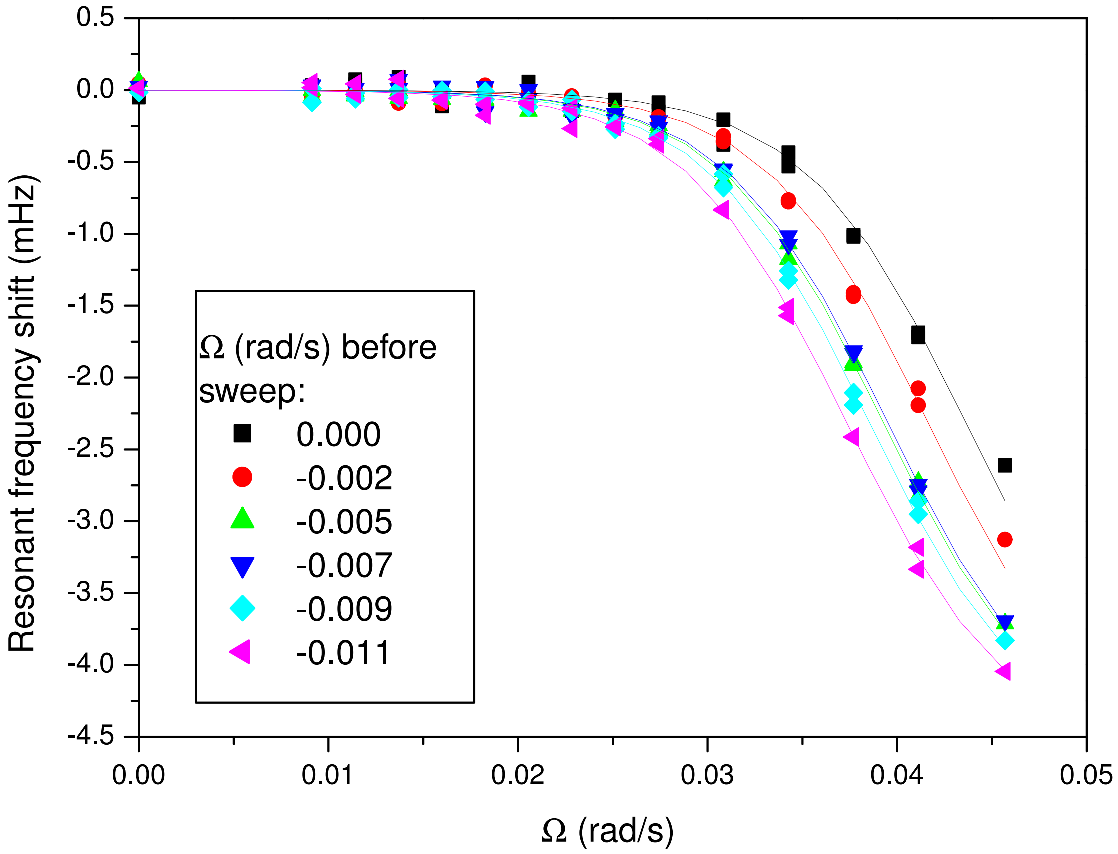

Figure 6.18: Frequency shifts for several rotation sweeps, all with the same sense of rotation, performed after very small rotations in the opposite direction. Ω_F decreases each time due to some of the vortices being unpinned.

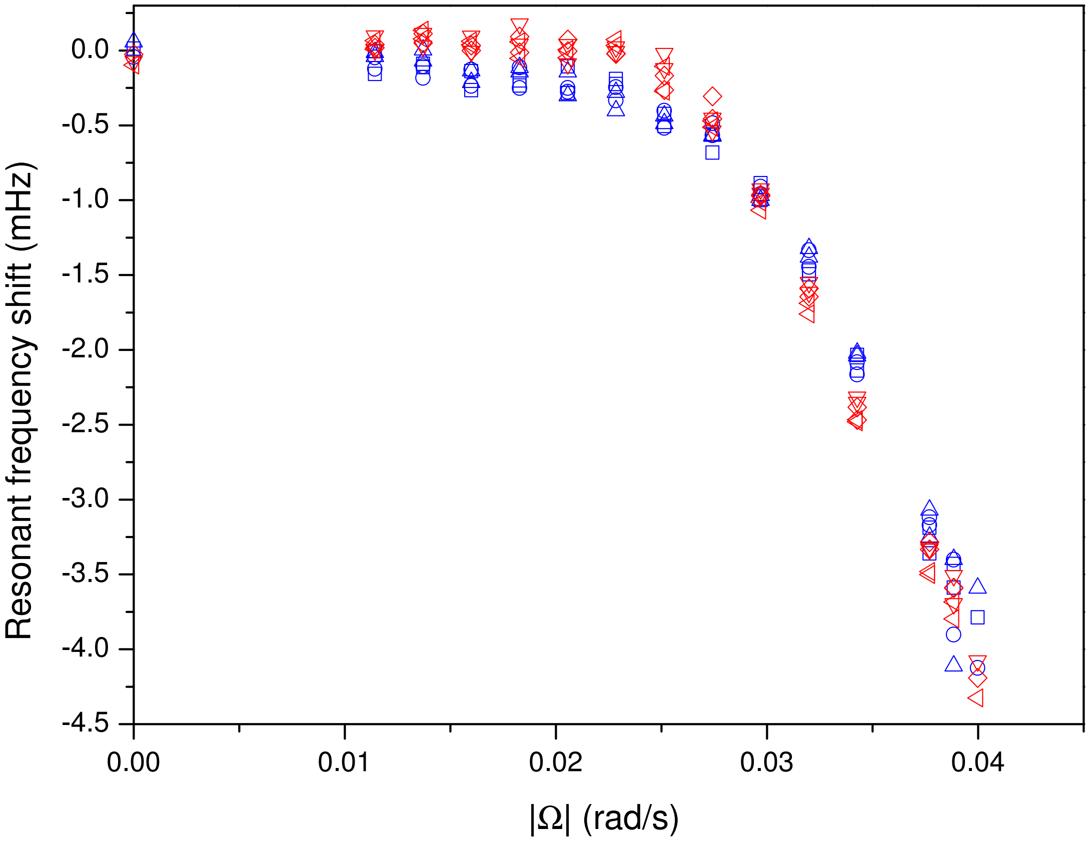

Figure 6.19: Several rotation sweeps for a texture that has been rotated in both directions to remove trapped vortices. The blue sweeps are for angular velocities in the same direction as that used while cooling and the red sweeps are for the opposite direction.

Chapter 7

Rotation while superfluid: non-uniform textures

7.1 Introduction

The previous chapter discussed rotation of an initially uniform texture and showed how two critical velocities could be obtained from the rotation sweeps. This chapter will discuss what happens when non-uniform textures are rotated. The behaviour is quite different to that of the uniform textures, where weak pinning of a few vortices was observed, since it seems that a substantial number of vortices can be strongly pinned by defects in the texture, leading to a persistent superflow near the perimeter of the slab after rotation has been stopped. As shown in chapter 5, non-uniform textures can be obtained by cooling from the normal state with no rotation or by warming from the superfluid B-phase. The effect of rotation on both these types of texture is discussed in section 7.2 and the results of an initial investigation into the lifetime and decay of the persistent superflow is described in section 7.3. Section 7.4 shows how the persistent currents depends upon the angular velocity of the cryostat and section 7.5 describes results obtained from magnetic field sweeps on textures with and without a persistent current. Section

7.6 discusses possible models to explain the magnitude of the persistent currents.

7.2 Rotation sweeps

The rotation sweeps for uniform textures, described in the previous chapter, were reproducible and showed little hysteresis in either the resonant frequency or the bandwidth. This is not the case for non-uniform textures. Figures 7.1 and 7.2 show the shifts in resonant frequency for a series of rotation sweeps performed on a texture formed by warming into the A phase from the B phase while the cryostat was stationary. The first sweep of rotation had positive Ω up to a maximum of 0.42 rad/s. When rotation was started the frequency initially decreased before starting to increase at higher angular velocities. The magnitude of the maximum shift of resonant frequency is less than that for uniform textures at a comparable temperature, indicating that the uniformity of the texture is poor. Deceleration led to the frequency increasing before levelling off, similar to the measurements on uniform textures. However, in this case, the frequency then decreases as the cryostat decelerates to low angular velocities such that the frequency after rotation has stopped is clearly lower than the initial value. A second sweep of rotation, in the same direction as the first, was then performed. This time the frequency increased for small angular velocities. It reached a maximum at $\Omega \simeq 0.03$ rad/s before decreasing. The behaviour during the rest of the sweep was then similar to that observed during the first sweep. All further sweeps for this direction of rotation were identical to the second sweep. Two sweeps of rotation in the opposite sense (negative Ω) were then performed. These sweeps showed similar behaviour to the first and second sweeps in the positive direction because the frequency initially decreased when rotation was started on the first sweep and the frequency then increased during the first part of the second sweep. The measurements described above clearly show that the superfluid had some memory of the previous rotation history even after rotation had been stopped. This must be due to a persistent

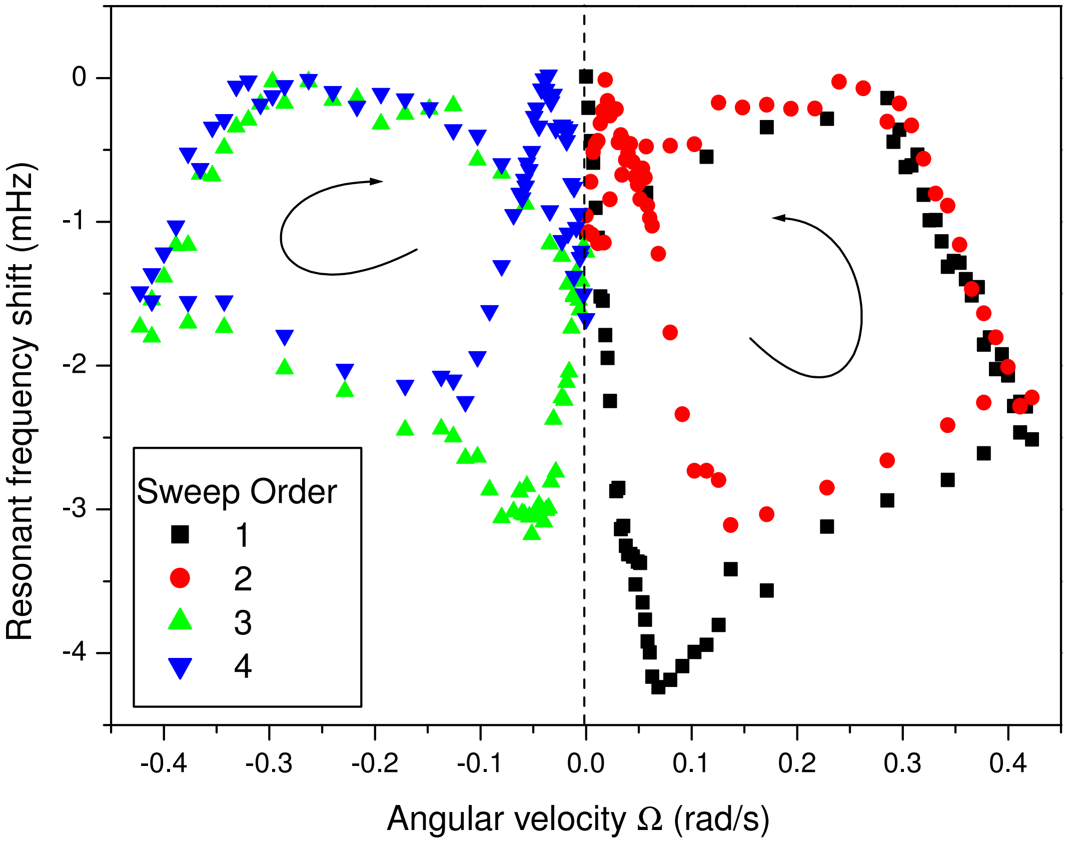

Figure 7.1: Resonant frequency shifts for a series of rotation sweeps performed on a texture created by warming from the B phase. The central region is shown in figure 7.2. The magnitude of the maximum frequency shift is less for the sweeps with negative Ω due to the sweeps being performed at a higher temperature.

superflow resulting from some vortices that are pinned and therefore unable to annihilate at the container walls. Such behaviour was not observed for uniform textures so the pinning must be due to defects (e.g. domain walls) in the texture. The maximum observed in the resonant frequency for small angular velocities is expected to correspond to the minimum counterflow when the angular velocity of the cryostat (and hence the normal component of the fluid) matches the angular velocity of the superflow, Ω_{pers} at the effective radius for vortex nucleation, R_{eff}, which was found from the rotation sweeps on uniform textures described in chapter 6. When the cryostat is stationary there is a small but non-zero counterflow which will tend to distort $\mathbf{l}$ in regions where the texture is non-uniform (i.e. at domain walls), leading to a decrease in frequency. The frequency and bandwidth shifts for rotation sweeps with small angular velocities ($\Omega < \Omega_c$) performed after rotation at 0.4 rad/s are shown in figures 7.3 and 7.4. The angular velocity of the persistent current was deduced from the position of the maximum frequency. For sweeps up to angular velocities not exceeding the critical value for vortex nucleation (Ω_c) the frequency shifts were reproducible during acceleration and deceleration and the angular velocity of the persistent current was steady for many hours (see section 7.3). Persistent currents could also be trapped in textures that were prepared by cooling from the normal state (N to A) without rotation. Figure 7.5 shows the frequency shift for such a sample. The behaviour is similar to the sweeps described above with the frequency increasing when rotation is started, but in this case the frequency at low angular velocity shows a flat plateau, with a width $\sim 2\Omega_F$, and then a sharp decrease in frequency instead of the rounded peak observed for the B to A textures. This suggests that the texture near the perimeter of the slab is more uniform for the N to A textures. A persistent current could also be trapped in some textures created while rotating during cooling into the superfluid state if the cooling rate was too high. A series of rotation sweeps for such a texture is shown in figure 7.6. The large frequency shifts indicate a near uniform texture. The magnitude of the maximum possible trapped persistent current for all of the above textures is approximately the same, $\Omega_{pers} \simeq 0.03$ rad/s, corresponding to

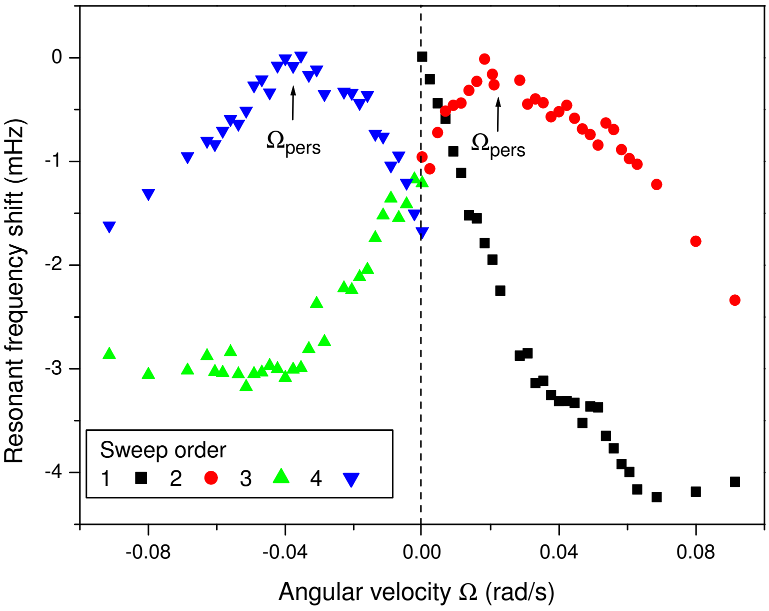

Figure 7.2: Resonant frequency shifts at small angular velocities during acceleration. A persistent current can be generated for both senses of rotation.

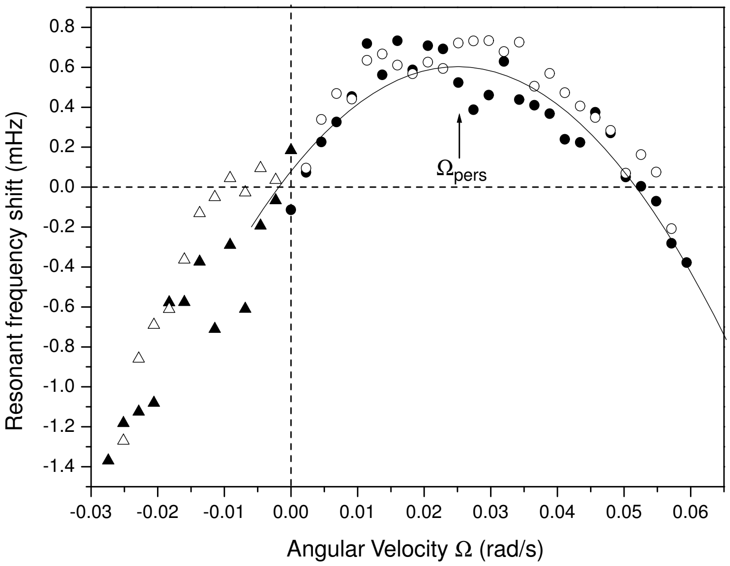

Figure 7.3: Resonant frequency shifts for small angular velocities. The solid and hollow symbols are during acceleration and deceleration respectively. The solid line is a quadratic polynomial fit to the points during acceleration. The maximum frequency is not at $\Omega = 0$ due to the presence of a small persistent current, Ω_{pers}.

approximately 60 circulation quanta (or 30 doubly quantized vortices).

7.3 Lifetime and decay of persistent currents

The lifetime and decay of the persistent superflow were investigated by sweeping angular velocity from zero to 0.05 rad/s and then back to zero approximately every 10 hours after a persistent current had been generated. This enabled the position of the maximum in the resonant frequency, and hence Ω_{pers}, to be monitored as a function of the time since the state had been created. Figure 7.7 shows the variation of Ω_{pers} with time for a texture that had been created by warming from the B-phase (see previous section). In this case, there was no observable decay in Ω_{pers} for the 33 hours after it had been created, but then there was a jump downwards in Ω_{pers} of $\simeq$ 0.013 rad/s during a routine cryogen transfer. Another jump of approximately the same magnitude occurred 25 hours later since there was a jump upwards in the resonant frequency of the oscillator (see figure 7.8). This second jump occurred on a day where there was very little activity in the department.

An initial study of the lifetime of a persistent current in a texture formed by cooling from the normal state (without rotation) found no observable decrease in Ω_{pers} during the 60 hours after it had been created.

7.4 Dependence of Ω_{pers} on Ω_{max}

Figures 7.9 and 7.10 show the dependence of Ω_{pers} upon the maximum angular velocity of the cryostat during a rotation sweep for textures prepared by warming from the B phase and by cooling from the normal state respectively. The cryostat was not rotated during the transition into the A phase so there was no initial persistent current in both cases. Rotation sweeps were then performed with positive

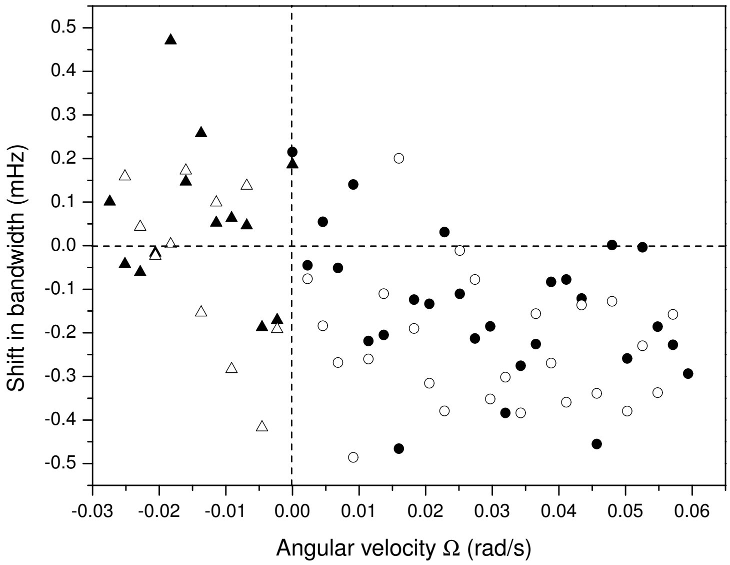

Figure 7.4: Shifts in bandwidth for small angular velocities. The solid and hollow symbols are during acceleration and deceleration respectively.

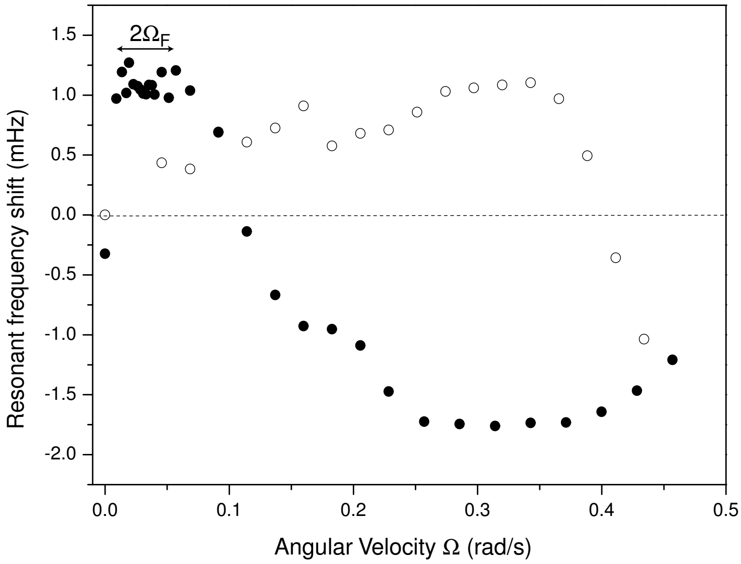

Figure 7.5: Example rotation sweep for a texture created by cooling from the normal state while the cryostat was stationary. The solid and open symbols are for acceleration and deceleration respectively.

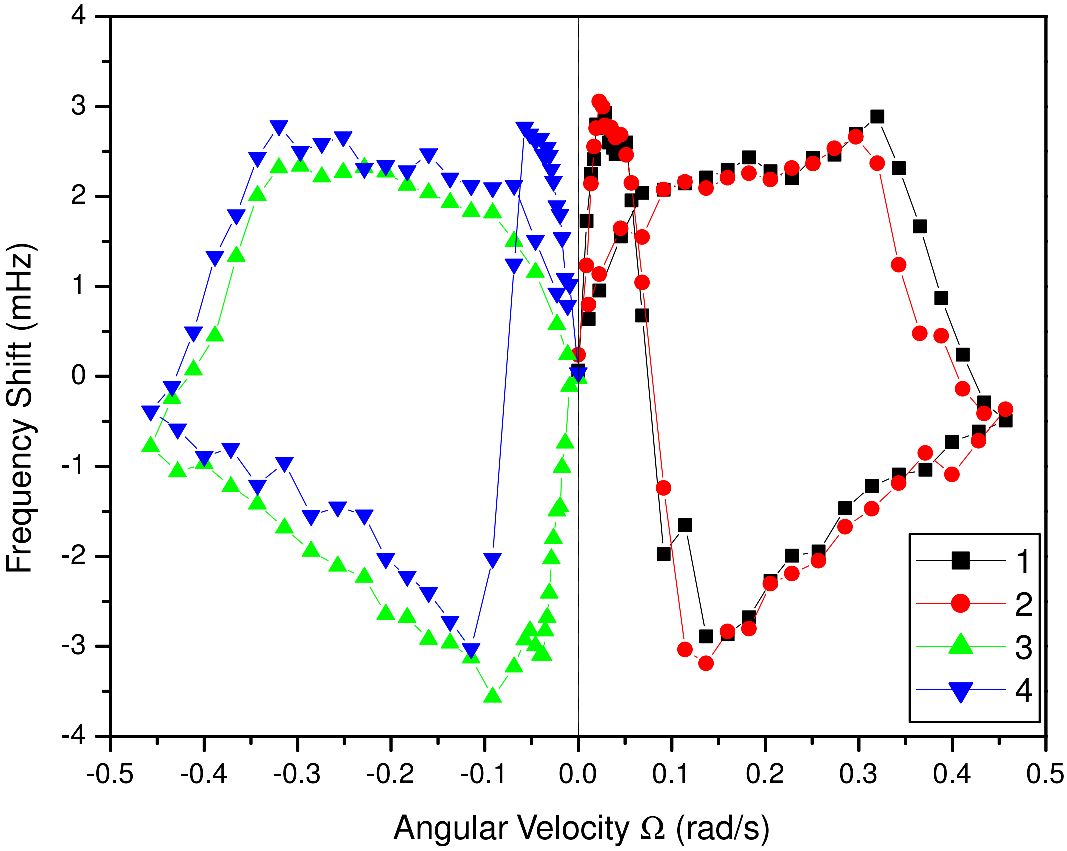

Figure 7.6: Rotation sweeps for a texture formed by rapid cooling from the normal state while rotating with positive Ω. The numbers denote the order in which the sweeps were performed.

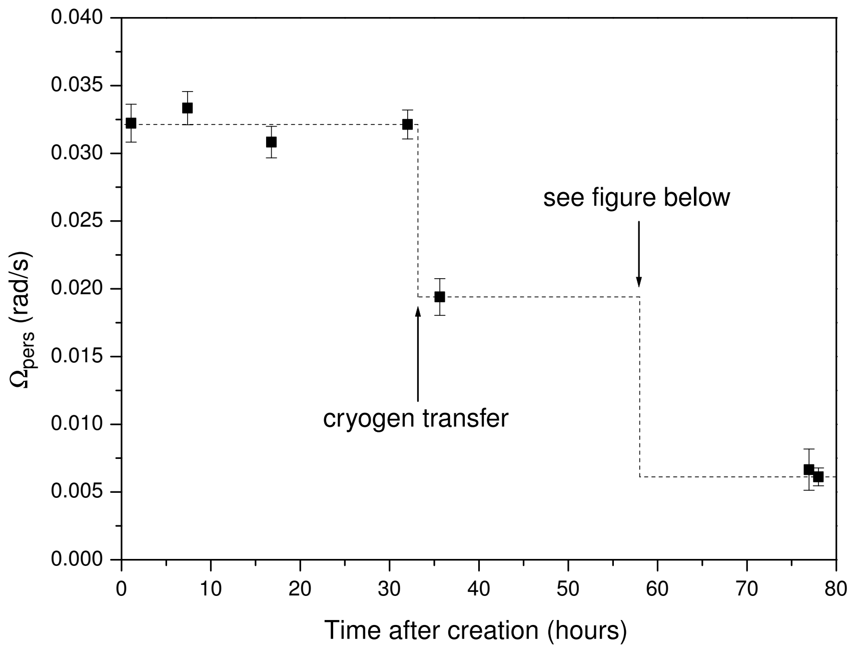

Figure 7.7: Magnitude of persistent current over a period of several days. The dashed line indicates when jumps in the resonant frequency (see figure 7.8) were observed.

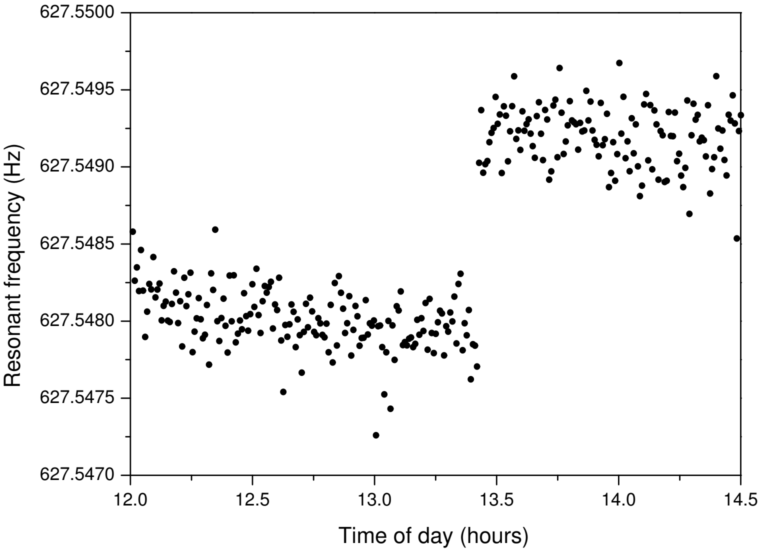

Figure 7.8: Jump in resonant frequency due to decay of persistent current. This event occurred 58 hours after the persistent current had been created.

Ω and the maximum angular velocity, Ω_{max}, was increased on each subsequent sweep. The persistent current angular velocity for each value of Ω_{max} was found by measuring the position of the frequency maximum during acceleration on the following sweep. The sweep with $\Omega_{max} = 0.46$ rad/s was repeated and then the process was repeated for rotation in the opposite sense (negative Ω).

The maximum persistent current that could be sustained for both types of textures was $\simeq 0.03$ rad/s. However, the behaviour for small Ω_{max} was different. In the B to A case, the minimum angular velocity ($\Omega_{max} = \Omega_c$) needed to create a non-zero persistent current is less than 0.035 rad/s but for the N to A case the critical angular velocity is $\Omega_c = 0.06$ rad/s and Ω_{pers} reaches a maximum when $\Omega_{max} \simeq 2\Omega_c$.

If the cryostat is then rotated in the opposite direction Ω_{pers} initially decreases until eventually a persistent current in the other direction is generated. The angular velocities where $\Omega_{pers} = 0$ are approximately -0.03 rad/s for the B to A texture and -0.07 rad/s for the N to A texture. The cycle was not completed by then rotating in the original direction but further studies are currently being carried out to study the behaviour of Ω_{pers} for these texture, including experiments to test whether reproducible behaviour is observed over several cycles of Ω_{max}. Possible models that could explain the persistent currents are discussed in section 7.6 including an explanation of the lines on figures 7.9 and 7.10.

7.5 Field sweeps

The frequency shift for number of field sweeps are shown in figures 7.11 to 7.13. Figure 7.11 shows two field sweeps for a N to A (with no rotation) texture. The first sweep was performed after cooling into the superfluid transition but before the cryostat was rotated. The transition field, H_F is 3.7 Gauss but the rounding of the transition and the frequency shift indicate that the texture was non-uniform. The

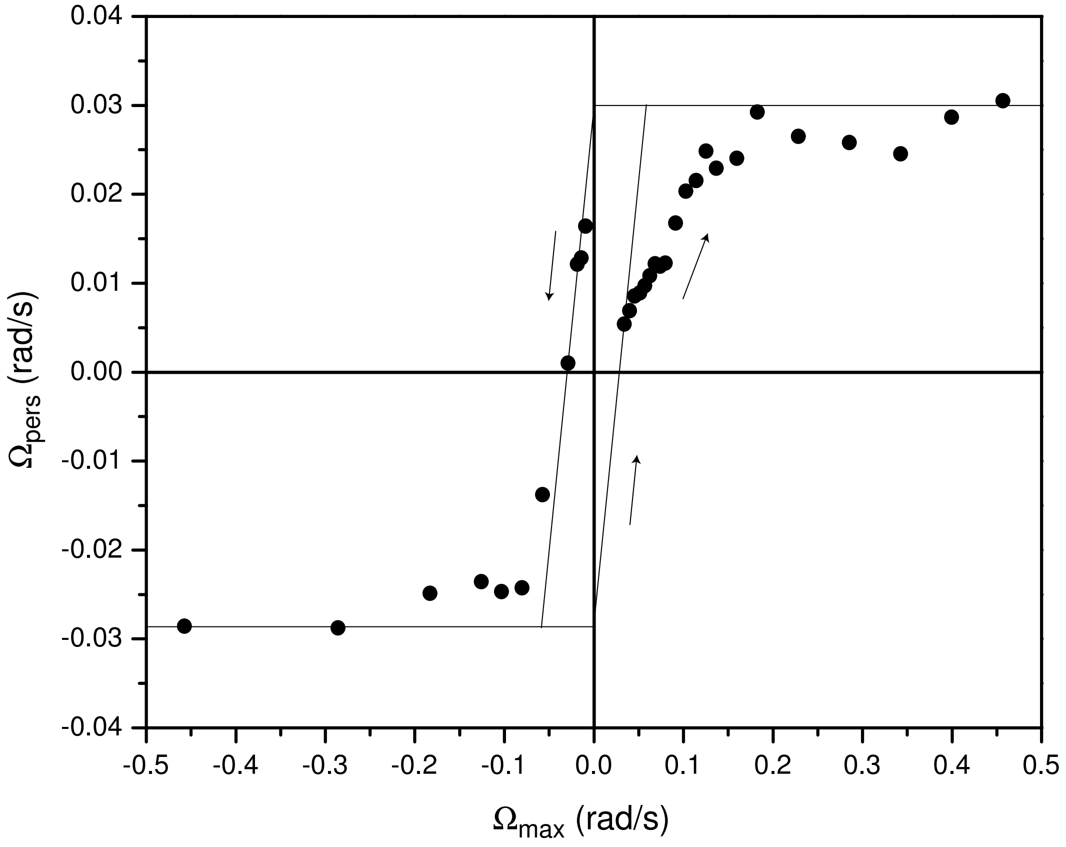

Figure 7.9: Persistent current angular velocity as a function of maximum angular for a texture prepared by warming from the B-phase. The solid line shows the expected behaviour in the limit of strong pinning.

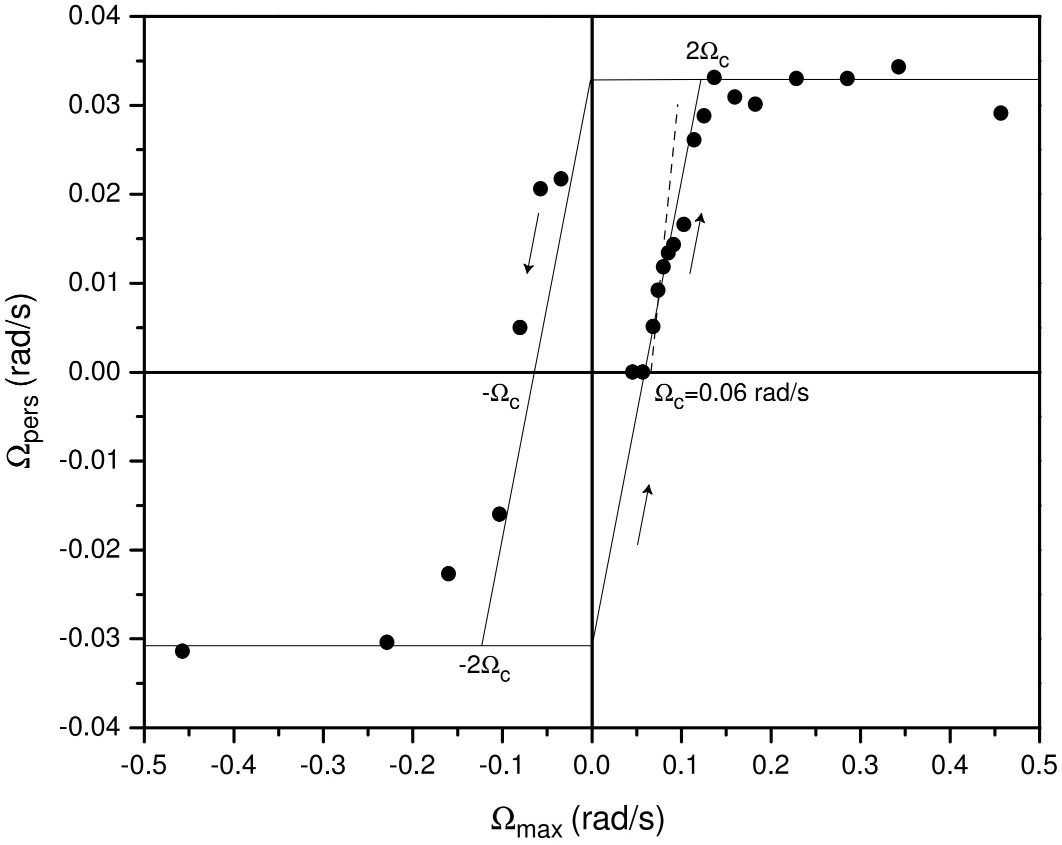

Figure 7.10: Persistent current angular velocity as a function of maximum angular for a texture prepared by cooling from the normal state with no rotation. The dashed line indicates the slope expected for the case of strong pinning.

cryostat was then rotated up to 0.46 rad/s and then stopped in order to generate a persistent current. The second field sweep was then performed. There are several differences from the first sweep. The transition field is much lower and also more rounded due to the presence of persistent superflow assisting the field in distorting the texture. The frequency shift is also larger and does not tend to the same value at high field as the previous sweep. This indicates that the texture is distorting in a different manner. The texture during the first sweep was likely to be planar but the persistent superflow would favour an azimuthal texture (see chapter 3) due to the orienting effect of the counterflow.

Figure 7.12 shows two field sweeps for a texture created by rapidly cooling from the normal state. The cryostat was rotated during the superfluid transition and when rotation was stopped a persistent current remained. A field sweep was then performed, this showed similar behaviour to the second field sweep described for the case above. A second field sweep was done while the cryostat was rotating at a constant angular velocity the same magnitude and direction as that of the persistent current, $\Omega = \Omega_{pers}$. This field sweep had a higher transition field because the orienting effect of the persistent superflow was minimized by matching the normal and superfluid angular velocities (i.e. the counterflow was minimized).

Figure 7.13 shows field sweeps for a texture created by warming from the B phase. One was before the cryostat was rotated and the second was carried out after rotation had generated a persistent current. In this case, unlike the measurement described above, there is very little that is different between the field sweeps. This is perhaps because the texture is highly non-uniform so the presence of the persistent superflow make little difference to how the texture distorts.

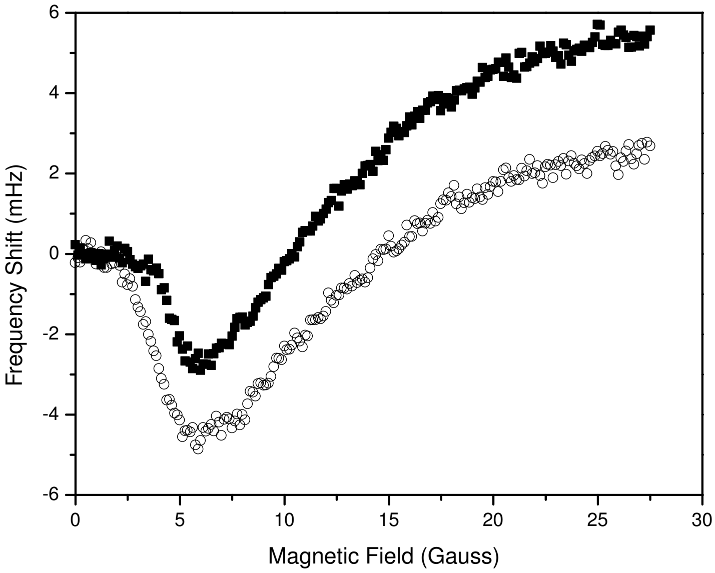

Figure 7.11: Frequency shift for magnetic field sweeps before (solid squares) and after (open circles) rotation for a texture prepared by cooling from the normal state with the cryostat stationary.

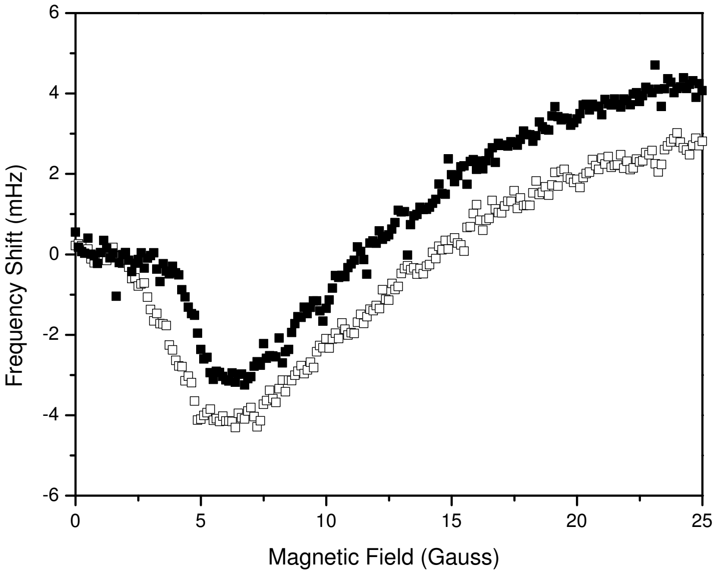

Figure 7.12: Frequency shift for magnetic fields when a persistent current is present. One is with the cryostat stationary (open squares) and the other is when the cryostat is rotating with angular velocity 0.034 rad/s (solid squares).

7.6 Possible models

It is clear when comparing the results for defect-free textures in the previous chapter and those of non-uniform textures with many defects presented in this chapter that the observed behaviour is strikingly different. The textures are hysteretic due to a persistent superflow generated by trapped vortices. The defects in the texture are in some way responsible for trapping the vortices such that there is an energy barrier preventing the vortices from escaping although the actual mechanism responsible for this behaviour has not yet been found. Another difference is that the critical velocities for vortex nucleation (and hence generation of a persistent current) for the non-uniform textures are at least a factor of two smaller than for uniform textures (figure 6.16). This may indicate that the vortices are nucleated in regions of inhomogeneous texture or that the structure of the vortices is different such that perhaps the vortex sheet, studied extensively in Helsinki, may play some sort of role.

No model has yet been developed to completely explain the observed hysteresis of Ω_{pers} with Ω_{max} although there are a few candidates. It is possible that the experimental data could be due to a combination of several mechanisms. The solid lines in figures 7.9 and 7.10 show behaviour that is very similar to that expected if all of the vortices are pinned. The expected hysteresis loop for Ω_{pers} against Ω_{max} in the limit of strong pinning, along with schematic diagrams showing what happens at each stage, is shown in figure 7.14. When the sample is first rotated (regime 1 in figure 7.14), no vortices are generated until $\Omega_{max} = \Omega_c$. Ω_{pers} then increases linearly with increasing Ω_{max} (regime 2) due to all of the vortices becoming pinned. However, Ω_{pers} reaches a constant maximum value of Ω_c for $\Omega_{max} > 2\Omega_c$ (regimes 3 and 4) due to the nucleation of vortices of opposite circulation (antivortices) during deceleration when the counterflow at the edge of the slab reaches $v_n - v_s = -v_c$. Rotation in the opposite sense (regime 5) leads to more antivortices being produced until a state with $\Omega_{pers} = 0$ (regime 6) is reached at $\Omega_{max} = -\Omega_c$. Further rotation in this direction will then generate a persistent current with negative circulation,

$\Omega_{pers} < 0$.

Comparison of the strong pinning model with the experimental data for the B to A (figure 7.9) and N to A (figure 7.10) shows a number of similarities although the agreement is not perfect in both cases. The B to A texture does have a maximum value of Ω_{pers} that is comparable to Ω_c but the slope of Ω_{pers} against Ω_{max} is less than what is expected from the model. However, when the sample was rotated in the opposite direction the agreement was considerably better. Ideally, several cycles of the hysteresis loop should be performed because the behaviour may be different when the sample is first rotated. The major difference between the model and the data for the N to A texture is that the maximum persistent current is a factor of two less than the model would predict since the maximum is $\simeq 0.5\Omega_c$ hence the slope of the data points for $\Omega < 2\Omega_c$ is less than the model predicts, as for the B to A texture. The fact that the maximum possible Ω_{pers} for both types of texture are similar, even though the critical velocities are about a factor of two different, suggests that perhaps the number of vortices that can be trapped is limited by a maximum pinning force which is the same for both types of texture. Again, further study is needed to clarify the underlying mechanisms. It may also be useful to repeat the experiment using a different technique that is non-invasive such as NMR. The torsional oscillator technique used in this work is mainly sensitive to the effects of flow on the $\mathbf{l}$ texture at the perimeter of the slab whereas NMR experiments are sensitive to the number and structure of vortices and hence would provide useful insight into the behaviour of the trapped vortices. The disadvantage of NMR is that it requires a finite magnetic field, whereas the torsional oscillator can be used in zero and non-zero fields.

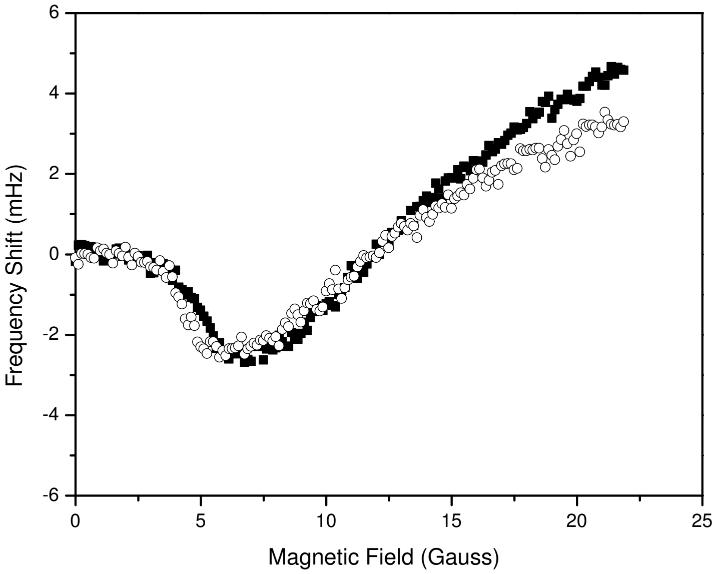

Figure 7.13: Frequency shift for magnetic field sweeps before (solid squares) and after (open circles) rotation for a texture prepared by warming from the B phase.

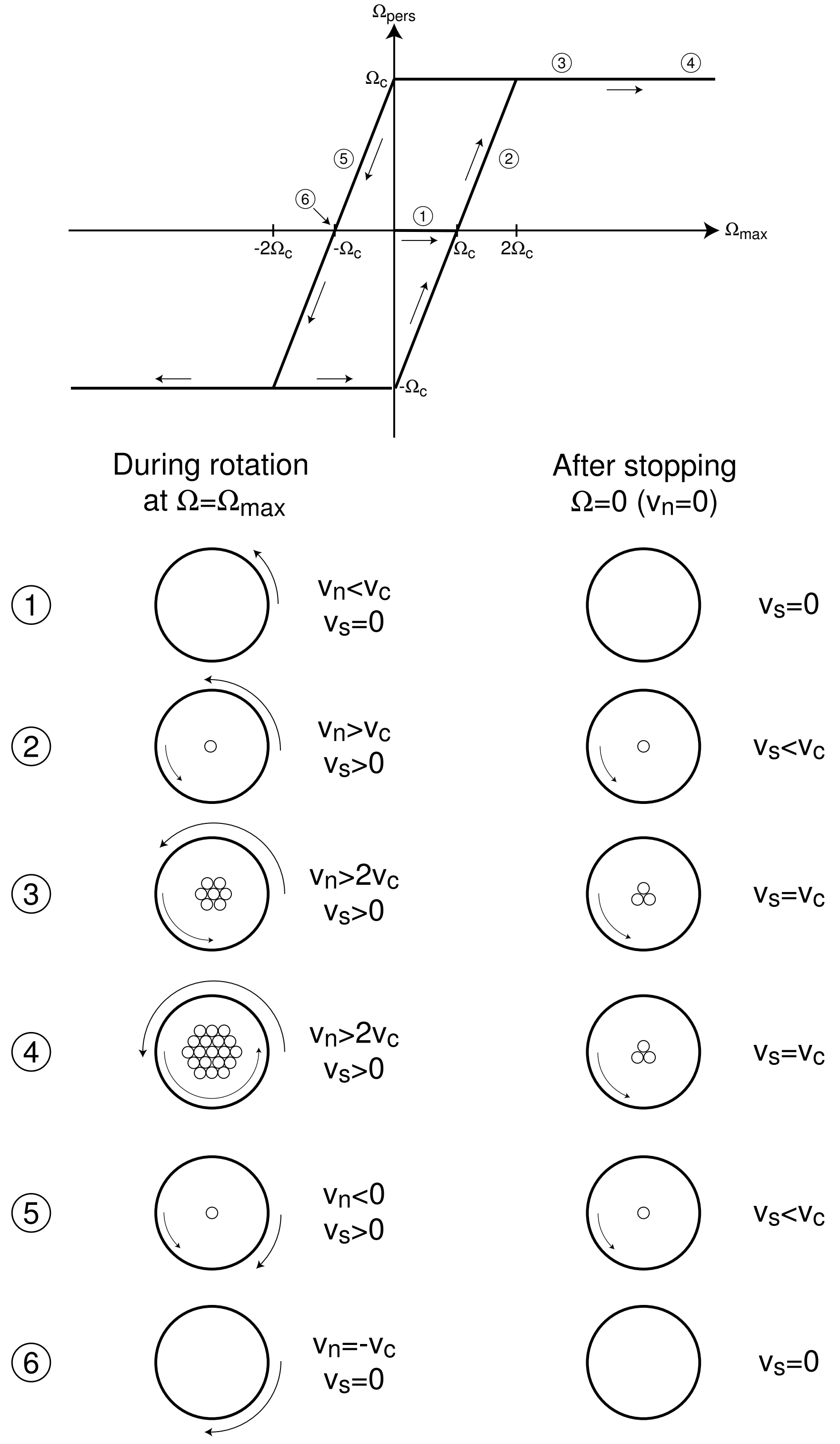
Ω_{pers}
Ω_c
③
④
⑤
②
⑥
①
Ω_{max}
$-2\Omega_c$
$-\Omega_c$
Ω_c
$2\Omega_c$
$-\Omega_c$
During rotation at $\Omega=\Omega_{max}$
After stopping $\Omega=0$ ($v_n=0$)
①
$v_n<v_c$ $v_s=0$
$v_s=0$
②
$v_n>v_c$ $v_s>0$
$v_s<v_c$
③
$v_n>2v_c$ $v_s>0$
$v_s=v_c$
④
$v_n>2v_c$ $v_s>0$
$v_s=v_c$
⑤
$v_n<0$ $v_s>0$
$v_s<v_c$
⑥
$v_n=-v_c$ $v_s=0$
$v_s=0$

Figure 7.14: Behaviour of superfluid in the limit of strong pinning. The inner and outer arrows give an indication of the direction and magnitude of the velocity of the superfluid (v_s) and normal (v_n) components respectively.

Chapter 8

Conclusions

The original motivation of this experiment was to measure the predicted orbital ferromagnetism. We have calculated its expected effect on textures in a slab geometry but we have not been able to observe these effects experimentally. At the moment we can claim that the orbital ferromagnetic moment must be less than $10^{-10}\mu_B$ per atom. This upper limit is still an order of magnitude greater than Leggett's prediction [21]. Our calculations show that experiments utilizing very high fields ($\sim$ 10 T) may be more successful because the ferromagnetic energy term would then dominate the dipolar energy resulting in a uniform texture with **l** and **d** perpendicular to each other.

We have also calculated other textures including a dipole-locked domain wall and the simplest continuous vortex for our geometry, which is the double quantum radial Anderson-Toulouse vortex. Our calculations suggest that continuous vortices should be formed in preference to singular vortices when cooling into the superfluid state for the angular velocities used during this experiment ($\sim$ 0.4 rad/s). Further work is planned to extend these calculations to AT vortices that have an azimuthal component of **l** and to also include the effects of dipole-unlocking.

The magnetic field induced Fréedericksz transition has been used to qualitatively study the uniformity of the texture by observing both the sharpness of the transition and the magnitude of the maximum frequency shift. Uniform textures were obtained by cooling through the superfluid transition whilst rotating in zero field at any Ω. The situation was more complicated when a magnetic field of 2.2 G was used during cooling but uniform textures could only be obtained using an angular velocity of $\Omega \simeq 0.4$ rad/s. The Fréedericksz transition was found to be sharpest for uniform textures since the presence of defects and persistent currents in non-uniform textures resulted in transitions that were much more rounded.

We have developed a simple model to explain the resonant frequency shifts observed when the cryostat is rotated while in the superfluid state. The excellent agreement between the model and experiment over a wide temperature range suggests that the behaviour of the vortex cluster is well described by the continuum model. Our results provide clear evidence that the vortices are created at an effective radius that is approximately one slab thickness from the outer perimeter. We have measured both the critical velocity for alignment of the $\mathbf{l}$ texture by flow and the critical velocity for vortex nucleation. The values for the vortex critical velocity in our geometry are consistent with previous experiments in other geometries [74]. We find that what we identify as uniform textures are able to trap approximately 10 quanta of circulation after rotation has been stopped. However, these pinned vortices are easily removed by small angular velocity rotations in the opposite direction of rotation suggesting that the pinning is quite weak.

Initial studies of the effect of rotation upon non-uniform textures formed by cooling from the normal state and by warming from the B phase (without rotation in both cases) has showed that a substantial persistent current of approximately 60 circulation quanta in either direction can be generated and sustained for many hours in both these textures. The lack of such an effect in uniform textures suggests that the persistent currents must be stabilized by defects in the texture and not by some external constraint. The exact mechanism causing this behaviour is not yet understood, and this experiment is still ongoing in order to clarify the role of specific topological defects in the hysteretic behaviour of the persistent currents as a function of the angular velocity of the cryostat, further experiments using other techniques may also provide further insight.

Combining all of the above observations we are able to characterize the behaviour of different textures. Uniform textures exhibits sharp textural transitions due to applied flow and magnetic fields and the magnitude of the maximum resonant frequency shifts of the torsional oscillator is large. The vortex critical velocity is the highest observed in our experiments and there is little hysteresis in rotation sweeps. Approximately 10 circulation quanta can be weakly trapped after a rotation sweep, but they can be removed by rotating in the opposite direction. After that a uniform oriented texture with a single quantum of circulation at the outer perimeter of the slab is achieved. On the other hand, the textures formed by warming from the B phase exhibit smeared textural transitions with smaller frequency shifts and the vortex critical velocity is at least a factor of three lower. This texture also shows hysteretic behaviour when rotation is swept due to long lived persistent currents. The maximum observed persistent current corresponds to approximately 60 trapped circulation quanta. Finally, the properties of textures created by cooling from the normal state without rotation are somewhere in between the previous two cases. The textural transitions are sharp and the frequency shifts and vortex critical velocity fall somewhere in between the values of the other two textures. The behaviour is again hysteretic when rotation is swept with a maximum persistent current of approximately the same magnitude as the B to A texture.

References

[1] A. M. Guénault, *Basic Superfluids*, Taylor & Francis (2003)

[2] D. R. Tilley and J. Tilley, *Superfluidity and Superconductivity*, Third Edition, IOP (1990)

[3] M. H. Anderson, J. R. Ensher, M. R. Matthews, C. E. Wieman and E. A. Cornell, Science **269**, 198 (1995)

[4] K. B. Davis, M. O. Mewes, M. R. Andrews, N. J. van Druten, D. S. Durfee, D. M. Kurn and W. Ketterle, Phys. Rev. Lett. **75**, 3969 (1995)

[5] L. N. Cooper, Phys. Rev. **104**, 1189 (1956)

[6] J. Bardeen, L. N. Cooper and J. R. Schrieffer, Phys. Rev. **108**, 1175 (1957)

[7] P. W. Anderson and P. Morel, Phys. Rev. **123**, 1911 (1961)

[8] R. Balian and N. R. Werthamer, Phys. Rev. **131**, 1553 (1963)

[9] P. W. Anderson and W. F. Brinkman, Phys. Rev. Lett. **30**, 1108 (1973)

[10] D. D. Osheroff, R. C. Richardson and D. M. Lee, Phys. Rev. Lett. **28**, 885 (1972)

[11] D. D. Osheroff, W. J. Gully, R. C. Richardson and D.M. Lee, Phys. Rev. Lett. **29**, 920 (1972)

[12] D. S. Greywall, Phys. Rev. B **33**, 7520 (1986)

[13] D. Vollhardt and P. Wolfle, *The Superfluid Phase of Helium 3*, Taylor & Francis (1990)

[14] W. F. Brinkman and M. C. Cross, in Progress in Low Temperature Physics, edited by D.F. Brewar, Vol. VIIa, North Holland (1978)

[15] A. J. Leggett, Rev. Mod. Phys. **47**, 331 (1975)

[16] P. G. De Gennes, *The Physics of Liquid Crystals*, OUP, London (1974)

[17] V. Ambegaokar, P. G. De Gennes and D. Rainer, Phys. Rev. A **9**, 2676 (1974)

[18] J. R. Hook, A. D. Eastop, E. Faraj, S. G. Gould and H. E. Hall, Phys. Rev. Lett. **57**, 1749 (1986)

[19] S. G. Gould,*Observation of a Freedericksz transition in superfluid* ^{3}*He-A* , Ph.D Thesis, University of Manchester (1986)

[20] A. D. Eastop,*Ultrasonic Investigations of Magnetic Field Induced Textural Changes in Superfluid* ^{3}*He-A* , Ph.D Thesis, University of Manchester (1986)

[21] A. J. Leggett, Nature **270**, 585 (1977)

[22] N. R. Kestner, J. Chem. Phys. **48**,252 (1968)

[23] C. Huiszoon and M. Caffarel, J. Chem. Phys. **104**, 4621 (1996)

[24] N. Kurita and H. Sekino, Chem. Phys. Lett. **348**, 139 (2001)

[25] R. A. Aziz and M. J. Slaman, J. Chem. Phys. **94**, 8047 (1991)

[26] D. N. Paulson and J. C. Wheatley, Phys. Rev. Lett. **40**, 557 (1978)

[27] A. J. Manninen, T. D. C. Bevan, J. B. Cook, H. Alles, J. R. Hook and H. E. Hall, Phys. Rev. Lett. **77**, 5086 (1996)

[28] R. P. Fenyman, *Application of quantum mechanics to liquid helium*, in *Progress in Low Temperature Physics* **I** (ed. by C. J. Gorter), North Holland, Amsterdam (1955)

[29] R. J. Donnelly, *Quantized Vortices in Helium II*, Cambridge University Press, Cambridge (1991)

[30] N. D. Mermin and T.L. Ho, Phys. Rev. Lett. **36**, 594 (1976)

[31] O. V. Lounasmaa and E. Thuneberg, Proc. Natl. Acad. Sci. **96**, 7760 (1999)

[32] R. Blaauwgeers, V. B. Eltsov, M. Krusius, J. Ruohio and R. Schanen, *Quantized Vorticity in Superfluid* ^{3}*He-A* in *Quantized Vortex Dynamics and Superfluid Turbulence*, Ed. C. Barenghi, Springer-Verlag, Berlin, (2001)

[33] Ü. Parts, E. V. Thuneberg, G. E. Volovik, J. H. Koivuniemi, V. H. Ruutu, M. Heinilä, J. M. Karimäki and M. Krusius, Phys. Rev. Lett. **72**, 3839 (1994)

[34] E. V. Thuneberg, Physica B **210**, 287 (1995)

[35] P. W. Anderson and G. Toulouse, Phys. Rev. Lett. **38**, 508 (1977)

[36] P. L. Gammel, T. L. Ho. and J. D. Reppy, Phys. Rev. Lett. **55**, 2708 (1985)

[37] P. J. Hakonen, K. K. Nummila, J. T. Simola, L. Skrbek and G. Mamniashvili, Phys. Rev. Lett. **58**, 678 (1987)

[38] P. Hakonen, O. V. Lounasmaa and J. Simola, Physica B **160**, 1 (1989)

[39] J. P. Pekola, J. T. Simola, K. K. Nummila, O. V. Lounasmaa and R. E. Packard, Phys. Rev. Lett. **53**, 70 (1984)

[40] G. Arfken, *Mathematical Methods for Physicists*, Second Edition, Academic Press, London (1970)

[41] FlexPDE v3, PDE Solutions, http://www.pdesolutions.com

[42] A. L. Fetter, Phys. Rev. B **14**, 2801 (1976)

[43] A. L. Fetter, Phys. Rev. B **15**, 1350 (1977)

[44] A. L. Fetter, J. Low Temp. Phys. **67**, 17 (1987)

[45] J. R. Hook, A. D. Eastop, E. Faraj, S. G. Gould and H. E. Hall, Can. J. Phys. **65**, 1486 (1987)

[46] J. R. Hook, J. Low Temp. Phys. **74**, 19 (1989)

[47] J. R. Hook, *Texture and Anisotropic Properties of a Slab of* ^{3}*He-A in a Magnetic Field* in *Helium Three*, Ed. by W. P. Halperin and L. P. Pitaevskii, Elsevier Science (1990)

[48] B. C. Israelsson, B. C. Crooker, H. M. Bozler and C. M. Gould, Phys. Rev. Lett. **53**, 1943 (1984)

[49] K. Maki, J. Low Temp. Phys. **32**, 1 (1978)

[50] T. D. C. Bevan, A. J. Manninen, J. B. Cook, H. Alles, J. R. Hook and H. E. Hall, J. Low Temp. Phys. **109**, 423 (1997)

[51] C. R. Hu, T. E. Ham and W. M. Saslow, J. Low Temp. Phys. **32**, 301 (1978)

[52] M. M. Salomaa and G. E. Volovik, Rev. Mod. Phys. **59**, 533 (1987)

[53] P. M. Walmsley, *Design and Construction of an Experiment to Measure the Orbital Magnetic Moment of* ^{3}*He-A* , 1st Year Ph.D report, University of Manchester (2000)

[54] L. Z. Ruan and J. R. Sambles, J. Appl. Phys. **92**, 4857 (2002)

[55] E. L. Andronikashvili, Zh. Eksp. Teor. Fiz. **16**, 780 (1946)

[56] J. R. Hook, E. Faraj, S. G. Gould and H. E. Hall, J. Low Temp. Phys. **74**, 45 (1989)

[57] NGK Berylco, Houston Park, Montford Street, Salford, M5 2RP.

[58] B. D. Montogomery, *Solenoid Magnet Design*, Krieger (1980)

[59] F. Pobell, *Matter and Methods at Low Temperatures*, Second Edition, Springer, Berlin (1996)

[60] P. S. Wootton, *Torsional Oscillator Studies of Superfluid ^{3}He in Aerogel*, Ph.D. Thesis, University of Manchester (2000)

[61] D. C. Carless, H. E. Hall and J. R. Hook, J. Low Temp Phys. **50**, 583 (1983)

[62] T. A. Alvesalo, T. Haavasoja, M. T. Manninen and A.T. Soinne, Phys. Rev. Lett. **44**, 1076 (1980)

[63] T. D. C. Bevan, *Mutual Friction in Superfluid ^{3}He* , Ph.D. Thesis, University of Manchester (1995)

[64] H. E. Hall, J. R. Hook, S. Wang, A. J. Armstrong and T.D Bevan, Physica B **194-196**, 41 (1994)

[65] OYO Geopspace EAME, F3 Enterprise Way, Luton Bedfordshire, LU3 4BU.

[66] D. J. Cousins, S. N. Fisher, A. M. Guénault, R. P. Haley, I. E. Miller, G. R. Pickett, G. N. Plenderleith, P.Skyba, P. Y. A. Thibault and M. G. Ward, J. Low Temp. Phys. **114**, 547 (1999)

[67] Firestone Airmount Isolators, Firestone Industrial Products Co., 701 Congressional Blvd., Carmel, Indiana 46032, USA.

[68] Newport Ltd., 4320 First Avenue, Newbury Business Park, London Road, Newbury RG142 PZ, UK

[69] M. A. Clayton, *Investigations of Orbital Textures in ^{3}He-A Using Ultrasound and Computer Simulations*, Ph.D. Thesis, University of Manchester (1989)

[70] Ü. Parts, J. M. Karimäki, J. H. Koivuniemi, M. Krusius, V. M. H. Ruutu, E. V. Thuneberg and G. E. Volovik, Phys. Rev. Lett. **75**, 3320 (1995)

[71] Ü. Parts, V. V. Avilov, J. H. Koivuniemi, N. B. Kopnin, M. Krusius, J. J. Ruohio and V. M. H. Ruutu, Phys. Rev. B **62**, 5865 (2000)

[72] R. Blaauwgeers, V. B. Eltsov, M. Krusius, J. J. Ruohio, R. Schanen and G. E. Volovik, Nature **404**, 471 (2000)

[73] V. B. Eltsov, R. Blaauwgeers, N. B. Kopnin, M. Krusius, J. J. Ruohio, R. Schanen and E. V. Thuneberg, Phys. Rev. Lett. **88**, 065301-1 (2002)

[74] V. M. H. Ruutu, J. Kopu, M. Krusius, Ü. Parts, B. Plaçais, E. V. Thuenberg and W. Xu, Phys. Rev. Lett. **79**, 5058 (1997)

[75] J. Kopu, R. Hänninen and E. V. Thuneberg. Phys. Rev. B **62**, 12374 (2000)